Bifurcations in Fluid Systems: Petrov-Galerkin Schemes

Memoria presentada por

Álvaro Meseguer Serrano[1], [2]

para optar al grado de Doctor en Ciencias.

Director:

Francesc Marquès Truyol[3]

Universitat Politècnica de Catalunya, Abril 1998

---

[1] Departament de Física Aplicada (U.P.C), alvar@benard.upc.es
[2] Departament de T.A.C. (EUPMT), messegue@eupmt.es
[3] Departament de Física Aplicada (U.P.C), marques@chandra.upc.es

Acknowledgements

For his essential guidance and support throughout my whole research, I am deeply thankful to my work director, Francesc Marquès. For all their assistance in solving technical problems arisen in some parts of the present task, my thanks go to Juan Sánchez and Daniel Crespo. I would also like to acknowledge all the help that the fluid dynamics research team from my department (Arantxa, Isabel, Marta, Vicente, Albert, Dani, Oriol, etc...), has generously provided. It would be unfair to forget the technical support provided by the system manager, Amador, as well as Silvia, who has been crucial for the registration bureaucratic procedure of this work.

I am in debt to my family, specially to my father, whose unvaluable support and good advice have been essential in the evolution of my scientific career. Finally, I also owe a debt of gratitude to Pilar and Sergio, two of the most generous and kind people I have ever met. Without their personal support, this work would not exist.

In memory of my mother,

to my father,

to my brothers,

to Sergio and, specially,

to Pi.

Contents

Chapter 1

Introduction

1.1 Navier-Stokes Equations and Dynamical Systems

The basic laws which describe the dynamics of viscous fluids were independently formulated more than a century ago by Navier (1823) and Stokes (1845). In its initial stages, it was necessary to solve fundamental questions concerning the physical hypotheses used to obtain the formulation: Newtonian fluid hypothesis, stress tensor structure, stick boundary conditions over the rigid wall, etc. After their eventual formulation, there arose many other questions of mathematical nature. In fact, a complete formalism was needed to provide a comprehensive description of the solutions of the Navier-Stokes equations. Since then, the difficulty has laid on the integration of solutions from these equations for different problems. The nonlinearity of the Navier-Stokes equations makes it impossible to integrate them by use of standard analytical methods (except in the most simple cases or under the assumption of symmetry hypotheses). Moreover, the problem is not only technical but also conceptual. The main question arising at this point concerns the existence and uniqueness of solutions for the Navier-Stokes initial boundary problem. The answer to this question strongly depends on the physical dimension of the fluid system. Although existence and uniqueness theorems have been provided for the two-dimensional case, equivalent theorems asserting the simultaneous existence and uniqueness of solutions for three-dimensional flows, have not been demonstrated.

Apart from the pure mathematical problems of existence and uniqueness, many other physical questions arise. On the one hand, the stability of steady flows must be studied in order to predict new secondary flows (also termed bifurcated solutions). On the other hand, a deeper understanding of the inner mechanisms which lead to turbulent phenomena is needed. Turbulence theory deals with the noisy or irregular (unpredictable) behaviour that may be exhibited by a fluid system under specific conditions. There is as yet no complete theory of the origin of turbulence in various types of hydrodynamic flow. Although various conjectural approaches have been reported in this advanced century, it remains an unsolved problem. It should be noted that this kind of phenomena is completely unrelated to the loss of analiticity of solutions of the Navier-Stokes equations. Some results on the presence of singularities in the Navier-Stokes problem have been obtained recently (Caffarelli *et al.* , 1982). Nevertheless, the question of physical turbulence (also termed weak turbulence) is a different and previous problem. Weak turbulence theory deals with the transition from steady solutions to time-periodic ones and, eventually, to chaotic regimes. In fact, these theories do not consider more aggressive conditions over the fluid system. For example, extreme physical conditions like high negative pressure gradients (cavitation) are out of the scope of weak turbulence theories. Moreover, it seems that weak turbulence, which is extensively studied experimentally, is far from the situation in which solutions develop singularities. Although some authors continue to associate turbulence with the presence of singularities in the solutions of the Navier-Stokes equation, it should be pointed out that weak turbulence has not very much to do with these specific mathematical problems.

Some relevant changes have taken place in this century that could offer new hopes for a better understanding of turbulent phenomena. On the one hand, the general theory of dynamical systems has developed new theoretical tools which provide a deeper understanding of non-linear dynamics in physical systems. For example, center manifold theory and local bifurcation methods provide essential information on the behaviour of the fluid system near critical stages. This kind of methodology is usually termed weak non-linear analysis. Throughout this work, it will be seen how these non-linear phenomena can be linked with complex behaviour in fluid systems. In addition, the continuous improvement of computational devices has provided the possibility of simulating fluid dynamics problems with high accuracy. Computational fluid dynamics (cfd) offers the capability of simulating processes which would be otherwise impossible to recover experimentally. As a matter of fact, fluid flows observed in nature not only must be solutions of the equations, but must also be stable. This condition is no longer necessary in cfd. On the contrary, some cfd methodologies are capable of detecting unstable solutions not observed in the laboratory. Furthermore, unstable solutions, undetectable in experimental research, are sometimes the cause of the instabilization of basic flows. One of the main goals of cfd is to formulate numerical schemes able to approximate solutions for the Navier-Stokes equations. These schemes should be flexible in order to be easily applied in problems of different nature depending on their features (e.g. geometry and boundary conditions, etc...). In addition, the information obtained from the computations should not be restricted to a simple array of numerical data. In fact, the mathematical structure of the method should be useful for different purposes. From a physical point of view, it is essential not only to obtain accurate numerical approximations, but also to recover essential information hidden behind the results.

The general theory of dynamical systems (ds) is a good point of reference to analyze the complex behaviour of fluid systems. In fact, many physical mechanisms of fluid instabilities (pattern formation or turbulence, for example) can be understood from the point of view of bifurcation theory (bt) and related topics (Ruelle, 1989). In fact, chaotic dynamics in low-dimensional models systems may provide a fair explanation of turbulent phenomena. To put it briefly, turbulence could be interpreted like a spatio-temporal chaotic behaviour in infinite-dimensional dynamical systems. Unfortunately, the link between the theory of stability of fluid flows (also termed hydrodynamic stability) and ds theory is not always direct. From a pure mathematical point of view, the nature of the problems is completely different. On the one hand, the instabilities of fluid systems are essentially boundary value problems, for which the formalism of partial differential equations applies. On the other hand, bt and ds deal with finite dimensional systems, that is, ordinary differential equations. Most of the tools developed recently in the field of ds are only valid in the range of finite dimensional problems. Consequently, it is necessary to provide a connection (at least from a numerical point of view) between the two fields.

A wide variety of methods is available to obtain a simplification of an infinite-dimensional stability problem. In the second half of this century, some different modeling techniques were formulated. The first approach to the problem of bifurcation of a fluid flow was conjectured by Landau in 1944. Landau proposed an amplitude equation for the square of the perturbations from the basic solution. Although it was a brilliant idea (as was customary in Landau's works), it was not completely justified. In fact, Landau did not calculate the coefficients in his equation, which had to be computed *a posteriori*, so it was not a predictive analysis (Landau, 1944). A second step was taken by Stuart and Watson in 1960. Stuart postulated the form of the equation sought and, on introducing suitable Taylor series in the amplitude of the unstable mode, found the coefficients for the nonlinear terms (see Stuart, 1960 or Watson, 1960). From the late fifties on, a large body of literature on the quasi-linear stability problem appeared. Nevertheless, a formal mathematical justification for the formulation of these kind of equations had to wait for over three decades. In 1983, Coullet and Spiegel published a complete formalism for the computation of amplitude equations in general situations (not only in fluid dynamics problems). They made use of center manifold formalism and normal forms from ds theory and the essential conditions of applicability of the method (hypotheses related to the structure of the spectrum of the operators) were established (Coullet & Spiegel, 1983). In fact, the Stuart-Watson amplitude equations were only valid under the hypothesis of discrete spectrum of eigenvalues of the linear operator which leads the stability. For the continuous case, the most frequent in extended fluid dynamic systems, an alternative formulation was needed. At the end of the sixties, Newell, Whitehead and Segel independently proposed a first model of finite bandwidth instabilities (Newell & Whitehead, 1969). In this case, modulation of the amplitude in the spatial unbounded coordinates was considered. The new partial differential equation, also termed Ginzburg-Landau equation in theoretical physics because of its similarity to a result in superconductivity, was obtained under some *ad hoc* considerations of time-space scales. From that time on, this methodology has been very productive for the theoretical research of fluid instabilities. Nevertheless, a rigorous mathematical theory which asserts the reliability of the method does not exist. Recently, Eckhaus reported some important results about the dynamical properties of the Ginzburg-Landau equation (Eckhaus, 1993). The efficiency of these kinds of methods is strongly conditioned by whether the analysis is done near criticality or not. More recently, a quantitative analysis of the accuracy and reliability of the low dimensional models as representations of continuous systems was reported (Wittenberg & Holmes, 1997). These reports criticize the qualitative behaviour of the low-dimensional models in relation to the real problem. As a matter of fact, some low-dimensional models exhibit complex phenomena (like chaotic dynamics, for example), while the real system (integrated numerically in its exact form) does not present those features.

The continuous improvement of high speed processors and the development of faster numerical algorithms call for more sophisticated (and also more accurate) methodologies. For instance, spectral methods (sm) are a good alternative for the previous purposes. sm allow to approximate solutions of the continuous nonlinear system without a loss of information on the core dynamics of the problem under study. Moreover, the flexibility of the methods allows to translate directly the system of non-linear partial differential equations to systems of ordinary differential equations – that is, a finite-dimensional dynamical system which leads the time-dependence of the problem. Finally, the use of tools provided by the general theory of dynamical systems (center manifold theory, local bifurcation analysis, continuation methods, etc...) is now completely justified.

1.2 The Purpose of this Work

Under the perspectives described in the introduction, the main goal of the present work is to provide a simple methodology capable of translating the spatio-temporal dynamics of a fluid physical problem to an adequate dynamical system of amplitudes. There are many integration schemes and numerical libraries for the Navier-Stokes boundary value problem whose accuracy an reliability has been extensively checked. Nevertheless, it should be noted that normally, those schemes are not properly posed for other purposes other than pure spatio-temporal computation. In fact, they are very closed algorithms whose internal information may be very complicated to understand physically. Consequently, the core aim of the present task is not only to establish a regular formulation of the Navier-Stokes initial-boundary problem, but also to provide a connection with the main tools of dynamical systems theories. Therefore, the task will be carried out focusing the efforts on the theoretical physical results more than in the effectiveness of the numerical schemes We are mainly concerned with the core dynamics of the physical problem –this is, the stability of ordered structures, study of eigenvalues, prediction of bifurcations, etc. As a result, the numerical schemes presented here may not be very efficient from a computational cost point of view. Fortunately, the improvement of numerical processors and algorithmic libraries allows us to stop bothering with those technical problems.

The second chapter will be devoted to the weak formulation of the Navier-Stokes problem. Its purpose is to establish generally the mathematical frame in which the physical problems studied throughout the research will take place. In addition, the general framework of the Petrov-Galerkin (pg) weak formalism will be introduced. Throughout this section, the analysis will not be presented in great detail, referring technical difficulties and computational procedures to specific chapters or appendices.

In the third chapter, a first numerical test of the numerical pg scheme will be carried out. For this purpose, a classical problem of computational fluid dynamics will be considered. Moreover, due to the good efficiency of the formalism, not only the integration of the problem will be given, but a linear stability analysis of the system will also be compared with recent related works. At this stage, the power of dynamical systems tools in relation to pure numerical schemes will be emphasized.

Chapter four deals with the behaviour of a low-dimensional fluid model obtained by a direct truncation of the pg spectral approximations obtained in chapter three, in order to study the effects of non-linearities in the dynamical system of amplitudes. The model exhibits a route to chaotic regimes via universal period doubling, also termed Feigenbaum's scenario. Some specific numerical algorithms will be constructed in order to compute the period doublings with high accuracy. Again, the numerical tools constructed specifically for those computations will be explained in referred appendices.

The fifth chapter, which is the core part of the present work, is completely devoted to a comprehensive study of the stability of Taylor-Couette problem submitted to axial sliding effects. In this part of the research, the tools developed throughout the work will be used. For this purpose, pg schemes will be *ad hoc* modified for the geometry and boundary conditions of the problem. Analysis will focus on the complex behaviour of the physical system and the efforts will be devoted in order to extract the mathematical information obtained from our numerical algorithms. As a matter of fact, the linear stability analysis is complex enough to devote our efforts in a better understanding of the instability and bifurcation mechanisms of the physical system.

The sixth and last chapter will provide the theoretical framework in which pg schemes can be applied in the nonlinear stability analysis of the Taylor-Couette problem. Two different situations will be considered. First, the formulation of the steady bifurcations with $\mathsf{O}(2)$ symmetry in the framework of normal form theory will be provided. The system of differential equations which is needed for the computation of the coefficients of the normal form will be obtained. The numerical integration is, at the present stage, out of the scope of this work. Secondly, the case of steady bifurcation with $\mathsf{O}(2)\rightarrow\mathsf{SO}(2)$ symmetry breaking will be considered. The normal form of the bifurcation will be obtained by applying symmetry arguments, and the qualitative properties of secondary steady patterns will be predicted from the analysis. Finally, this work will end with a numerical check on the previous results. For this purpose, the pg scheme will be suitably modified in order to consider not only sliding effects but also an imposed axial pressure gradient. The numerical evidences obtained from concluding results will confirm that it is possible to recover steady bifurcations with an explicit $\mathsf{O}(2)$ symmetry breaking and that the generic bifurcation is 2-codimensional.

Chapter 2

Navier-Stokes Equations: Weak formalism

2.1 General Procedure

The non-dimensional Navier-Stokes equations of viscous incompressible fluids are considered:

$$\begin{aligned} \partial_t \mathbf{u} + (\mathbf{u}\cdot\nabla)\mathbf{u} &= \Delta\mathbf{u} - \nabla p && (2.1)\\ \nabla\cdot\mathbf{u} &= 0. && (2.2)\end{aligned}$$

These equations govern the dynamics of a fluid inside an open bounded subset $\Omega(\subset \mathbb{R}^n)$ with boundary Γ, where n may have the values 2 or 3. The unknown quantities are the components of the velocity field $\mathbf{u}(\mathbf{r},t)$ and the dynamic pressure $p(\mathbf{r},t)$. It should be noted that the process on non-dimensionalization (L–space, L^2/ν–time) of the problem carries out a system of non-dimensional control parameters which describe the global dynamics of the system. For our purposes, it will be only necessary to consider an abstract parameter R [1]. In addition, equations (2.1) and (2.2) are complemented with boundary conditions over Γ and the initial value prescription. For the sake of simplicity, in this section, homogeneous boundary conditions over Γ will only be considered

$$\mathbf{u}(\mathbf{r},t) = \mathbf{0}, \quad \forall\mathbf{r}\in\Gamma, \quad \forall t \tag{2.3}$$

and the initial value prescription

$$\mathbf{u}(\mathbf{r},0) = \mathbf{u}_0(\mathbf{r}) \quad (\forall\mathbf{r}\in\Omega) \tag{2.4}$$

For the mathematical setting of this problem, it is necessary to consider two different Hilbert spaces. First, the spectral space of divergence-free vector fields $\mathcal{H}_s$, which is a closed subspace of $\mathcal{L}^2(\Omega)^n$, is considered

$$\mathcal{H}_s = \{\mathbf{u}\in\mathcal{L}^2(\Omega)^n, \nabla\cdot\mathbf{u} = 0, \mathbf{u}\mid_\Gamma = 0\} \tag{2.5}$$

---

[1] Usually, this parameter is the Reynolds number $R = \frac{UL}{\nu}$, where U, L and ν are typical velocity, length and kinematic viscosity respectively, featuring the physical system.

where $\mathcal{L}^2(\Omega)^n$ is the space of square integrable functions over the n–dimensional domain, and $\mathbf{n}$ is the unit normal vector at each point over the boundary Γ. Secondly, the projection space $\mathcal{H}_p$ defined as follows

$$\mathcal{H}_p = \{\tilde{\mathbf{u}} \in \mathcal{H}_0^1(\Omega)^n, \nabla \cdot \tilde{\mathbf{u}} = 0\} \tag{2.6}$$

will be considered [2] In this case, $\mathcal{H}_0^1(\Omega)^n$ is a subspace of $\mathcal{L}^2(\Omega)^n$ whose functions have distributional square-integrable derivatives up to the first order, vanishing over the boundary. Our aim is to obtain a dynamical system from the previous initial boundary value problem. For this purpose, that the weak solution of the previous problem will be assumed as belonging to $\mathcal{H}_s$. The weak form of the Navier-Stokes equation is obtained by projecting equation (2.1) over the space $\mathcal{H}_p$. For the projection process, the standard hermitian product between integrable vector fields is considered

$$< \mathbf{a}, \mathbf{b} >= \int_\Omega \mathbf{a}^* \cdot \mathbf{b} d\Omega. \tag{2.7}$$

Therefore, the weak form of the Navier-Stokes equation will be

$$< \tilde{\mathbf{u}}, \partial_t \mathbf{u} > + < \tilde{\mathbf{u}}, (\mathbf{u} \cdot \nabla)\mathbf{u} >=< \tilde{\mathbf{u}}, \Delta \mathbf{u} > - < \tilde{\mathbf{u}}, \nabla p >, \quad \forall \tilde{\mathbf{u}} \in \mathcal{H}_p \tag{2.8}$$

One of the advantages of this formalism is that the final equations depend only on the velocity field $\mathbf{u}$. In fact, the pressure term $< \tilde{\mathbf{u}}, \nabla p >$ in equation (2.8) vanishes:

$$< \tilde{\mathbf{u}}, \nabla p >= \int_\Omega \tilde{\mathbf{u}}^* \cdot \nabla p d\Omega = \int_\Omega \nabla \cdot (\tilde{\mathbf{u}}^* p) d\Omega - \int_\Omega p \nabla \cdot \tilde{\mathbf{u}}^* d\Omega = \int_\Gamma (\tilde{\mathbf{u}}^* p) \cdot d\Gamma = 0$$

where Green's Theorem has been used. Notice that the condition for the last term in the previous equation to be zero is that $\tilde{\mathbf{u}}$ has only tangential component over the boundary Γ. Therefore, the method only requires this *inviscid* boundary condition on the test-projection functions of $\mathcal{H}_p$. In fact, some authors (Moser, Moin & Leonard, 1983) make use of this less restrictive condition . Nevertheless, our functions $\tilde{\mathbf{u}}$ belong to $\mathcal{H}_0^1(\Omega)^n$ and they vanish over the boundary Γ. Finally, the spatial dependence disappears and a dynamical system, which only involves $\mathbf{u}$, is obtained:

$$\frac{d}{dt}\mathcal{A}(\tilde{\mathbf{u}}, \mathbf{u}) = \mathcal{L}(\tilde{\mathbf{u}}, \mathbf{u}) + \mathcal{N}(\tilde{\mathbf{u}}, \mathbf{u}, \mathbf{u}), \quad \forall \tilde{\mathbf{u}} \in \mathcal{H}_p \tag{2.9}$$

where $\mathcal{A}$, $\mathcal{L}$ and $\mathcal{N}$ stand for the linear forms

$$\mathcal{A}(\mathbf{a}, \mathbf{b}) = \int_\Omega \mathbf{a}^* \cdot \mathbf{b} d\Omega \tag{2.10}$$

$$\mathcal{L}(\mathbf{a}, \mathbf{b}) = \int_\Omega \mathbf{a}^* \cdot \Delta \mathbf{b} d\Omega \tag{2.11}$$

$$\mathcal{N}(\mathbf{a}, \mathbf{b}, \mathbf{c}) = \int_\Omega \mathbf{a}^* \cdot [(\mathbf{b} \cdot \nabla)\mathbf{c}] d\Omega \tag{2.12}$$

---

[2] In fact, some authors only consider non-slip condition, this is, a subspace of $\mathcal{H}^1(\Omega)$. In this case, the functions do not require the vanishing condition over the boundary.

for all integrable vector fields $\mathbf{a}, \mathbf{b}$ and $\mathbf{c}$. Besides, the incompressibility condition (2.2) is identically satisfied.

This is the general procedure to obtain the weak form of the Navier-Stokes equations. Nevertheless, some *ad hoc* modifications must be done to set up the method in different problems. Nevertheless, such changes are only technical.

2.2 Fluid Driven by its Boundary

One of the possible methods to induce a motion in a contained fluid system consists in driving it by its boundary. The non-slip boundary condition ensures the local propagation on kinematic energy near the frontiers. As a result, the velocity field changes with respect to the spatio-temporal variables. Consequently, many interesting questions arise. First, it would be interesting to have information about the existence of attractors in the phase space of the associated dynamical system. These attractors may be represented by steady patterns, time-periodic structures or turbulent flows in the physical space. Secondly, the study of the stability of steady flows, represented by stationary points in the phase space, is necessary in order to predict *a priori* bifurcation processes and new structures. Theory related with the existence and stability of attractors of the Navier-Stokes equations has been developed by other authors (Temam, 1988), although the study of these features is out of the scope of the present work.

For previous purposes, weak formalism, suitably modified, explained in section 2.1 is the adequate framework. In this section, the weak formalism for non-homogeneous problems (driven boundary fluids) will be developed. The next section is devoted to the stability of the the solutions obtained by this method or by direct integration of the Navier-Stokes equations.

We consider again the Navier-Stokes equations for incompressible fluids in two or three dimensions

$$\partial_t \mathbf{u} + (\mathbf{u} \cdot \nabla)\mathbf{u} = \Delta \mathbf{u} - \nabla p \tag{2.13}$$

$$\nabla \cdot \mathbf{u} = 0 \tag{2.14}$$

defined in a closed subset Ω whose boundary is Γ. In addition, let us suppose that the velocity profile prescribed over Γ is given in the form

$$\mathbf{u}(\mathbf{r}, t) \,|_\Gamma = \mathbf{u}_\Gamma(\mathbf{r}), \quad \forall \mathbf{r} \in \Gamma \tag{2.15}$$

and the initial conditions are given by the equation (2.4). The methodology developed in section 2.1 is no longer valid in this case. The main reason is that the boundary conditions are not homogeneous. In spite of these differences, it is possible to avoid the problem easily. For this purpose, it will be supposed that the velocity field can be split up as a sum of two objects

$$\mathbf{u} = \mathbf{u}_h + \mathbf{u}_p. \tag{2.16}$$

On the one hand, $\mathbf{u}_p$ is a stationary solenoidal vector field which verifies the boundary condition (2.15). In fact, $\mathbf{u}_p$ can be obtained analytically by the use of the Stream-Function formalism. To sum it up:

$$\nabla \cdot \mathbf{u}_p = 0, \quad \mathbf{u}_p \mid_\Gamma = \mathbf{u}_\Gamma, \quad \mathbf{u}_p \mid_\Gamma \cdot \mathbf{n} = 0, \quad \partial_t \mathbf{u}_p = 0 \tag{2.17}$$

On the other hand, $\mathbf{u}_h$ is an unknown field which will be obtained by the weak formalism. To put it briefly, $\mathbf{u}_h$ will play here the role of $\mathbf{u}$ in section 2.1. Thus, $\mathbf{u}_h \in \mathcal{H}_s$, vanishing identically over Γ. The weak form of the problem will now be

$$< \tilde{\mathbf{u}}, \partial_t \mathbf{u}_h > + < \tilde{\mathbf{u}}, [(\mathbf{u}_h + \mathbf{u}_p) \cdot \nabla](\mathbf{u}_h + \mathbf{u}_p) > = < \tilde{\mathbf{u}}, \Delta(\mathbf{u}_h + \mathbf{u}_p) > \tag{2.18}$$

where the pressure term, which vanishes in the projection, has been already omitted. As a result, the dynamical system for the unknown field $\mathbf{u}_h$ is obtained

$$\frac{d}{dt}\mathcal{A}(\tilde{\mathbf{u}}, \mathbf{u}_h) = \mathcal{M}(\tilde{\mathbf{u}}, \mathbf{u}_h, \mathbf{u}_p) - \mathcal{N}(\tilde{\mathbf{u}}, \mathbf{u}_h, \mathbf{u}_h) + \mathcal{P}(\tilde{\mathbf{u}}, \mathbf{u}_p) \tag{2.19}$$

where $\mathcal{M}$ and $\mathcal{P}$ are defined as follows

$$\mathcal{M}(\tilde{\mathbf{u}}, \mathbf{u}_h, \mathbf{u}_p) = \mathcal{L}(\tilde{\mathbf{u}}, \mathbf{u}_h) - \mathcal{N}(\tilde{\mathbf{u}}, \mathbf{u}_h, \mathbf{u}_p) - \mathcal{N}(\tilde{\mathbf{u}}, \mathbf{u}_p, \mathbf{u}_h) \tag{2.20}$$

$$\mathcal{P}(\tilde{\mathbf{u}}, \mathbf{u}_p) = \mathcal{L}(\tilde{\mathbf{u}}, \mathbf{u}_p) - \mathcal{N}(\tilde{\mathbf{u}}, \mathbf{u}_p, \mathbf{u}_p) \tag{2.21}$$

where the notation described in equations (2.10), (2.11) and (2.12) has been used. The splitting in equation (2.19) has been carried out in order to identify the different nature of each term. First, $\mathcal{M}$ stands for the part of the equation which depends linearly on the unknown field $\mathbf{u}_h$. Secondly, $\mathcal{P}$ is the forcing term which only depends on the solenoidal field $\mathbf{u}_p$. Finally, $\mathcal{N}$ represents the non-linear part in $\mathbf{u}$, also called convective term.

2.3 Hydrodynamic Stability

Yet not every solution of the equations of motion, even if it is exact, can actually occur in Nature. The flows which appear in Nature, must not only obey the equations of fluid dynamics, but must also be stable. This is the essential principle of hydrodynamic stability (hs). In fact, not only is of physical interest to obtain solutions for the Navier-Stokes equations, but also to study their stability with respect to perturbations which may arouse the generation of new patterns, oscillatory phenomena and, eventually, turbulent stages. Mathematically, the problem of the hs of a steady flow may be very complicated. The geometry and symmetries of the system can be of great aid simplifying the problem. This section deals with the general setting of the problem of hs from the standpoint of dynamical systems theory. For this purpose, weak formalism, explained in previous section is the adequate frame.

Consider again a fluid system under the same hypotheses stated in previous sections. Moreover, assume that a steady solution $\mathbf{v}_B$ is known by analytical or weak formalism methods. Thus

$$(\mathbf{v}_B \cdot \nabla)\mathbf{v}_B = \Delta \mathbf{v}_B - \nabla p_B, \quad \nabla \cdot \mathbf{v}_B = 0 \tag{2.22}$$

where, p_B is the steady pressure field. In order to study the stability of the fluid system, the flow $\mathbf{v}_B$ and the pressure field p_B are simultaneously perturbed with a time-dependent vector field $\mathbf{u}(\mathbf{r}, t)$ and a time-dependent scalar field $p'(\mathbf{r}, t)$, respectively. As a result, the perturbed system is

$$\mathbf{v}(\mathbf{r}, t) = \mathbf{v}_B(\mathbf{r}) + \mathbf{u}(\mathbf{r}, t), \quad p(\mathbf{r}, t) = p_B(\mathbf{r}) + p'(\mathbf{r}, t) \tag{2.23}$$

where $\mathbf{u}$ must be a solenoidal field which vanishes over the boundary of the fluid system

$$\nabla \cdot \mathbf{u} = 0, \quad \mathbf{u}(\mathbf{r}, t) \mid_\Gamma = \mathbf{0}, \quad \forall t \tag{2.24}$$

Formal substitution of the perturbed fields (2.23) in equation (2.1) leads to the law which governs the dynamics of the perturbation

$$\partial_t \mathbf{u} + [(\mathbf{v}_B + \mathbf{u}) \cdot \nabla](\mathbf{v}_B + \mathbf{u}) = \Delta(\mathbf{v}_B + \mathbf{u}) - \nabla(p_B + p'). \tag{2.25}$$

Formally, weak solutions to the problem described by equations (2.24) and (2.25) can be obtained using the formalism developed in section 2.2. The integration of the previous problem would lead to a complete description of the evolution of the perturbation field $\mathbf{u}$. Unfortunately, this task is not always feasible. In some particular problems, whose geometric features require an special treatment, an alternative is needed. In fact, hs only deals with questions about the stability of the basic flow. The prediction and computation of secondary flows which appear after the bifurcation are, at the present stage, out of the scope of linear hydrodynamic stability [3].

Under the hypothesis of infinitesimal perturbations, the stability of a basic flow is governed by the lowest order terms in equation (2.25). Consequently, the non-linear term $(\mathbf{u} \cdot \nabla)\mathbf{u}$ can be neglected as a first approximation for our practical purposes. As a result, the mathematical problem simplifies considerably. The linearization process leads to a simpler equation

$$\partial_t \mathbf{u} = \Delta \mathbf{u} - (\mathbf{v}_B \cdot \nabla)\mathbf{u} - (\mathbf{u} \cdot \nabla)\mathbf{v}_B - \nabla p', \tag{2.26}$$

where identity (2.22) was used. In contrast with equation (2.25), (2.26) is a quasi-linear partial differential equation which is easier to solve. A suitable method is needed not only to compute the presence of bifurcations, but also to extract essential information of physical interest, like spatial periodicity of secondary patterns, velocities of propagation, etc..., from the system of equations (2.24) and (2.26). At the present stage, many different approaches to solve the problem are available. As a matter of fact, the pressure term $\nabla p'$ plays a crucial role. One possible option is to annihilate the pressure term making use of the stream-function formalism for the perturbation. This procedure leads to the usually termed Orr-Sommerfeld-Squire equations (see Drazin & Reid, 1981 or Canuto *et al.* , 1988). From a numerical point of view, the boundary value problem associated with the Orr-Sommerfeld formulation may have convergence problems (Mercader *et al.* , 1991). In fact, the previous formulation based on potentials or similar techniques (Marqués, 1990) lead to high order eigenvalue problems constrained to low

---

[3] We do not consider here weakly non-linear theories which provide more information in bifurcation processes.

order boundary conditions. As a result, numerical instabilities may appear in the computation of eigenvalues of the operators. Perhaps, a more compact formulation may be provided making use of Petrov-Galerkin weak formalism. The main purpose is not only to construct a suitable scheme for the linear stability analysis, but also to use it for the nonlinear integration of the problem under study.

2.3.1 Petrov-Galerkin Scheme

It is possible to span the Hilbert spaces $\mathcal{H}_s$ and $\mathcal{H}_p$ of section 2.1 with a suitable set of solenoidal bases. In some cases, those bases may coincide–that is, $\mathcal{H}_s$ and $\mathcal{H}_p$ are the same functional space. If it is the case, the projection process which leads to the weak form of the problem is usually termed Galerkin scheme. Nevertheless, for computational purposes, it is necessary to select a modified basis in $\mathcal{H}_p$ with respect to the set of functions which spans $\mathcal{H}_s$. Sometimes, this slight modification is needed to take advantage from orthogonality properties between the two sets. In this situation, the projection process is properly called Petrov-Galerkin scheme.

Let $\mathcal{H}_s$ and $\mathcal{H}_p$ be two function spaces spanned by two sets of solenoidal fields $\{\mathbf{u}_\beta\}$ and $\{\tilde{\mathbf{u}}_\alpha\}$, respectively:

$$\mathcal{H}_s = \mathrm{Span}\{\mathbf{u}_\beta\}, \quad \mathcal{H}_p = \mathrm{Span}\{\tilde{\mathbf{u}}_\alpha\}.$$

In order to obtain a dynamical system of amplitudes from the problem (2.26), we suppose that our unknown perturbation field can be expressed as a linear combination of the set of functions $\mathcal{H}_s$

$$\mathbf{u} = \sum_\beta a_\beta(t)\mathbf{u}_\beta(\mathbf{r}), \quad \forall \mathbf{u}_\beta \in \mathcal{H}_s \tag{2.27}$$

where the amplitudes a_β are related with the time evolution of $\mathbf{u}$. After a formal substitution of expression (2.27) in equation (2.26), we proceed to project it over each element of $\mathcal{H}_p$ leading to a system of ordinary differential equations

$$\frac{d}{dt}\mathcal{A}(\tilde{\mathbf{u}}_\alpha, \mathbf{u}) = \mathcal{M}(\tilde{\mathbf{u}}_\alpha, \mathbf{u}) \quad \forall \mathbf{u}_\alpha \in \mathcal{H}_p \tag{2.28}$$

where the elements $\mathcal{A}$ and $\mathcal{M}$ are

$$\mathcal{A}(\tilde{\mathbf{u}}_\alpha, \mathbf{u}) =< \tilde{\mathbf{u}}_\alpha, \sum_\beta a_\beta \mathbf{u}_\beta > \tag{2.29}$$

$$\mathcal{M}(\tilde{\mathbf{u}}_\alpha, \mathbf{u}) =< \tilde{\mathbf{u}}_\alpha, \Delta \sum_\beta a_\beta \mathbf{u}_\beta - (\mathbf{v}_B \cdot \nabla) \sum_\beta a_\beta \mathbf{u}_\beta - [(\sum_\beta a_\beta \mathbf{u}_\beta) \cdot \nabla]\mathbf{v}_B > \tag{2.30}$$

The system (2.28) can be expressed more explicitly in the following form

$$\mathrm{A}_{\alpha\beta}\dot{a}_\beta = \mathrm{M}_{\alpha\beta}a_\beta \tag{2.31}$$

or

$$\dot{a}_\beta = \mathrm{S}_{\alpha\beta} a_\beta, \tag{2.32}$$

where $\mathrm{S}_{\alpha\beta} = \mathrm{A}^{-1}_{\alpha\gamma} M_{\gamma\beta}$ and where Einstein's convention of addition with respect to repeated indexes has been used. Besides, the matrix elements $\mathrm{A}_{\alpha\beta}$ and $\mathrm{M}_{\alpha\beta}$ are defined as follows

$$\mathrm{A}_{\alpha\beta} =< \tilde{\mathbf{u}}_\alpha, \mathbf{u}_\beta >, \quad \mathrm{M}_{\alpha\beta} =< \tilde{\mathbf{u}}_\alpha, \Delta\mathbf{u}_\beta - (\mathbf{v}_B \cdot \nabla)\mathbf{u}_\beta - (\mathbf{u}_\beta \cdot \nabla)\mathbf{v}_B > \tag{2.33}$$

System (2.32) represents the temporal evolution of the perturbation field. In fact, $a_\alpha = 0$ is always a solution of the previous system, representing the trivial solution $\mathbf{u} = 0$ of (2.26). Therefore, the stability of the basic flow $\mathbf{v}_B$ will be implicitly conditioned by the spectrum of eigenvalues of the matrix $\mathrm{S}_{\alpha\beta}$. So far, the general frame has been considered. Depending on the geometry, symmetries and dimension of the problem, the previous formulation may be prohibitive from a numerical point of view. One of the most frequently used methods to reduce computational cost is the usually termed *normal mode analysis*. This method considers specific functional structure of the perturbation field $\mathbf{u}$ depending on the geometric features of the problem. Typically, the perturbation is supposed to depend exponentially on the time variable and periodically in the extended (unbounded) spatial ones

$$\mathbf{u}(\mathbf{r}_u, \mathbf{r}_b, t) = \mathbf{v}(\mathbf{r}_b)\mathrm{e}^{\lambda t + \mathrm{i}\mathbf{k}\cdot\mathbf{r}_u}.$$

In the previous expression, $\mathbf{r}_u$ and $\mathbf{r}_b$ stand for the unbounded and bounded spatial variables, respectively. On the other hand, $\mathbf{k}$ denotes the wave number (which may be real or integer, depending on the symmetries of the problem) featuring the spatial periodicity of the perturbation. Besides, $\mathbf{v}$ is a vector field that depends on the bounded spatial variables and which needs a special treatment. The exponential factor λ is complex in the general case, and the sign of its real part will lead the linear stability of the basic flow. The exponential structure of the time dependence is justified by the differential operator ∂_t whose integration would lead to the exponentiation of the matrix S in the general frame. This kind of analysis greatly simplifies the computations because of the linearity of equation (2.26). On formal substitution of those exponential structures in the perturbation equation, each spatial mode $\mathbf{k}$ decouples leading to a system of independent boundary value problems for the unknown field $\mathbf{v}$ (see Lin, 1955 or Chandrasekhar, 1961). In fact, this kind of analysis will be used throughout chapters 5 and 6 taking advantage of the symmetries of the particular problem under study (Taylor-Couette problem). Unfortunately, when the physical system has no symmetries, the previous general frame of analysis is needed. This is exactly what is going to be carried out in next chapter for the regularized flow in a square cavity.

Chapter 3

Regularized Driven Cavity Flow

3.1 Introduction

For several years, steady flow in a square cavity has become a popular example for testing and comparing numerical methods in computational fluid mechanics. The simplicity of the problem makes it possible to check easily numerical schemes of integration for the Navier-Stokes equations of incompressible fluids. In fact, two different versions of the problem can be considered. In a first version, the fluid velocity is zero on three sides of the square and is tangent to the fourth side with a uniform profile. This configuration (also termed Driven Cavity Flow, see Fig. 3.1) has been analyzed extensively by many authors (see Gupta & Manohar, 1979, for example) with finite-difference schemes. Because of the discontinuity of the velocity vector field at the corners of the driven side, the solution of the Navier-Stokes equations is singular at these points (the vorticity is infinite). As a matter of fact, it is difficult to measure with precision the effect of a singularity on the accuracy of a solution. This is particularly true when the mesh is refined so that the computation points are drawn nearer and nearer to the corners even if the values of the vorticity at these points are not involved in the numerical scheme as is usual for finite-difference approximations.

A regularized alternative was proposed by Bourcier and Francois in 1969. They considered the same problem but with a regularized profile instead of a uniform one. This

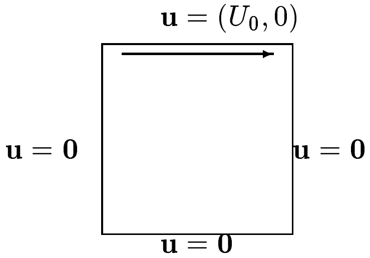

Figure 3.1: Geometrical configuration of the Driven Cavity Flow. On note the discontinuities of the velocity vector field in the top corners.

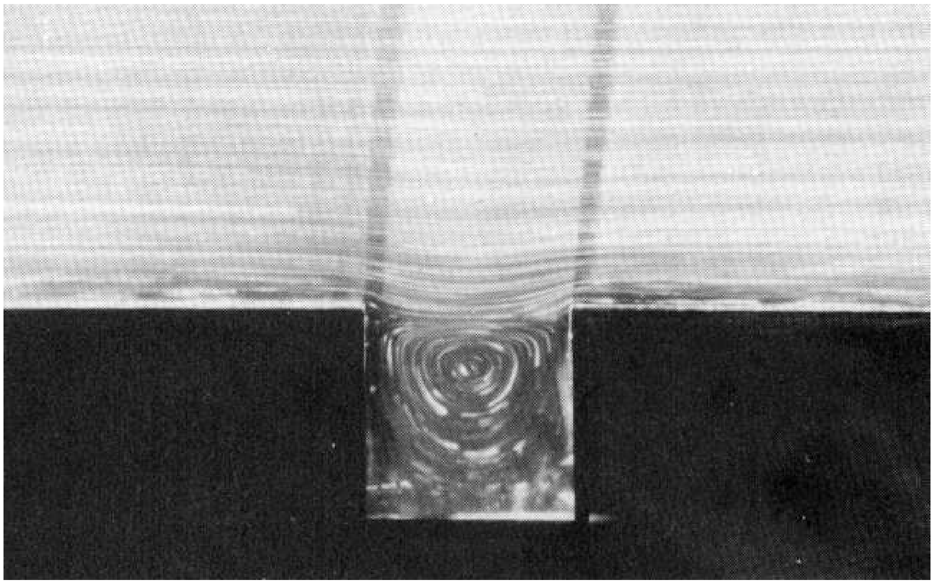

Figure 3.2: Experimental grooved channel problem (from Taneda, 1979).

problem is commonly termed Regularized Driven Cavity Flow (`rdcf`). In this chapter, not only the numerical schemes used throughout the present work will be tested in this second case, but also new results related to the stability of the problem will be provided.

The initial motivation of this theoretical (but more physical) problem lies on a deeper understanding of instability processes in grooved channels (Taneda, 1979). From a physical point of view, it is interesting to study the effect of cavities in channel flows (see figure 3.2). The presence of this kind of irregularities in the boundary profile may affect the stability of the global flow. From a mathematical point of view, the advantages of this problem lie on the regularity conditions that must be imposed on the boundary. This fact makes the essential distinction between the `rdcf` and the Driven Cavity Flow (`dcf`) which has singularities and can not be analyzed with Galerkin methods.

The grooved channel problem was first numerically studied by Korczak & Patera, 1986, with spectral elements methods, although a former integration model can be found in Peyret & Taylor, 1983. Nevertheless, the previous analyses were not concerned with the stability of the flow. More recently (Shen, 1991), a comprehensive analysis has been reported making use of temporal-evolution schemes in order to detect instabilities of the steady flow. As a matter of fact, the absence of symmetries in `rdcf` makes it impossible to simplify its analysis in order to compute steady solutions. The `rdcf` is a pure non-linear two-dimensional problem in which the two coordinates must be integrated simultaneously being impossible to compute steady solutions by analytical methods.

This chapter is devoted to the stability analysis of the `rdcf` as a first test of the Petrov-Galerkin formulation in primitive variables. For this purpose, the weak formalism explained in chapter 2 will be used. First, the steady solution for a wide range of Reynolds numbers will be computed numerically. This will be done using a simple continuation algorithm. Secondly, the stability of the solution will be studied making use of the linear

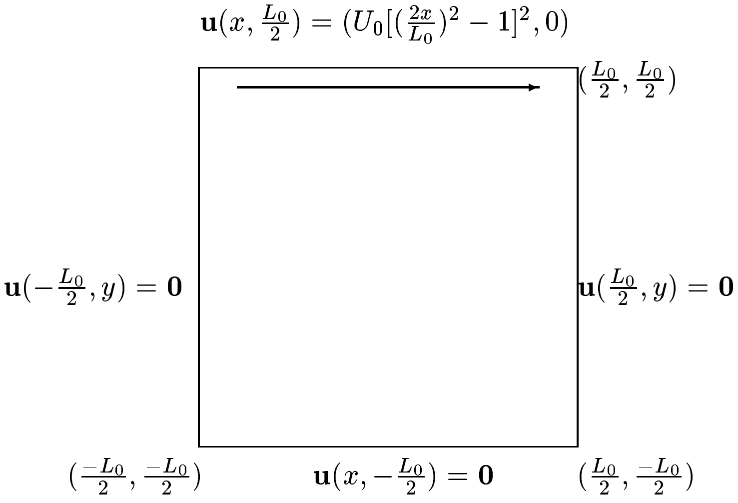

Figure 3.3: Physical configuration of the Regularized Driven Cavity Flow

criteria of eigenvalues. Some comparison with former works will be provided in order to focus the power of hydrodynamic stability tools in comparison with temporal-evolution methods.

3.2 Physical Description

The rdcf considers a two-dimensional square box of side length L_0 filled with an incompressible fluid of kinematic viscosity ν. The velocity profile is prescribed over the boundary. On the one hand, the top side is moving in the horizontal direction with a regularized law over the top corners $\mathbf{u}(x, L_0/2) = (U_0[(2x/L_0)^2 - 1]^2, 0)$. On the other hand, the velocity field vanishes over the left, right and bottom sides (see figure 3.3).

All variables will be rendered dimensionless, using $L_0/2$, $2\nu/L_0$ as the unit length and velocity respectively. Therefore, in the frame of chapter 2, the fluid domain is $\Omega = [-1, 1] \times [-1, 1]$, and the boundary is the union of the following sets:

$$\begin{array}{ll} \Gamma_1 = \{(x, y) \in \mathbb{R}^2; x = 1, y \in [-1, 1]\} & \Gamma_2 = \{(x, y) \in \mathbb{R}^2; x \in [-1, 1], y = 1\} \\ \Gamma_3 = \{(x, y) \in \mathbb{R}^2; x = -1, y \in [-1, 1]\} & \Gamma_4 = \{(x, y) \in \mathbb{R}^2; x \in [-1, 1], y = -1\}. \end{array}$$

That is, $\Gamma = \bigcup_{i=1}^{4} \Gamma_i$. Besides, the non-dimensional boundary conditions are now:

$$\mathbf{u}\,|_{\Gamma_1,\Gamma_3,\Gamma_4} = \mathbf{0} \qquad \mathbf{u}\,|_{\Gamma_2} = (R(x^2 - 1)^2, 0) \tag{3.1}$$

where R is the Reynolds number $R = L_0 U_0 / 2\nu$ (which differs by a factor $\frac{1}{2}$ with respect to the Reynolds number considered by other authors), and U_0 is the maximum of the imposed velocity on the side Γ_2. It should be noted that the velocity profile imposed over Γ_2 is continuous and differentiable over the corners $(-1, 1)$ and $(1, 1)$.

3.3 Mathematical Setting

Our aim is to apply to this particular problem the formalism developed in chapter 2. For this purpose, it is necessary to identify each element. First of all, we are dealing with a two-dimensional problem in Cartesian coordinates. Moreover, the physical configuration does not provide any kind of symmetry which could make the analysis simpler. Besides, the boundary conditions are not homogeneous. As a result, we must use the method explained in section 2.2. For this purpose, we will suppose that the solution of our problem can be split up in two parts: $\mathbf{u}_\mathrm{h}$ and $\mathbf{u}_\mathrm{p}$. On the one hand, $\mathbf{u}_\mathrm{p}$ is a solenoidal field which satisfies the boundary conditions over the four sides Γ_1, Γ_2, Γ_3 and Γ_4. On the other hand, $\mathbf{u}_\mathrm{h}$ is the homogeneous weak approximation which vanishes at the previous boundaries:

$$\mathbf{u} = \mathbf{u}_\mathrm{h} + \mathbf{u}_\mathrm{p} \qquad \nabla \cdot \mathbf{u}_\mathrm{h} = 0 \qquad \nabla \cdot \mathbf{u}_\mathrm{p} = 0 \tag{3.2}$$

$$\mathbf{u}_\mathrm{p}\,|_{\Gamma_1,\Gamma_3,\Gamma_4} = \mathbf{0} \quad \mathbf{u}_\mathrm{p}\,|_{\Gamma_2} = R[x^2-1]^2\mathbf{i} \quad \mathbf{u}_\mathrm{h}\,|_{\Gamma} = \mathbf{0} \tag{3.3}$$

The non-homogeneous part $\mathbf{u}_\mathrm{p}$ can be obtained analytically from the curl of a a pseudo-stream function ψ defined over Ω. A detailed explanation of the computation of ψ and $\mathbf{u}_\mathrm{p}$ can be found in appendix A.1. In this case, a solenoidal vector field compatible with the boundary conditions is

$$\mathbf{u}_\mathrm{p} = \frac{R}{4}(3y-1)(y+1)(x^2-1)^2\mathbf{i} - Rx(y+1)(y^2-1)(x^2-1)\mathbf{j} \tag{3.4}$$

The next step is to consider the unknown field $\mathbf{u}_\mathrm{h}$ as an element of the space $\mathcal{H}_s$ where our weak approximation will be expanded. Regarding the procedure explained in section 2.2, the weak form of the problem will be

$$< \tilde{\mathbf{u}}, \partial_t(\mathbf{u}_\mathrm{h} + \mathbf{u}_\mathrm{p}) + (\mathbf{u}_\mathrm{h} + \mathbf{u}_\mathrm{p}) \cdot \nabla(\mathbf{u}_\mathrm{h} + \mathbf{u}_\mathrm{p}) - \Delta(\mathbf{u}_\mathrm{h} + \mathbf{u}_\mathrm{p}) >= 0, \quad \forall \tilde{\mathbf{u}} \in \mathcal{H}_p \tag{3.5}$$

3.4 Basis for $\mathcal{H}_s$ and $\mathcal{H}_p$: The Petrov-Galerkin Scheme

The spaces $\mathcal{H}_s$ and $\mathcal{H}_p$ will be spanned with solenoidal vector fields whose structure is previously conditioned by the divergence-free constraint in cartesian coordinates. Therefore, a possible set of bases is

$$\mathcal{H}_p = \mathrm{Span}\{\tilde{\mathbf{u}}_{ij}\} \quad \mathcal{H}_s = \mathrm{Span}\{\mathbf{u}_{kl}\} \tag{3.6}$$

where

$$\tilde{\mathbf{u}}_{ij} = (-\tilde{f}_i(x)\tilde{g}'_j(y), \tilde{f}'_i(x)\tilde{g}_j(y)) \quad \mathbf{u}_{kl} = (-f_k(x)g'_l(y), f'_k(x)g_l(y)) \tag{3.7}$$

where $'$ means derivative with respect to the variable of the function in each case. The previous set of functions identically satisfies the divergence-free condition. Furthermore, they are bases of the Hilbert spaces $\mathcal{H}_s$ and $\mathcal{H}_p$ respectively. As a result, it is possible to expand our weak approximation $\mathbf{u}_\mathrm{h}$ as a linear combination of the functions $\mathbf{u}_{kl}$

$$\mathbf{u}_\mathrm{h}(x,y,t) = \sum_{k,l} a_{kl}(t)\mathbf{u}_{kl}(x,y) \tag{3.8}$$

It will be assumed that $\tilde{\mathbf{u}}_{ij}$ and $\mathbf{u}_{kl}$ are continuous and differentiable vector fields defined in Ω such that their components vanish over the boundary Γ. The selection criteria of the functions $\tilde{f}_i$, $\tilde{g}_j$, f_k and g_l depends on the geometry of the problem and the boundary conditions. On the one hand, the functions f_k and g_l contain orthogonal polynomials factorized with a suitable low order binomial factor which ensures the boundary conditions. On the other hand, the functions $\tilde{f}_i$ and $\tilde{g}_j$ have the same factors. In addition, they are factorized with the weight function associated with the orthogonal polynomials used in the scheme. Depending on this weight function, the bases $\mathbf{u}_{kl}$ and $\tilde{\mathbf{u}}_{ij}$ are not exactly the same. This scheme is not exactly a Galerkin one but it is more properly called Petrov-Galerkin. This method has been used before by other authors in different problems with different geometries (Moser, Moin & Leonard, 1983), (Canuto *et al.* , 1988).

For this problem, we have selected Tchebychev polynomials whose associated weight function is $\omega(x) = (1-x^2)^{-1/2}$. As a result, the component functions f_k, g_l, $\tilde{f}_i$ and $\tilde{g}_j$ are

$$\tilde{f}_i(x) = (1-x^2)^{3/2}T_i(x) \quad \tilde{g}_j(y) = (1-y^2)^{3/2}T_j(y) \quad (0 \le i,j \le M) \tag{3.9}$$

$$f_k(x) = (1-x^2)^2T_k(x) \quad g_l(y) = (1-y^2)^2T_l(y) \quad (0 \le k,l \le M), \tag{3.10}$$

where M is the order of our spectral approximation.

3.5 Dynamical System of Amplitudes

Substituting the spectral approximation (3.8) into the weak form of the Navier-Stokes equation (3.5), we obtain a dynamical system for the amplitudes a_{kl}

$$A_{ijkl}\frac{da_{kl}}{dt} = (B_{ijkl} - C^{\mathrm{R}}_{ijkl})a_{kl} - N_{ijklmn}a_{kl}a_{mn} + b^{\mathrm{R}}_{ij}, \quad (0 \le i,j \le M) \tag{3.11}$$

where we have used the Einsteinś convention of addition with respect to repeated indexes and where the index R stands for those terms which depend implicitly on the Reynolds number. The previous coefficients which appear in the last equation are the following matrix elements:

$$A_{ijkl} =< \tilde{\mathbf{u}}_{ij}, \mathbf{u}_{kl} >, \quad (0 \le i,j,k,l \le M) \tag{3.12}$$

$$B_{ijkl} =< \tilde{\mathbf{u}}_{ij}, \Delta\mathbf{u}_{kl} >, \quad (0 \le i,j,k,l \le M) \tag{3.13}$$

$$C^{\mathrm{R}}_{ijkl} =< \tilde{\mathbf{u}}_{ij}, (\mathbf{u}_{kl}\cdot\nabla)\mathbf{u}_{\mathrm{p}} + (\mathbf{u}_{\mathrm{p}}\cdot\nabla)\mathbf{u}_{kl} >, \quad (0 \le i,j,k,l \le M) \tag{3.14}$$

$$N_{ijklmn} =< \tilde{\mathbf{u}}_{ij}, (\mathbf{u}_{kl}\cdot\nabla)\mathbf{u}_{mn} >, \quad (0 \le i,j,k,l,m,n \le M) \tag{3.15}$$

and the forcing term is

$$b^{\mathrm{R}}_{ij} =< \tilde{\mathbf{u}}_{ij}, \Delta\mathbf{u}_{\mathrm{p}} - (\mathbf{u}_{\mathrm{p}}\cdot\nabla)\mathbf{u}_{\mathrm{p}} > \quad (0 \le i,j \le M) \tag{3.16}$$

These objects are explicitly analyzed in appendix A.1. Symbolically, the dynamical system can be expressed as follows

$$A\dot{a} = L_{\mathrm{R}}a - N(a,a) + b_{\mathrm{R}} \tag{3.17}$$

where L_{R} stands for a linear operator which depends on a control parameter R, N is a bilinear form acting over a and b_{R} is a time-independent forcing term due to the non-homogeneous boundary condition.

3.6 Steady Solutions

For an arbitrary value of R, the stationary solutions of our problem can be obtained by equating the right-hand side of (3.17) to zero. This provides an non-linear system of algebraic equations whose solutions depend implicitly on R [1],

$$g(a,\mathrm{R}) = L_{\mathrm{R}}a - N(a,a) + b_{\mathrm{R}} = 0, \tag{3.18}$$

where the explicit structure of $g(a,\mathrm{R})$ is

$$g_{ij}(a,\mathrm{R}) = (B_{ijkl} - C^{\mathrm{R}}_{ijkl})a_{kl} - N_{ijklmn}a_{kl}a_{mn} + b^{\mathrm{R}}_{ij}, \quad (0 \le i,j \le M) \tag{3.19}$$

The system (3.18) can be solved numerically, making use of an iterative Newton-Raphson algorithm (Keller, 1977). For this purpose, starting from an initial point a^0_{ij} representing a steady solution for some value of R, a forward Euler's predictor point $a^{1/2}_{ij}$ is obtained locally over the branch $g(a,\mathrm{R}) = 0$, which always exists, provided that $\partial_{\mathrm{R}} g \neq 0$ (implicit function theorem)

$$a^{1/2}_{ij} = a^0_{ij} + (\partial_{\mathrm{R}} g)_{ij}\delta\mathrm{R}. \tag{3.20}$$

The previous expression provides a first approximation of the steady solution for the slightly increased $\mathrm{R} + \delta\mathrm{R}$ Reynolds number. This predicted value is then corrected, being used as the starting iteration point for the Newton-Raphson algorithm

$$a^{(n+1)}_{ij} = a^{(n)}_{ij} - [Dg(a^{(n)})]^{-1}_{ijkl}[g(a^{(n)})]_{kl}, \tag{3.21}$$

where Dg is the Jacobian matrix of the field g evaluated at the n^{th}-iteration point

$$[Dg(a^{(n)})]_{ijkl} = B_{ijkl} - C^{\mathrm{R}}_{ijkl} - N_{ijklpq}a^{(n)}_{pq} - N_{ijmnkl}a^{(n)}_{mn} + b^{\mathrm{R}}_{ij}, \quad (0 \le i,j \le M) \tag{3.22}$$

The convergence of the method depends strongly on the basin of attraction of the stationary point in phase space. The presence of neighboring numerical branches depends on the truncation order of the spectral approximation. In any case, as long as the number of modes is increased, it seems to be only a stationary branch which is easy to follow for a wide range of values of the control parameter R. By increasing the parameter R from zero, the steady solutions can be obtained. Some particular cases are depicted in figures 3.4, 3.5

---

[1] Provided that the Implicit Function Theorem applies.

and 3.6. From definitions (3.3) and (3.8), the stationary velocity field will be expressed as follows

$$\mathbf{u} = \mathbf{u}_p + \sum_{k=1}^{M}\sum_{l=1}^{M} a_{kl}^0 \mathbf{u}_{kl}(x,y), \tag{3.23}$$

where the coefficients a_{kl}^0 are the coordinates of the stationary point computed previously. The stream function of the problem is

$$\Psi = \psi(x,y) + \sum_{k=1}^{M}\sum_{l=1}^{M} a_{kl}^0 (x^2-1)^2(y^2-1)^2 T_k(x) T_l(y). \tag{3.24}$$

The vorticity field, which measures the local torsion, will be obtained evaluating the curl on $\mathbf{u}$

$$\omega_{\mathbf{k}} = (\nabla \times \mathbf{u})_{\mathbf{k}} = \partial_x \mathbf{u}_y - \partial_y \mathbf{u}_x = \sum_{k=1}^{M}\sum_{l=1}^{M} a_{kl}^0 [f_k''(x) g_l(y) + f_k(x) g_l''(y)] + \nabla \times \mathbf{u}_p \tag{3.25}$$

From the previous pictures, the progressive increasing of the size of the vortices which appear near the corners can be observed, as well as the clear distinction between two different zones of vorticity. On the top center part, a high clockwise vorticity can be observed. This is produced by the horizontal profile of the velocity imposed on the top side of the box. On the top right part, a high counter clockwise vorticity is present. This has been produced because of the collision of an almost horizontal jet with the right side of the box. An almost circular crown around the center vortex can be observed as a constant low vorticity zone. The velocity fields represented in the figures have been normalized to the maximum value in each case.

3.7 Linear Stability of the Steady Solutions

Provided that the matrix A in equation (3.17) is non-singular, the dynamical system of amplitudes can be expressed in the following form

$$\dot{a} = f(a, \mathrm{R}) \tag{3.26}$$

where the vector field f is

$$f(a, \mathrm{R}) = A^{-1}[L_{\mathrm{R}} a - N(a,a) + b_{\mathrm{R}}] \tag{3.27}$$

Let a_0 be a solution of the equation $f(a, \mathrm{R}) = 0$ for $\mathrm{R} = \mathrm{R}_0$. The stability of a_0 will be governed by the spectrum of eigenvalues of the Jacobian matrix of f evaluated at the point (a_0, R_0)

$$J = D_a f(a, r) \mid_{(a_0, \mathrm{R}_0)} \tag{3.28}$$

Let $\mathrm{Spec}\{J\} = \{\lambda \in \mathbb{C} \mid det(J - \lambda \mathrm{I}) = 0\}$ be the spectrum of the matrix J and λ_M its eigenvalue with maximum real part. Then, the basic flow, represented by the stationary solution a_0 in the phase space, will loss its stability if $\mathrm{Re}\lambda_M > 0$.

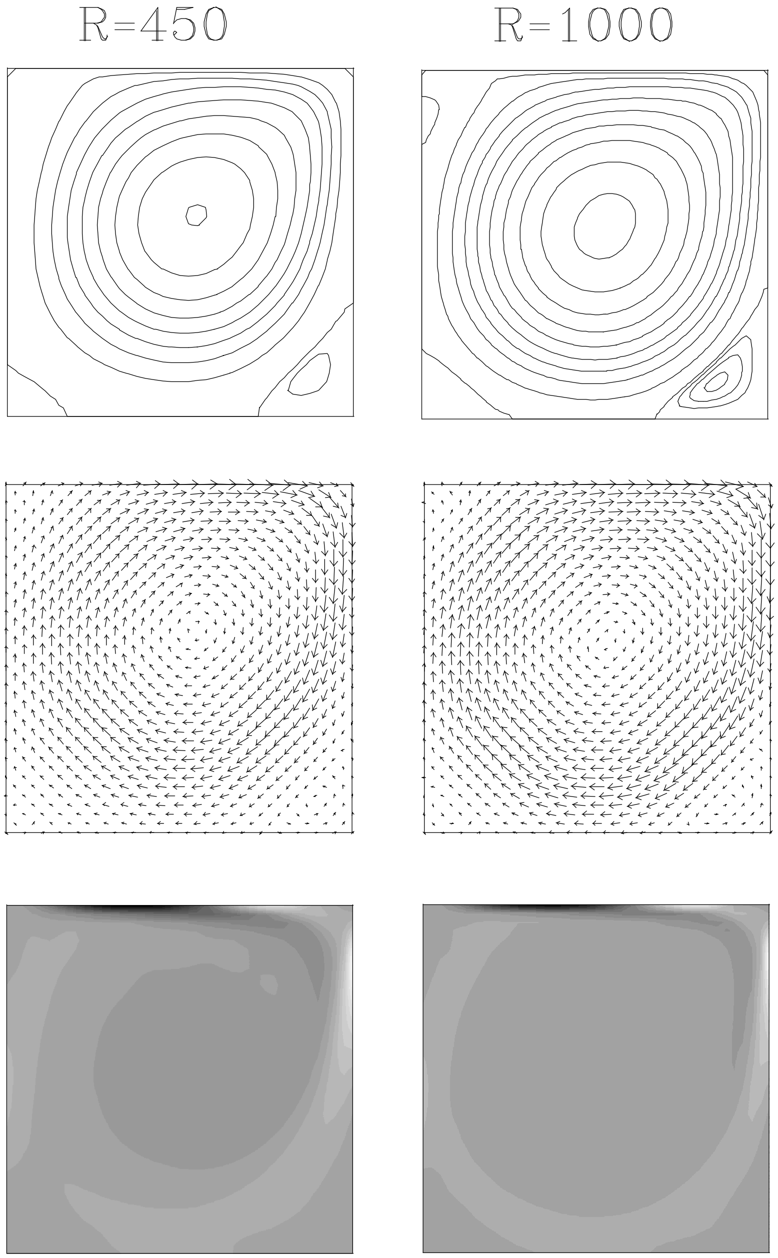

Figure 3.4: Above, featuring the stream lines for the specific values $R = 450$ and $R = 1000$. In the middle, the corresponding velocity vector fields. At the bottom, the vorticity distribution.

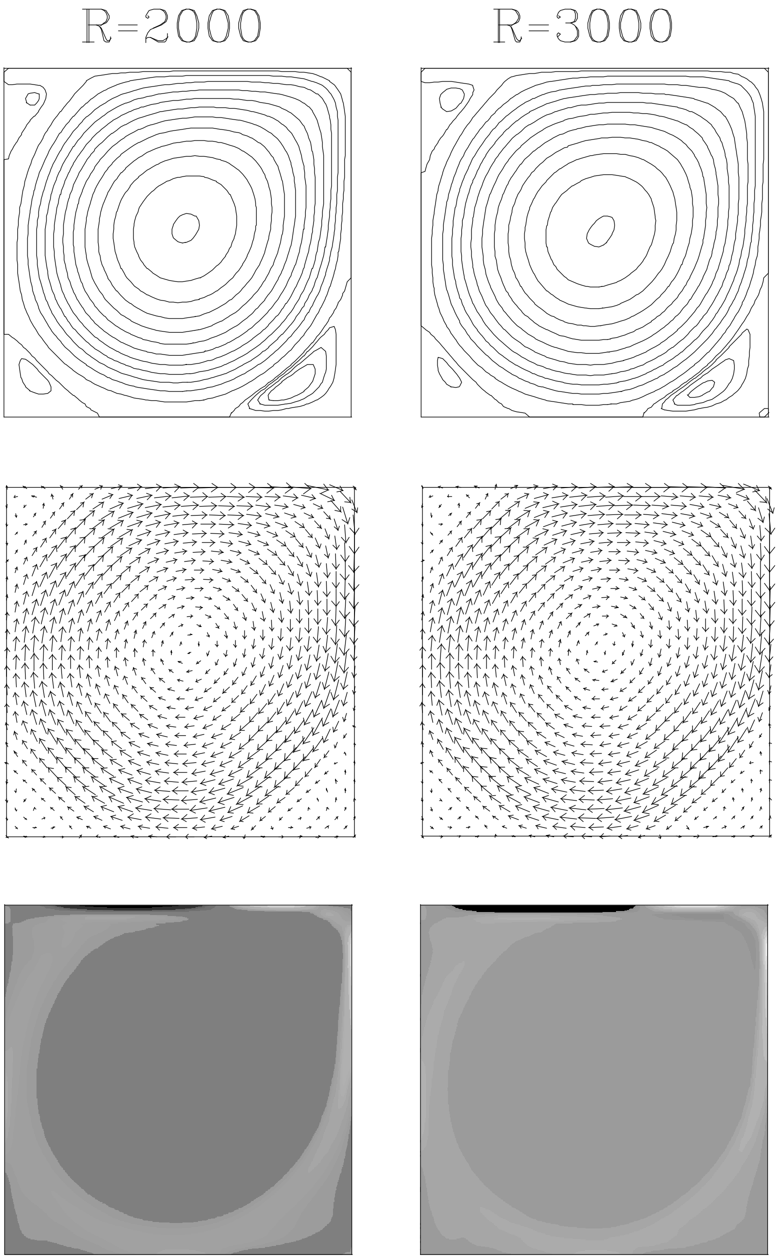

Figure 3.5: Above, featuring the stream lines for the specific values $R = 2000$ and $R = 3000$. In the middle, the corresponding velocity vector fields. At the bottom, the vorticity distribution.

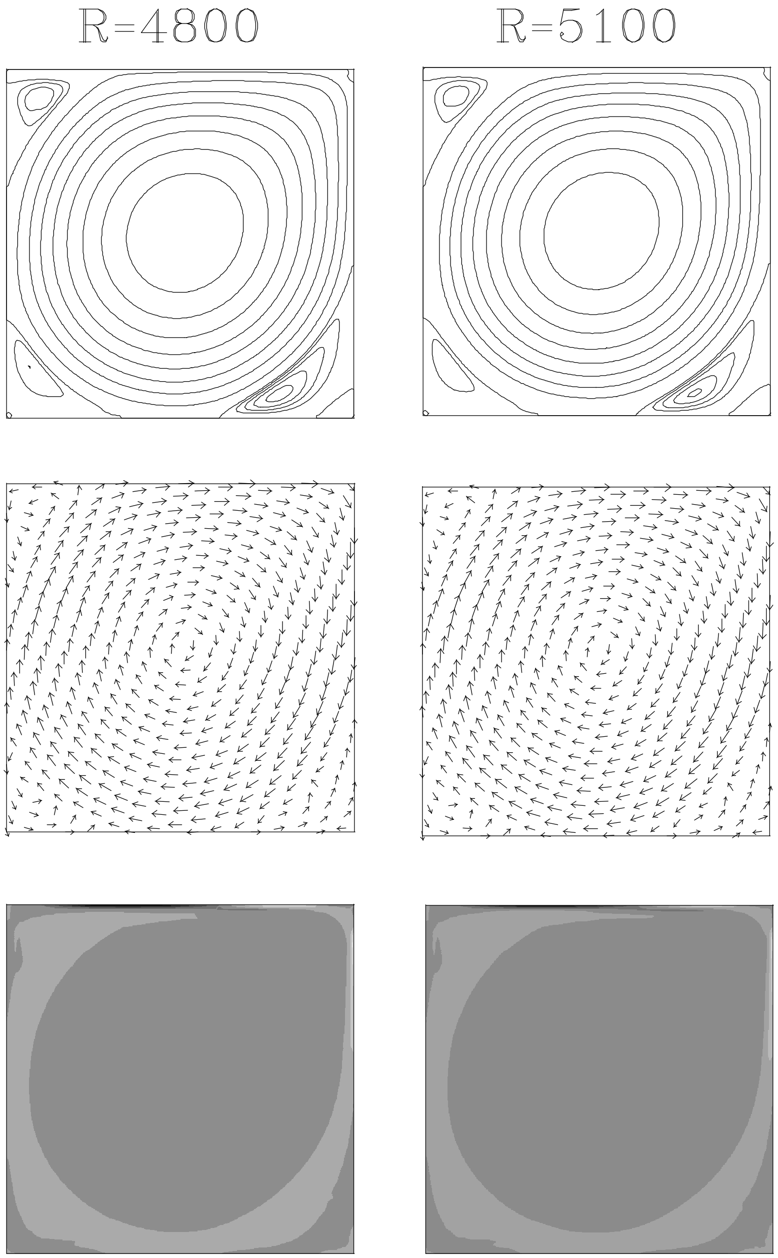

Figure 3.6: Above, featuring the stream lines for the specific values $R = 2000$ and $R = 3000$. In the middle, the corresponding velocity vector fields. At the bottom, the vorticity distribution.

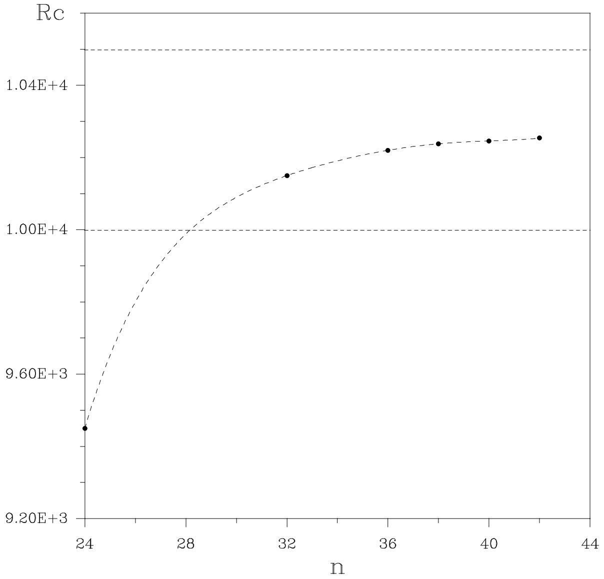

Figure 3.7: Critical Reynolds R_c number obtained as a function of the increasing number of spectral modes n. The two dotted horizontal lines represent the threshold limits of stability predicted by Shen. On note that our computations converge just in the middle of Shen's band (Shen, 1991).

The existence of a local branch of solution near the point (a_0, R_0) is ensured by the Implicit Function Theorem provided that f is analytic and J is non-singular in a neighborhood of that point (Keller, 1977). The presence of local bifurcations near $a = a_0$ depends on the evolution of eigenvalues of J in the complex plane. As a particular case, if one pair of complex conjugated eigenvalues cross the imaginary axis, then a Hopf bifurcation occurs. As a result, the flow loses its stationary structure and instabilizes to a time-periodic pattern whose periodicity is directly related to the imaginary part of λ_M.

For a wide range of values of the Reynolds number R, the spectrum of J has been computed. In figure 3.7, the computed critical Reynolds number as a function of the order of spectral approximation has been sketched. Numerical evidence predicts a Hopf bifurcation from the basic flow for $\mathrm{R}_c = 10250$. This result has been tested by increasing the number of modes of the spectral approximation. The numerical value of R_c is in the range of the interval predicted in (Shen, 1991), where time-evolution schemes were used to detect the instability. In Shen's analysis, two threshold limits of stability are given. They are depicted as dotted horizontal lines for the values $R = 1.00e4$ and $1.05e4$. Curiously, our computations converge just in the middle point of Shen's band. From a numerical point of view, a linear analysis of stability is much more accurate than a time-integration scheme in order to detect a Hopf bifurcation. In fact, these kind of high-dimensional dynamical systems may be very stiff, and time evolution methods may need very long transient periods of time to observe the instability.

Beyond the Hopf bifurcation, the present analysis is no longer valid. As a matter of fact, the continuation algorithm can only compute the evolution of steady solutions. On the contrary, Shen's temporal-evolution algorithms are capable of computing secondary time periodic patterns. In addition, it is possible to make a stability analysis of the time periodic flows as R is further increased. In fact, this is just what Shen's study does, detecting a secondary Hopf bifurcation in the range of values $[1.2e4, 1.25e4]$, where the flow loses its time periodicity, appearing another rational independent frequency (Ruelle-Takens scenario). It is supposed that further increase of the Reynolds number would lead to turbulent stages according with classical theories. In order to detect accurately the value of R for the secondary (Neimark-Sacker) Hopf bifurcation, it would be necessary to make a Floquet analysis on the periodic orbits in phase space representing the time-periodic flow. At present stage, this task is out of the scope of this work and it could be prohibitive from a computational cost point of view, due to the huge dimension of the associated dynamical system of amplitudes. Nevertheless, this kind of analysis is what is going to be done for a low dimensional model of the regularized driven cavity flow, where the dimension of the associated dynamical system is four.

Chapter 4

Feigenbaum's Universality in a Low Dimensional Fluid Model

4.1 Introduction

In this chapter, a low-dimensional truncated model for the Regularized Driven Cavity Flow is obtained by truncating a dynamical system of amplitudes for the velocity field. This low-dimensional model exhibits a route to chaos via a period doubling cascade (Feigenbaum's Scenario). In order to compute with high accuracy the period doubling, a numerical method based on the first order variational equations for the Poincaré map has been developed. This methodology can also be applied to the analysis of bifurcations of periodic orbits in low dimensional ordinary differential equations. This method allows to detect not only of the presence of bifurcations but also the computation of stable and unstable periodic orbits. In addition, the chaotic dynamics of the system is analyzed in detail by the computation of the Liapunov exponents for long-time integrations. For this purpose, a numerical scheme based on renormalization techniques has been constructed.

Low-dimensional analysis of fluid systems are of interest in capturing the essential features of their behaviour. Many fluid dynamics problems have been analyzed from this point of view (Lorenz, 1963, Boldrighini *et al.* , 1979). Of course, the results obtained from these models may not be directly related to experiment. However, they capture the basic qualitative features of the physical system. On the other hand, this kind of models usually provide relevant information about the core dynamics which governs the fluid motion.

In this chapter we introduce a low-dimensional analysis for the flow of a viscous fluid contained in a square box whose boundary conditions have been previously regularized (regularized driven cavity flow). As explained comprehensively in chapter 3, the regularization is needed for the analiticity of the solutions near the top boundaries. In this case, a spectral Legendre-tau scheme in primitive variables will be considered in order to obtain a dynamical system of amplitudes for the velocity field. By truncating the system up to order four, a relatively simple system of ordinary differential equations is obtained. Its analysis is the main subject of this chapter. We have found the stationary solution at low Reynolds number using a continuation method. This solution loses stability at a

Hopf bifurcation, and exhibits a cascade of period doubling bifurcations. Making use of a method based on the first order variational equations for the Poincaré map, the period doubling transitions have been computed with suitable accuracy. The methodology introduced here has a wide range of applicability in low dimensional ordinary differential equations. This method allows to detect the successive period doublings and to compute not only the stable periodic orbits but also the unstable ones.

For the truncated system, a period doubling scenario is obtained in the Reynolds number interval [503.26, 512.468]. This period doubling cascade verifies Feigenbaum's universality. Beyond $Re = 512.468$ the system presents chaotic behaviour. This is reflected in the Liapunov exponents analysis and in the Fourier spectra of the time evolution. Also, the structure of the Poincaré section of the attractor presents fractal features.

The chapter is organized as follows. In section 4.2, the physical description of the problem and the truncated four dimensional model are introduced. Besides, the steady solution is computed and monitorized as the Reynolds number is increased. Finally, the stability of the steady solution is studied. In section 4.3, the Newton-1^{st}-order variational method is developed in order to detect the period-doubling scenario in the model. The bifurcations are computed with high accuracy; the resulting cascade is presented in detail. Section 4.4 is devoted to the study of the chaotic zone. On the one hand, Liapunov exponents are computed as a function of the Reynolds number, showing the chaotic behaviour of the orbits. Moreover, periodic windows are obtained inside the chaotic region. On the other hand, the results of the Fourier spectra from time integrations of the dynamical system are presented for different regions of the parameter space. Finally, a Poincaré section of the strange attractor is visualized in order to analyze its self-similar (fractal) structure.

4.2 Physical Description: The Model

The problem consists of a two-dimensional square box of length L_0 filled with an incompressible fluid, whose velocity is given on one box side, and zero on the remaining ones, the so called cavity flow. The physical variables of the problem will be rendered dimensionless by considering $L_0/2$, $L_0/2\nu$ as the unit length and velocity respectively, being ν the kinematic viscosity. The fluid domain is $\Omega = [-1,1]\times[-1,1]$, in Cartesian coordinates (x, y). The boundary conditions are:

$$\vec{v}(\pm 1, y) = (0,0), \quad \vec{v}(x,-1) = (0,0), \quad \vec{v}(x,1) = \vec{v}_\Gamma = (R(x^2-1)^2, 0) \tag{4.1}$$

where R is the Reynolds number $R = L_0 v_0/2\nu$ and v_0 is the maximum of the imposed velocity on the side $y = 1$.

The problem will be approximated in a weak spectral-scheme. The velocity field belongs to a free-divergence function space. Therefore, the incompressibility condition is automatically satisfied. On the other hand, the Navier-Stokes equation is projected over a space of solenoidal functions which verify suitable boundary conditions in order to cancel the pressure term. The technical details of the method are explained in appendix B.

The low-dimensional truncation of Navier-Stokes equations with the boundary conditions described in the previous section yields a four-dimensional dynamical system for the amplitudes.

$$\begin{pmatrix}\dot{u}\\ \dot{v}\\ \dot{w}\\ \dot{z}\end{pmatrix} = R\begin{pmatrix}-\lambda_1\\ -\lambda_2\\ 0\\ 0\end{pmatrix} + R^2\begin{pmatrix}0\\ 0\\ -\lambda_3\\ -\lambda_4\end{pmatrix} - \begin{pmatrix}d_1 & 0 & 0 & 0\\ 0 & d_2 & 0 & 0\\ 0 & 0 & d_3 & 0\\ 0 & 0 & 0 & d_4\end{pmatrix}\begin{pmatrix}u\\ v\\ w\\ z\end{pmatrix} +$$

$$R\begin{pmatrix}0 & 0 & -\nu_1 & \nu_2\\ 0 & 0 & -\nu_3 & -\nu_4\\ -\delta_1 & \delta_2 & 0 & 0\\ \delta_3 & \delta_4 & 0 & 0\end{pmatrix}\begin{pmatrix}u\\ v\\ w\\ z\end{pmatrix} + \begin{pmatrix}\rho_1 uz - \rho_2 vw\\ \rho_3 uw - \rho_4 vz\\ \rho_5 wz - \rho_6 uv\\ \rho_7 u^2 + \rho_8 v^2 - \rho_9 w^2 - \rho_{10} z^2\end{pmatrix}, \quad (4.2)$$

where the coefficients are numerical constants, which can be found in appendix B.

The functional structure of (4.2) is too complicated to find analytical expressions for the stationary points and their dependence on the Reynolds number R. Nevertheless, the steady solution will be computed numerically, making use of a continuation method in the same way as in previous chapter (Keller, 1977). The solution branch is sketched in figure 4.1. The eigenvalues of the Jacobian matrix over the solution branch have been computed as a function of the parameter R. For values of R less than 321.5 the eigenvalues have negative real part. For $R = 321.5$ one pair of complex conjugated eigenvalues crosses the imaginary axis. As a result, a Hopf bifurcation appears. The orbit generated by this bifurcation is stable over the interval [321.5, 503.26].

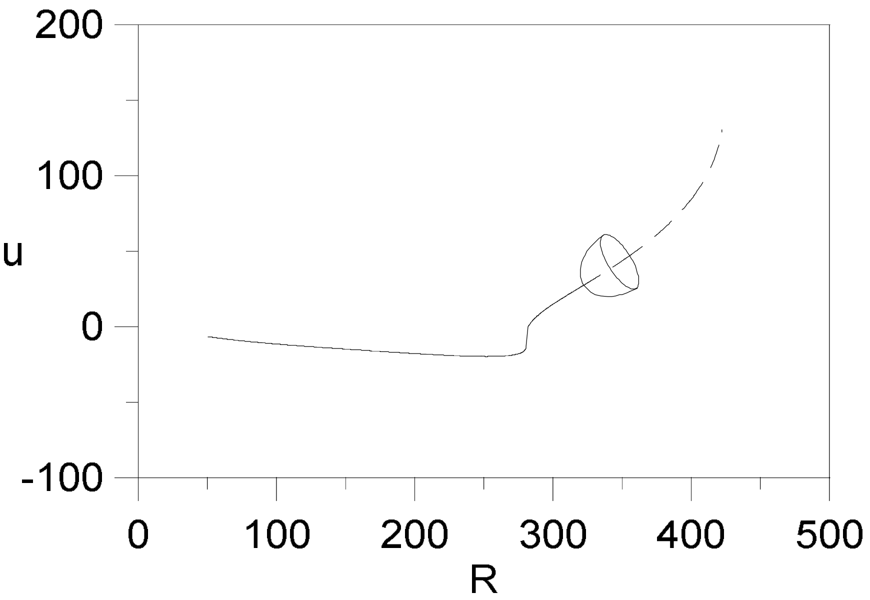

Figure 4.1: The fixed point as a function of the Reynolds number R. Solid line means stable, and dashed line, unstable. The parabolic shape that emerges from the continuous line represents the periodic orbit generated by the Hopf bifurcation.

4.3 Period Doubling Scenario: The Newton–1^{st}-Order-Variational Method

For the sake of simplicity, the system (4.2) will be symbolically expressed as $\dot{x} = f(x, R)$. Let $\phi(t, x)$ be the solution of this system with x as initial condition ($\phi(0, x) = x$). In order to fix the stability and secondary bifurcations of the periodic orbit γ that appears in the Hopf bifurcation, the associated Poincaré map has been considered. Let Π_0 be a hyperplane transversal to γ in a point $x_0 \in \gamma$. The equation of Π_0 is $(x - x_0) \cdot \xi = 0$, where ξ satisfies the transversality condition $\xi \cdot f(x_0, R) \neq 0$. Therefore, the Poincaré map is given by

$$\begin{array}{rccl} P: & \Pi_0 & \longrightarrow & \Pi_0 \\ & x & \longrightarrow & P(x) = \phi(\tau(x), x) \end{array} \tag{4.3}$$

where the function $\tau(x)$, the time of flight needed to return to Π_0, is obtained from the equation $(\phi(\tau(x), x) - x_0) \cdot \xi = 0$. The eigenvalues of DP lead the stability of the periodic orbit γ. Formally, DP is the restriction to Π_0 of the solution of the first variational equation

$$\dot{J} = D_x f(\phi(t, x_0), R) J \quad , \quad J(0) = \mathbf{1}_4 \tag{4.4}$$

where $\mathbf{1}_4$ is the identity matrix in $\mathbb{R}^4$. The projection on Π_0 is given by

$$DP = (\mathbf{1}_4 - \frac{f(x_0, R) \otimes \xi}{f(x_0, R) \cdot \xi}) J \mid_{\Pi_0}, \tag{4.5}$$

where DP is a $3-$dimensional square matrix.

The method we have termed Newton–1^{st}-order-variational is an algorithmic process which allows to compute simultaneously the periodic orbit, its period and the differential of the corresponding Poincaré map (for a detailed explanation of the numerical algorithms used here, see appendix C). From an initial point x^k near to γ and an estimate T^k of the period, the following system is integrated in time

$$\left\{ \begin{array}{rcl} \dot{x} = f(x, R) & , & x(0) = x^k \\ \dot{J} = [D_x f(x, R)] J & , & J(0) = \mathbf{1}_4 \end{array} \right. \tag{4.6}$$

Next, the accuracy of the period is improved by integrating the dynamical system (4.6) up to a final time $t = T^{k+1}$ which satisfies the cut condition with the Poincaré section:

$$(\phi(T^{k+1}, x^k) - x^k) \cdot \xi = 0 \tag{4.7}$$

This time can be obtained iteratively by linear interpolation or the bisection method. As a result, a final predictor point $x^{k+1/2}$, the Jacobian matrix and DP evaluated at T^{k+1} are computed:

$$\begin{array}{l} x^{k+1/2} = \phi(T^{k+1}, x^k), \quad J^{k+1} = J(T^{k+1}) \\ DP^{k+1} = (\mathbf{1}_4 - \dfrac{f(x^k; R) \otimes \xi}{f(x^k; R)} \cdot \xi) J^{k+1} \mid_{\Pi_k} \end{array} \tag{4.8}$$

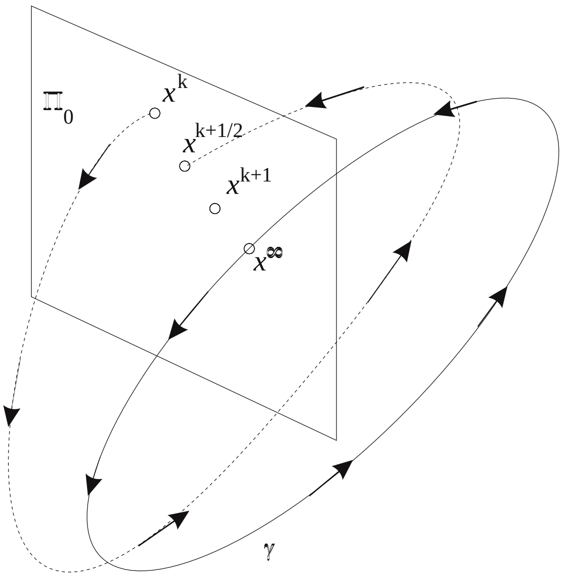

Figure 4.2: Featuring algorithmic process of computation of periodic orbits as fixed points of the Poincaré map.

Finally, the predicted values are slightly modified making use of a corrector Newton process over Π_k (see figure 4.2):

$$x^{k+1} = x^k + (\mathbf{1}_3 - DP^{k+1})^{-1}(x^{k+1/2} - x^k) \tag{4.9}$$

The matrix $\mathbf{1}_3 - DP^{k+1}$ must be invertible, i.e., its eigenvalues must be different from 1. But when γ is stable, the eigenvalues have moduli less than 1, and the computed bifurcations are associated to period doublings. The critical eigenvalue crosses the unit circle by -1 and the matrix of the Newton method is invertible. For $k \to \infty$, x^k gives a point of the orbit, regardless of whether it is stable or not. T^k and DP gives its period and eigenvalues.

This iterative process is the core of a continuation method in the Reynolds number R. The process starts with a R value at which γ is stable. The first periodic orbit is obtained by time evolution of (4.2). For a new value of R the iteration begins with a point and the period of the previous orbit; if the orbit suffers a period doubling bifurcation, the new guiding period will be twice the former period.

In order to simplify the computations, the vector ξ and the coordinates for Π_0 are held fixed throughout the global process. The transversality to γ is ensured by moving x_0 along the orbit to a point p_γ where the angle between the orbit and the Poincaré section is maximum:

$$\frac{f(x,R)\cdot\xi}{\|f(x,R)\|\|\xi\|} \leq \frac{f(p_\gamma,R)\cdot\xi}{\|f(p_\gamma;R)\|\|\xi\|} \quad \forall x \in \gamma \tag{4.10}$$

By gradually varying the Reynolds number R, the bifurcating values of R can be computed with high degree of accuracy (by successive linear interpolation, for example).

R_{crit}	δ
R^1=503.26263580	
R^2=507.98889404	δ^1=1.113
R^3=512.23403718	δ^2=23.361
R^4=512.41575610	δ^3=4.3590
R^5=512.45743770	δ^4=5.0208
R^6=512.4657403824	δ^5=4.6436
R^7=512.4675281125	δ^6=4.6773
R^8=512.4679103180	δ^7=4.6689
R^9=512.4679921795	

Table 4.1: Critical Reynolds numbers R^n and ratios δ^n for the period doubling cascade.

As a result, a period doubling cascade has been detected, whose first nine period doubling bifurcation values has been detailed in Table 4.1. The table also shows the ratios between the successive bifurcation intervals, defined by:

$$\delta^n = \frac{R^{n+1} - R^n}{R^{n+2} - R^{n+1}} \tag{4.11}$$

It can be observed that these ratios approach Feigenbaum's universal constant $\delta_F = 4.66920160\ldots$. The R^n sequence has an accumulation point at $R^\infty = 512.468014489$.

The first one, two, four and eight periodic states are sketched in figure 4.3, where we have represented the amplitude z versus the amplitude v.

4.4 Properties of the Strange Attractor

Liapunov exponents provides information about the stability of the orbits and the long-term behaviour of the volume elements in phase space (i.e., contraction and expansion). For the present problem, the first order variational dynamical system has been considered again

$$\begin{array}{lcl} \dot{x} = f(x,R) & , & x(0) = x_0 \\ \dot{J} = [D_x f(x,R)]J & , & J(0) = \mathbf{1}_4 \end{array} \tag{4.12}$$

where now x_0 is a point of the orbit or the attractor to be considered, obtained after a suitable transient time integration. Making use of the previous system, the eigenvalues μ_j of the matrix J can be computed for all values of t. Therefore, the Liapunov exponents of the dynamical system will be:

$$\lambda_j = \lim_{T\to\infty} \frac{\log \mid \mu_j \mid}{T} \qquad (j = 1,2,3,4) \tag{4.13}$$

When the Liapunov exponents are evaluated directly by integrating the first variational equations (4.12), numerical problems arise. The columns of $J(t)$ become almost parallel to the direction of the biggest Liapunov exponent, J becomes ill conditioned, and tends

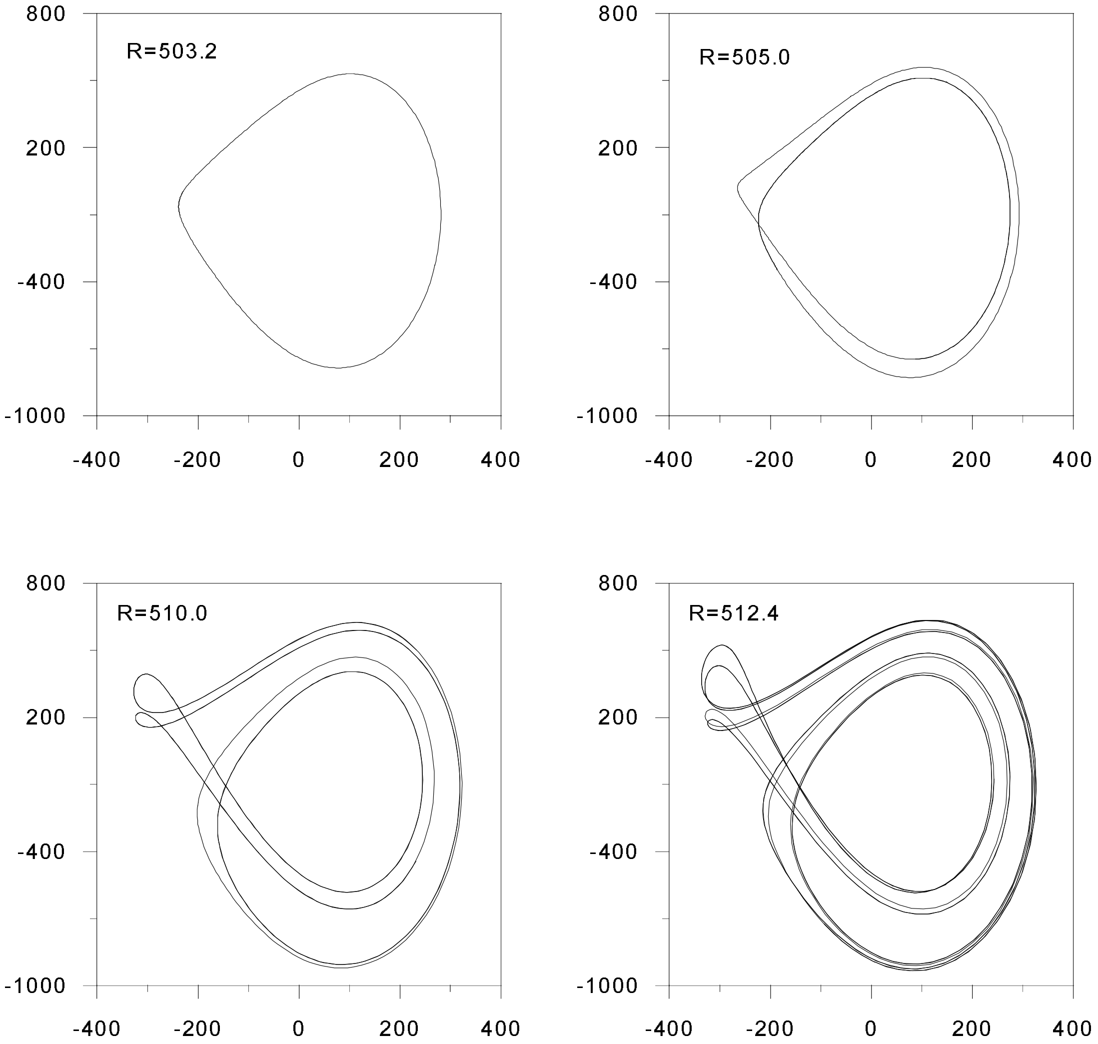

Figure 4.3: Orbits of the one, two, four and eight periodic states. In the figures the x axis corresponds to the v amplitude and the y axis to the z amplitude.

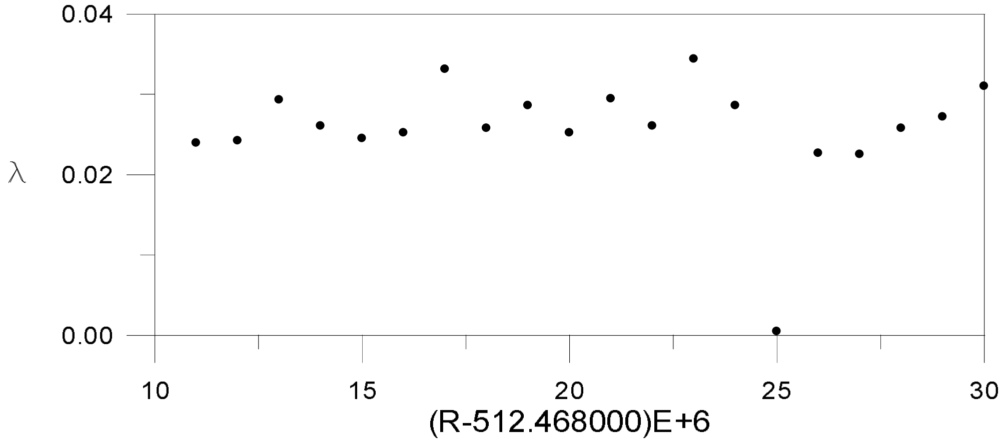

Figure 4.4: Maximum Liapunov exponent as a function of the Reynolds number R. Note the periodic solution at $R = 512.468025$

to be singular. Furthermore, if some of the Liapunov exponents are greater than zero, overflow problems can occur. Therefore, the previous limit cannot be computed directly. In order to handle this problem, the renormalization method of Shimada and Nagashima (Shimada & Nagashima, 1979) has been used. The previous method is comprehensively described in (Kubicek & Marek, 1983) although a comprehensive explanation can be found in appendix C. Finally, the Liapunov exponents have been computed as a function of the Reynolds number. For the periodic solutions ($R \leq R^{\infty}$) the maximum exponent is zero, being negative the remaining ones, as it was expected. The behaviour of the greatest Liapunov exponent for $R > R^{\infty}$ is displayed in Fig. 4.4. Positive values of the exponent correspond to chaotic solutions, and it can be observed that the system is chaotic but presents a window with a periodic stable solution. This behaviour is typical of many dynamical systems which exhibit a period doubling cascade. Besides, it should be regarded here that the system is featured by a strong hysteresis. As a consequence, different initial conditions can lead to different solutions, multi-periodic solutions or chaotic ones.

The strange attractor corresponding to the chaotic zone ($R = 512.5$) is sketched in figure 4.5. In order to analyse the fractal features of the strange attractor, a Poincaré section has been obtained. This section is depicted in Fig. 4.6 for $R = 512.5$. Its self-similarity structure, typical of strange attractors is apparent. The fractal dimension of the attractor has been computed using the numerical method of Grassberger and Procaccia (Grassberger & Procaccia, 1983) [1]. The computed dimension for $R = 512.5$ is $d = 1.5854$

The Fourier spectra for two different Reynolds numbers are shown in Fig. 4.7. The first spectrum corresponds to a periodic orbit, and the second one is in the chaotic region. On note that the former exhibits a broad-band noise, whose level is two or more orders of magnitude higher than in the periodic case. This is a typical signature of chaos. In the chaotic spectrum sharp peaks appear above the level of the noise. Similar types of spectrum have been observed by other authors (Kubicek & Marek, 1983). This type

---

[1] Dr. Crespo is thanked for his help in computing the fractal dimension of the attractor

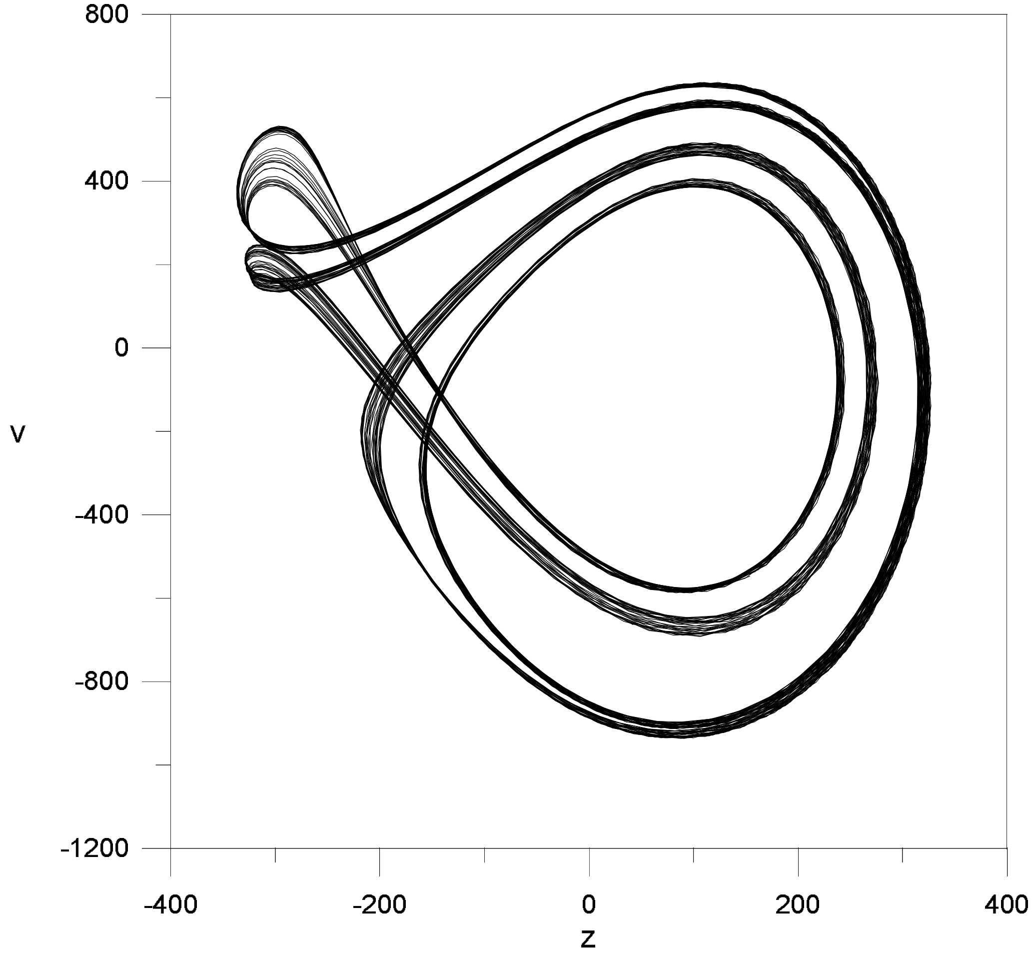

Figure 4.5: Plot of the strange attractor for $R = 512.5$. Projection into the plane (v,z).

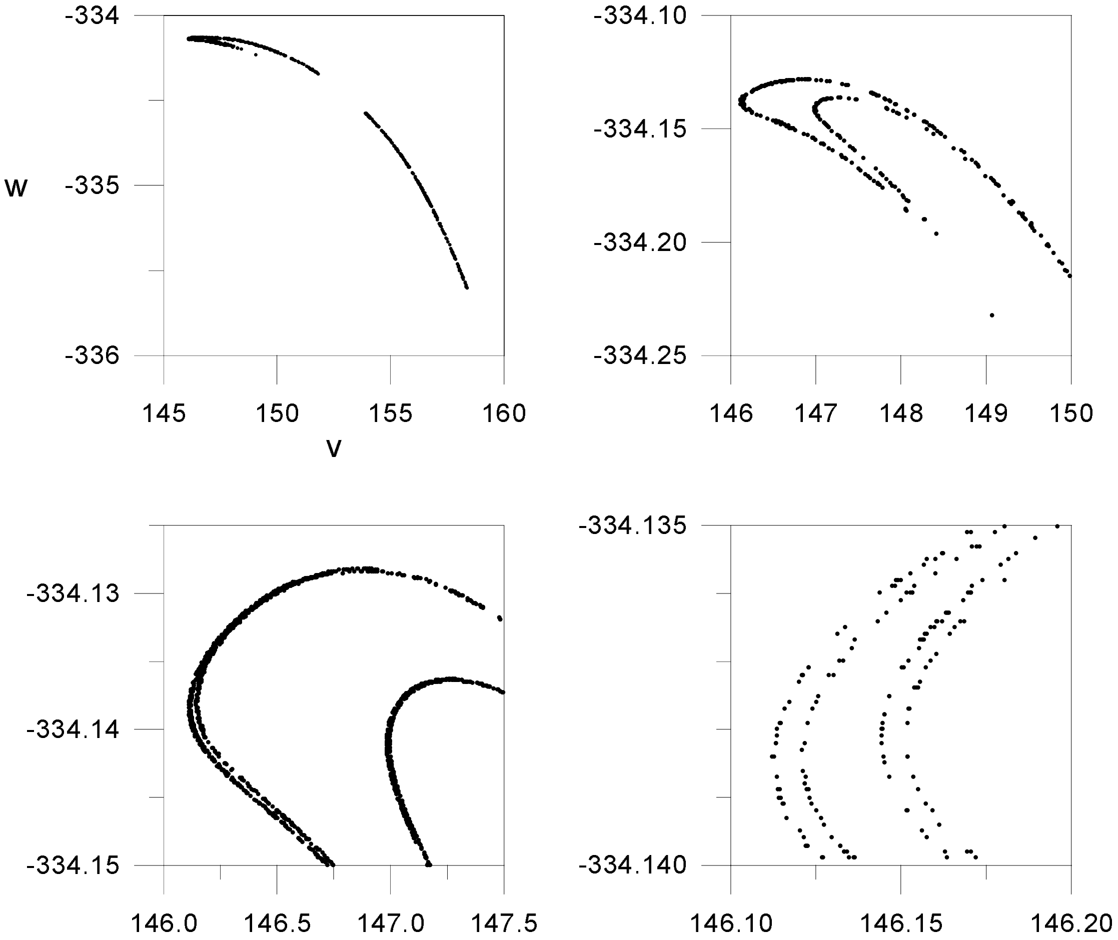

Figure 4.6: Poincaré section of the strange attractor for $R = 512.5$. The enhanced areas show a self-similar structure. The variables displayed are (v, w)

of spectrum is usually termed *phase coherent*, and occurs close to unstable limit cycles generated by the sequence of period doubling bifurcations.

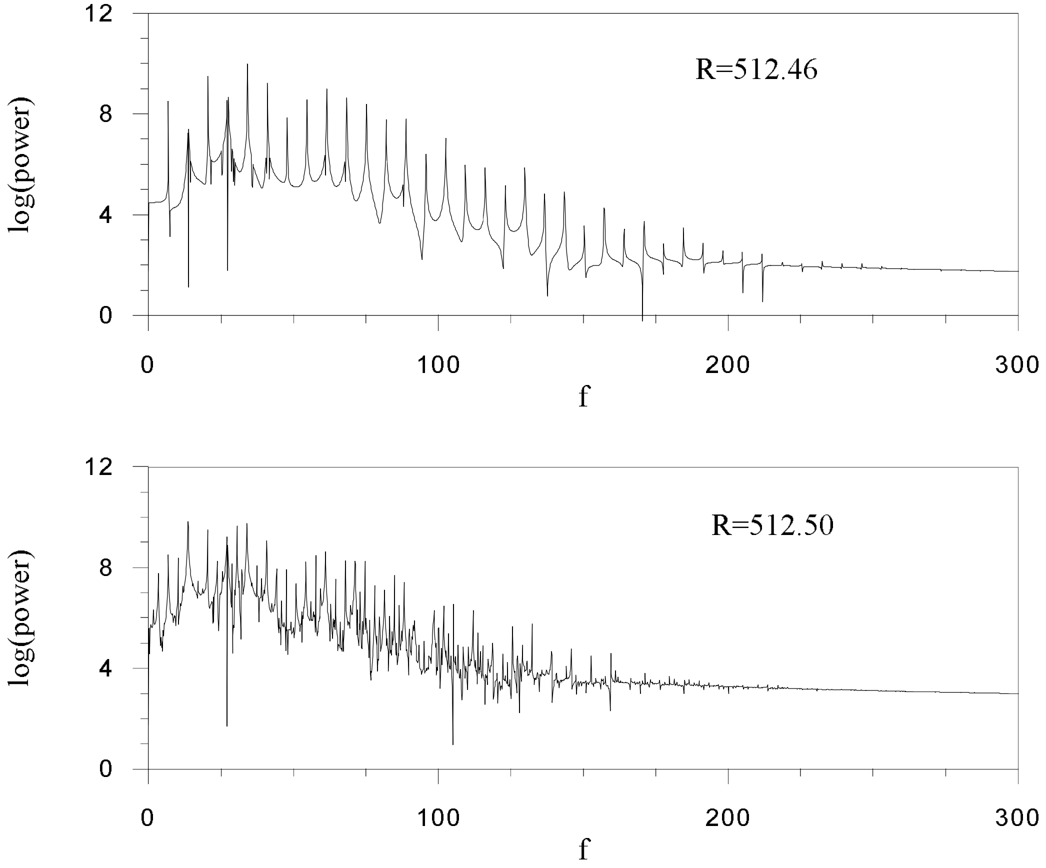

Figure 4.7: Fourier spectra for a periodic solution ($R = 512.46$) and a chaotic solution ($R = 512.50$).

A further increase of the Reynolds number produces a collapse between the chaotic attractor and an unstable manifold belonging to another branch of steady solutions. This collision produces an eventual inestabilization of the attractor. This phenomenon is probably due to the excessive truncation of the model.

In order to check the behaviour of this low-dimensional model, six-dimensional system for the same problem ($M = 2$ and $N = 3$) has been computed. The obtained results are very similar. The six-dimensional model also exhibits a period doubling scenario, although the bifurcations take place at different Reynolds numbers.

4.5 Conclusions

By analyzing a truncated model for a two dimensional Navier-Stokes problem we find a transition to chaos by means of a period doubling cascade. The period doubling verifies

Feigenbaum's universality. After the successive period doubling bifurcations, the system presents a chaotic behaviour. This is reflected in the Liapunov exponents and in the Fourier spectra of the time integrations of the dynamical system. A six-dimensional model has also been studied in order to check the results obtained with the four-dimensional one. In both cases, the qualitative phenomena are essentially the same. We have also introduced a useful methodology for the analysis of the bifurcations of periodic orbits in low dimensional ordinary differential equations, that we have termed the Newton-1^{st}-order-variational method.

Chapter 5

Axial Effects in the Taylor-Couette Problem

5.1 Introduction: The Taylor-Couette Problem

The Taylor-Couette problem concerns with the behaviour of a viscous fluid contained between two concentric cylinders which rotate independently around their common axis. The physical system was originally designed by Couette and Mallock in 1888 Couette, 1888, Mallock, 1888 in order to apply it in viscosimetric measures of fluids. In fact, it was Margules who, in 1881, proposed the construction of a viscosimeter which could measure the angular momentum response of an internal cylinder in contact with a viscous fluid rotating under the action of an external cylinder. Although the theory developed by Couette predicted that this response should be linear, the experiments only behaved correctly for a low range of outer rotation angular velocities. Beyond a threshold limit of the angular speed of the external cylinder, the response was much more complicated, with the appearence of turbulent stages. In a different way, Mallock considered the inverse problem by increasing the angular velocity of the inner cylinder and studying the behaviour of the external one. Again, the observed phenomena did not completely coincide with the theoretical predictions of Couette. In fact, for a threshold limit of the inner rotation speed, the response of the speed of the outer cylinder was also linear but with greater slope. A partial explanation to this phenomenon was proposed by Lord Rayleigh in 1916. For this purpose, Rayleigh considered perturbations of concentric fluid rings. These perturbations were submitted to angular momentum conservation. As a result, the sufficient condition of instability was the decreasing rate of the angular momentum of the fluid ring with respect to the radial variable. In fact, the Rayleigh criterion of instability was a inviscid condition and the dumping effects due to viscosity were not considered.

A comprehensive explanation of the instability mechanism was introduced by G.I. Taylor, who in a brilliant theoretical and experimental work, predicted the instability of the azimuthal flow proposed initially by Couette (Taylor, 1923). In the previous work, the instability values of the inner rotation velocity were computed for different external rotation conditions. In addition, the secondary patterns, which appear immediately after the bifurcation from the Couette flow, were predicted linearly and checked experimentally.

These new toroidal structures are now termed Taylor Vortex flow. Actually, the new geometry of the flow allows a better efficiency in the radial transport of the angular momentum throughout the fluid system. In any case, it should be mentioned that, the prediction of this kind of patterns is due to Stokes who, in 1848, had already proposed the existence of cellular structures for high rotation speeds of the inner cylinder.

Flow between rotating cylinders is remarkable for the fact that slow increase of the speed of the inner cylinder gives rise to a wide spectrum of well-distinguishable flow patterns of increasing geometrical complexity. In Andereck *et al.* , 1986, a comprehensive experimental study of different flows which appear in different parts of parameters space can be found. Moreover, the flows which appear in Taylor-Couette problem depend strongly on the particular path followed to reach each of the points in parameter space. This hysteresis phenomena occurs frequently in non-linear physical systems. Altogether, Taylor-Couette problem turns out to be a perfect framework with which, the main theoretical predictions about pre-turbulent stages can be checked.

The present chapter will deal with the Taylor-Couette stability analysis in a more general way. In addition to the centrifugal effects produced by the rotation of the cylinders, shear axial effects will be considered. This effect will be accomplished by an inertial relative sliding between the cylinders. The global system is now termed Spiral Couette problem and it has been studied partially by many authors from the sixties on (Ludwieg, 1964, Hung, Joseph & Munson, 1972, Ali & Weidman, 1993). Nevertheless, so far the studies dealing with the problem have been a bit restricted to particular situations. As a matter of fact, the problem is now a bit more complicated, not only because of the presence of a new physical parameter, but also because of the competition between two different kinds of instability effects, that is, shear and centrifugal mechanisms. It is a well known fact that shear flow in a pipe throughout its axial direction is linearly stable with respect to infinitesimal perturbations. Likewise, the solid-body rotation where both cylinders rotate at the same angular speed, is linearly stable. A very interesting physical phenomenon occurs when a slight shear effects inestabilizes the solid-body rotations problem and, simultaneously, a little relative rotation inestabilizes the pure shear axial flow (Mackrodt, 1976).

Very extensive literature has reported on the behaviour of Taylor-Couette problem under different physical conditions. A comprehensive historical review of the subject would require hundred of pages and its is out of the scope of the present research. A very good synthesis of the whole inestabilization mechanisms of the problem can be found in Chossat & Iooss, 1994. For a comprehensive experimental study of the different flows which appear see Andereck *et al.* , 1986. The present work needs to be restricted to make specific references to those points which are going to be studied. Nevertheless, it is worthwile to devote a section to the classical Taylor–Couette problem in order to have a broader view.

5.1.1 The Taylor-Couette Problem: Physical Description

Taylor–Couette flow is the term used to describe fluid motion between two concentric rotating cylinders, whose radius and angular velocities are r_i^*, r_o^* and Ω_i, Ω_o respectively. The annular gap between the cylinders is $d = r_o^* - r_i^*$.

The independent nondimensional parameters appearing in this problem are, the radius

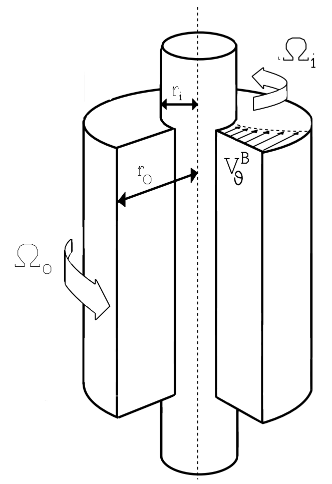

Figure 5.1: Geometric sketch and parameters of the Taylor-Couette problem. The basic flow v_θ^B, driven by the angular rotations Ω_i, Ω_o, is also depicted.

ratio $\eta = r_i^*/r_o^*$, which fix the geometry of the annulus and the Couette flow Reynolds numbers $R_i = dr_i\Omega_i/\nu$ and $R_o = dr_o\Omega_o/\nu$ of the rotating cylinders.

Henceforth, all variables will be rendered dimensionless using d, d^2/ν, ν^2/d^2 as units for space, time and the reduced pressure (p^*/ρ^*). The Navier–Stokes equation and the incompressibility condition for this scaling become

$$\partial_t \mathbf{v} + (\mathbf{v}\cdot\nabla)\mathbf{v} = -\nabla p + \Delta\mathbf{v}, \quad \nabla\cdot\mathbf{v} = 0, \tag{5.1}$$

which can be expressed explicitly in a suitable cylindrical coordinate system (r, θ, z) as follows:

$$\begin{aligned}
\partial_t u + u\partial_r u + \frac{v}{r}\partial_\theta u + w\partial_z u - \frac{v^2}{r} &= -\partial_r p + \Delta u - \frac{2}{r^2}\partial_\theta v - \frac{u}{r^2} && (5.2)\\
\partial_t v + u\partial_r v + \frac{v}{r}\partial_\theta v + w\partial_z v + \frac{uv}{r} &= -\frac{1}{r}\partial_\theta p + \Delta v + \frac{2}{r^2}\partial_\theta u - \frac{v}{r^2} && (5.3)\\
\partial_t w + u\partial_r w + \frac{v}{r}\partial_\theta w + w\partial_z w &= -\partial_z p + \Delta w && (5.4)\\
\partial_r u + \frac{1}{r}\partial_\theta v + \partial_z w + \frac{u}{r} &= 0, && (5.5)
\end{aligned}$$

where u, v and w are the radial, azimuthal and axial components of the velocity vector field $\mathbf{v}$, respectively. In previous equations, Δ stands for the laplacian operator in cylindrical coordinates

$$\Delta = \partial_r^2 + \frac{1}{r}\partial_r + \frac{1}{r^2}\partial_\theta^2 + \partial_z^2 \tag{5.6}$$

5.1.2 Steady Solutions and Symmetry Analysis

The first difficulty that arises when properly describing the physical system lies in the boundary conditions which must be imposed on the top and bottom sides of the cylinder. From an experimental point of view, those conditions may be chosen in different ways. In fact, the top and bottom lids may be enforced to rotate with one of the two cylinders or to remain fixed. Another possibility is to remove the top wall. In this situation, the top part of the fluid is submitted under a stress free boundary condition. The anomalous effects produced by different configurations has been studied by many authors (Cliffe *et al.* , 1992). It is a remarkable fact that comparisons between experiments and predictions from theoretical arguments (neglecting lids effects) are reasonably good, provided that the height of cylinders is large enough compared to the gap width, even in such situations where complicated dynamics occur close to the points of onset of instability for Couette flow. Moreover, those effects appear after long transient periods of time only. From a numerical point of view, a realistic computation of the solutions of the Navier–Stokes problem may be very complicated. Furthermore, in the absence of symmetries, the previous numerical integrations would not provide the main features of the bifurcated solutions.

The apparent experimental evidence of the presence of axial periodicity in the bifurcated patterns of the physical system, is a fair motive for imposing the usually termed *infinite cylinder* hypothesis. This last hypothesis allows to obtain an analytical solution for the problem, which is essential for the study of the stability and bifurcations, used throughout this research. The identification of the top and bottom sides changes the topology of the problem, becoming now a two dimensional torus in the axial and azimuthal coordinates. The invariance group of transformations is properly $\mathsf{O(2)}\times\mathsf{SO(2)}$. On the one hand, the orthogonal group $\mathsf{O(2)}$ is associated with the translations in the axial directions identified with vertical periodicity modulus and with specular reflections with respect a horizontal plane containing the origin. On the other hand, $\mathsf{SO(2)}$ is associated with the rotations around the common axis of the cylinders. To sum up, the corresponding actions on the velocity field given by equations (5.2), (5.3), (5.4) and (5.5) are

$$(\tau_a\mathbf{v})(r,\theta,z) = (u,v,w)(r,\theta,z+a), \quad a\in\mathbb{R} \tag{5.7}$$

$$(S\mathbf{v})(r,\theta,z) = (u,v,-w)(r,\theta,-z) \tag{5.8}$$

$$(R_\psi\mathbf{v})(r,\theta,z) = (u,v,w)(r,\theta+\psi,z), \quad \psi\in\mathbb{R}/2\pi\mathrm{Z} \tag{5.9}$$

The next step is the computation of steady solution for the system (5.2), (5.3), (5.4) and (5.5). Assuming zero axial-radial components on the sought solution and invariance under the prescribed transformations (5.7), (5.8) and (5.9), an exact solution is found. For this purpose, the following boundary conditions on the velocity vector field must be imposed:

$$u(r_i)=0, \quad u(r_o)=0, \tag{5.10}$$

$$v(r_i)=R_i, \quad v(r_o)=R_o, \tag{5.11}$$

$$w(r_i)=0, \quad w(r_o)=0, \tag{5.12}$$

where $r_i = \eta/(1-\eta)$, $r_o = 1/(1-\eta)$. As a result, the sought solution, also termed

Couette-Flow, is given by the following components

$$u_B = 0,\ v_B = Ar + \frac{B}{r},\ w_B = 0 \tag{5.13}$$

as can be seen in (Joseph, 1976). The constants A and B are given by

$$A = \frac{R_o - \eta R_i}{1-\eta^2},\ B = \frac{\eta(R_i - \eta R_o)}{(1-\eta)(1-\eta^2)}. \tag{5.14}$$

As a result, the exact solution is a pure azimuthal flow, where the fluid particles are rotating in circular trajectories around the vertical axis and constrained to parallel horizontal planes. On note that the transformations defined in relations (5.7), (5.8) and (5.9), act trivially over the basic flow (5.13):

$$\tau_a \mathbf{u}_B = \mathbf{u}_B \quad S\mathbf{u}_B = \mathbf{u}_B \quad R_\psi \mathbf{u}_B = \mathbf{u}_B \tag{5.15}$$

5.1.3 Linear Stability Analysis: Main Results

As already has been briefly commented, the Taylor–Couette problem has been extensively studied by many authors in its different possible configurations. In this section, the main results concerning the stability of the centrifugal mechanism will be introduced. In fact, the computations which are going to be presented here have been done in order to be compared and checked with previous works and to make a numerical test of the Petrov-Galerkin schemes used. This section will focus its attention on the final results more than on the methodology used to obtain them. A comprehensive explanation of the computational methods will be more properly introduced in the general case concerning axial effects.

During these last decades, the increasing numerical capabilities of computational devices has allowed to provide more accurate integration schemes for the Navier-Stokes equations. This fact has directly affected to the study of the Taylor-Couette problem, increasing exponentially the knowledge about its behaviour under specific conditions. A synthesis of the results would be prohibitive for the present purposes, but it is worthwile to present here the essential features exhibited by the problem. At this stage, the first step is to recover the basic results concerning the stability of *Couette flow.* As commented in the introduction, the first comprehensive analysis was carried out by G.I. Taylor in 1923. Nevertheless, it would be unfair to forget the first non-viscous criterion of stability stated by Lord Rayleigh in 1916. *Rayleigh's criterion* of stability considers small perturbations of the orbit of a fluid ring, which is rotating with constant angular velocity around a fixed axis which contains the center of the ring and is parallel to the angular velocity vector. Under the hypothesis of conservation of angular momentum of the perturbed ring, it can be demonstrated (Landau & Lifshitz, 1987) that the local angular momentum of the fluid must increase with respect to the distance to the rotation axis in order to be stable. This general condition for rotating fluids can be particularly applied on *Couette flow* for the co-rotation case. As a result, the non-viscous condition of stability is $R_o > \eta R_i$. On the other hand, Taylor considered the problem of stability as a boundary value problem in which an infinitesimal perturbation (Lin, 1955), vanishing on the radial boundaries r_i and

r_o, disturbs the velocity and pressure fields. From a formal point of view, stability of a basic flow means stability with respect to all possible infinitesimal disturbances. Accordingly, for an investigation on stability to be complete, it is necessary that the reaction of the system to all possible disturbances be examined. In practice, this is accomplished by expressing an arbitrary disturbance as a superposition of certain basic possible periodic [1] modes and examining the stability of the system with respect to each of these modes (*normal mode analysis*), as noted in chapter one. The mathematical formulation of the problem may be established by considering the perturbed fields from the basic state

$$\mathbf{v}(r,\theta,z,t) = \mathbf{v}_B(r) + \mathrm{e}^{\mathrm{i}(n\theta+kz)+\lambda t}\mathbf{u}(r), \tag{5.16}$$

$$p(r,\theta,z,t) = p_B(r,z) + p'(r)\mathrm{e}^{\mathrm{i}(n\theta+kz)+\lambda t}, \tag{5.17}$$

where $k \in \mathbb{R}$, $n \in \mathrm{Z}$ and $\lambda \in \mathbb{C}$. Thus, k features the possible continuous periodicity in the axial $z-$coordinate, n is the azimuthal normal mode (which must be integer due to the azimuthal symmetry), and $\lambda = \sigma + \mathrm{i}\omega$ leads the stability of the flow, as explained in chapter one. Similarly, $\mathbf{v}_B = (0, v_B, w_B)$ is given by (5.13) and the boundary conditions for $\mathbf{u}$ are homogeneous, $\mathbf{u}(r_i) = \mathbf{u}(r_o) = \mathbf{0}$. Linearizing the Navier–Stokes equations about the basic solution, the following eigenvalue problem is obtained

$$\lambda\mathbf{u} = -\nabla p' + \Delta\mathbf{u} - \mathbf{v}_B\cdot\nabla\mathbf{u} - \mathbf{u}\cdot\nabla\mathbf{v}_B. \tag{5.18}$$

Formal substitution of perturbed fields (5.17) in equation (5.18) leads to a decoupled system of eigenvalues for each mode n and k. Thus, a comprehensive study of the stability is accomplished by the computation of the spectrum of eigenvalues $\lambda(n,k)$ for each problem and, eventually, the selection of the critical ones (i. e., those which have maximum real part). A graphical representation of the global procedure of stability analysis is depicted in figure 5.2, for $R_o = 0$. In this case, for a fixed wavenumber k, the inner Reynolds number R_i is progressively increased up to a critical value $R_i^c(k)$ so that one of the eigenvalues crosses the imaginary axis (i. e., $\sigma = 0$). This procedure must be done for a wide continuous range of values of k and for the different azimuthal wavenumbers n. Typically, for a fixed value of n, the curve of critical $R_i^c(k)$ values has a parabolic profile with a single and well-distinguished minimum. The curves $\sigma(k, R_i) = 0$ are usually termed Neutral Stability Curves (NSC). Therefore, the dominant transition will be the minimum of the set of minima obtained from the different NSC. This selection provides a critical pair of values (k^c, R_i^c) for which the bifurcation takes place. In the represented case, the dominant perturbation is the axisymmetric one ($n = 0$). The previous methodology must be repeated for each value of external Reynolds number R_o. As a result, a functional dependence between R_i^c and R_o is obtained. The curve which separates stable from unstable regimes in parameter space (R_i, R_o) is usually termed *linear stability curve* or *marginal curve*.

In figure 5.3, the linear stability results for the cases $\eta = 0.5$ and $\eta = 0.8$ is depicted and compared with the *Rayleigh's criterion* of stability. The figure represents the usually termed critical curves over which the linear criterion predicts the presence of a bifurcation. Therefore, for each case, the curve separates two well-distinguished zones. For physical conditions contained below the critical curve, the basic flow (*Couette flow*) is stable, being unstable as long as the critical curve is crossed.

---

[1] The assumption of periodicity of the perturbation fields is justified by experimental evidences. To put it briefly, we are only searching for spatially periodic bifurcated solutions.

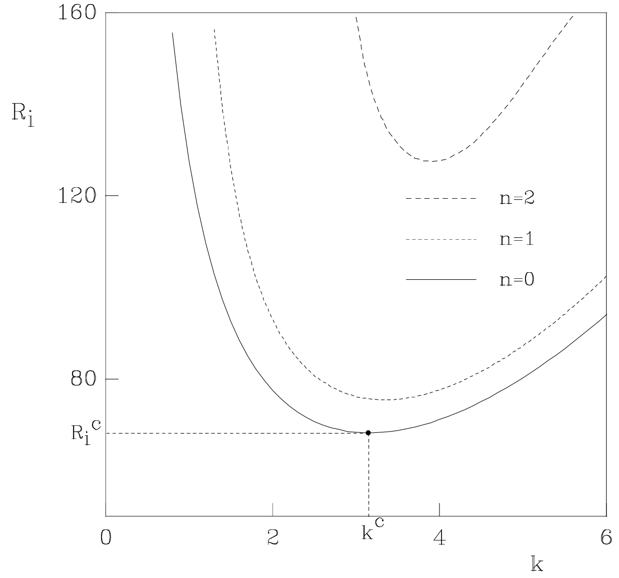

Figure 5.2: Featuring neutral stability curves for the *Couette flow*. The values of the physical parameters are $\eta = 0.5$ and $R_o = 0$. The curves for the first three possible azimuthal modes ($n = 0, 1, 2$) are depicted. On note the presence of a minimum critical point located at $(k^c, R_i^c) = (3.16, 68.19)$.

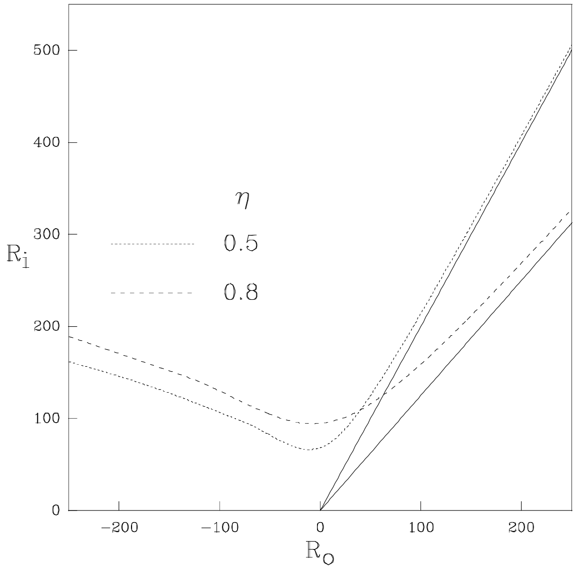

Figure 5.3: Featuring linear stability curves for *Couette flow*. The dotted curves represent the marginal state for the cases $\eta = 0.5$ and $\eta = 0.8$ obtained from the Petrov-Galerkin scheme. Solid lines emerging from the origin represent the non-viscous *Rayleigh's criterion* of stability $R_i = R_o/\eta$ in each case.

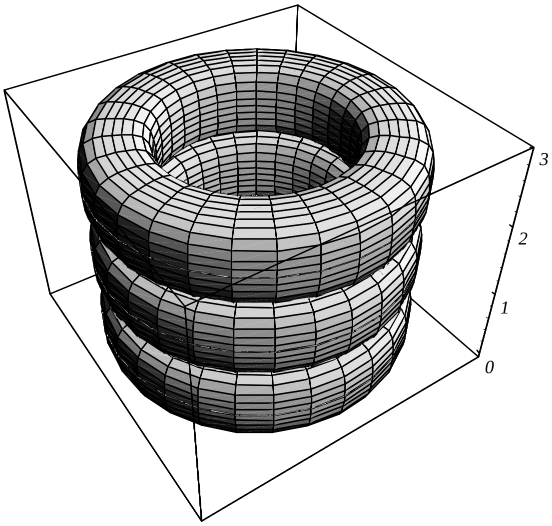

Figure 5.4: Geometrical sketch of *Taylor vortex flow* for the value parameters $\eta = 0.5$, $R_i = 68.19$, $R_o = 0$ and $k_c = 3.16$. The fluid particles remain moving in each one of the toroidal surfaces usually termed *Taylor vortices*.

Another relevant feature of the stability of *Couette flow* is the structure of the secondary flows which appear near criticality. Typically, the emerging patterns just after the inestabilization of *Couette flow* may be steady cellular flows, usually termed *Taylor Vortex flow*, or time periodic flows, usually termed *Spiral flows.* The dominance of one or another depends on the specific physical conditions. On the one hand, *Taylor Vortex flow* appears when considering axisymmetric disturbances as the dominant ones in the critical regime. A curious feature of this flow is its stability under the presence of perturbations. By contrast, *Spiral flow* which only appear in counter-rotation situations, is a very unstable pattern. In figures (5.4) and (5.6), a geometrical representation of the stream functions associated to the two possible bifurcating regimes is depicted. In the first case, when axisymmetric disturbances are the dominant ones, the bifurcation leads to a cellular steady pattern in which the fluid remains constrained to move in toroidal surfaces (*Taylor vortices*) with axial periodicity. Only one constant stream function surface is depicted. In fact, the stream surface which reaches an 80% of the whole gap only is sketched. For the second representation, the same criterion has been considered. In this case, the particles move in a spiral surface which is invariant under specific combinations of axial translations and azimuthal rotations of the form $n\theta + k_c z = cnst.$, with n an integer number.

For the computation of the previous structures, the general Petrov-Galerkin scheme, explained in next section and in appendix D, was used for the particular case of no-sliding effects. In fact, the previous surfaces represent the eigen–stream functions associated with the critical eigenvalues in the bifurcation. The axial periodicity of the patterns can be computed with the same scheme and are the unstable wave numbers under which the bifurcation will take place. Therefore, the representations are only qualitative. For a

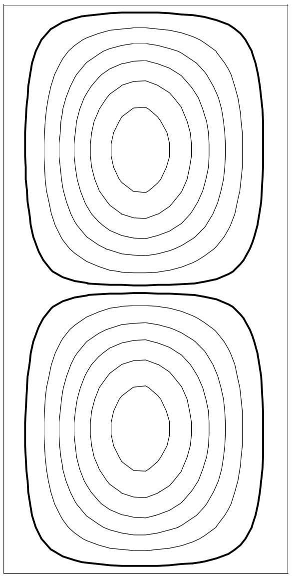

Figure 5.5: Geometrical sketch of *Taylor vortex flow* for the value parameters $\eta = 0.5$, $R_i = 68.19$, $R_o = 0$ and $k_c = 3.16$. Different constant stream function values have been depicted. The thickest line represents a constant azimuthal cut of one pair of toroidal structures represented in previous figure.

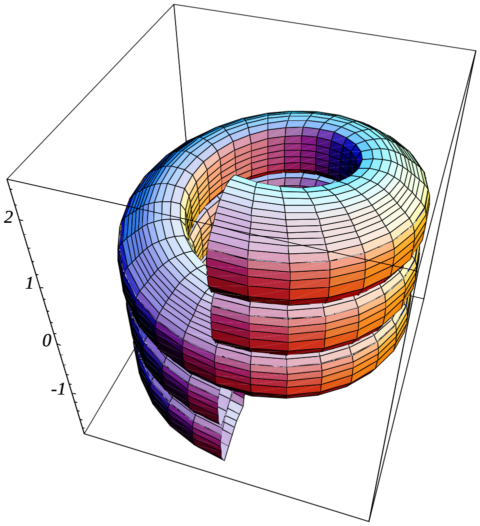

Figure 5.6: Geometrical sketch of *Spiral flow* for the value parameters $\eta = 0.5$, $R_i = 97.89$, $R_o = -80$, $n = -1$ and $k_c = 3.85$. In this case, fluid particles remain moving in each one of the spiral surfaces.

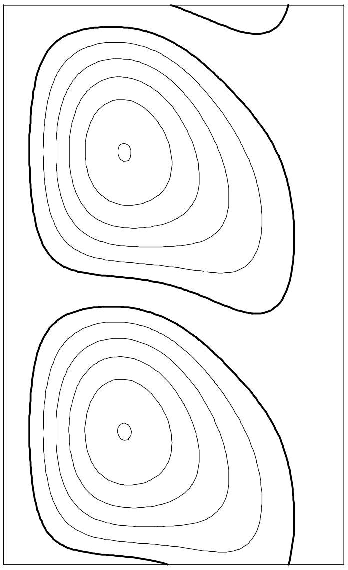

Figure 5.7: Geometrical sketch of *Spiral flow* for the value parameters $\eta = 0.5$, $R_i = 97.89$, $R_o = -80$, $n = -1$ and $k_c = 3.85$. Different constant stream function values have been depicted. The thickest line represents a constant azimuthal cut of one pair of spiral structures represented in figure 5.6.

real representation of the bifurcating patterns, the non-linear integration of the original problem would be needed.

5.2 Spiral Couette Problem–Introduction

In this section, the linear stability of a fluid confined between two coaxial cylinders rotating independently and with axial sliding (Spiral Couette flow) is examined. A wide range of experimental parameters were explored, including two different radius ratio. Zero-*th* order discontinuities are found in the critical surface; they are explained as a result of the competition between the centrifugal and shear instability mechanisms, which appears only in the co–rotating case, close to the rigid body rotation region. In the counter–rotating case, the centrifugal instability is dominant. Due to the competition, the neutral stability curves develop islands of instability, which considerably lower the instability threshold. Specific and robust numerical methods to handle these geometrical complexities were developed. The results are in very good agreement with the experimental data available, and with previous computations.

An incompressible viscous fluid which is contained in the gap between two concentric cylinders that rotate independently about a common axis at constant angular velocities is considered. Forward motion is induced by an inertial sliding of the cylinders relative to one another along the pipe axis. The basic motion whose linear stability will be studied is, therefore, a combination of the Couette flow and the axial velocity field induced by the relative sliding, the so called Spiral Couette flow (Joseph, 1976).

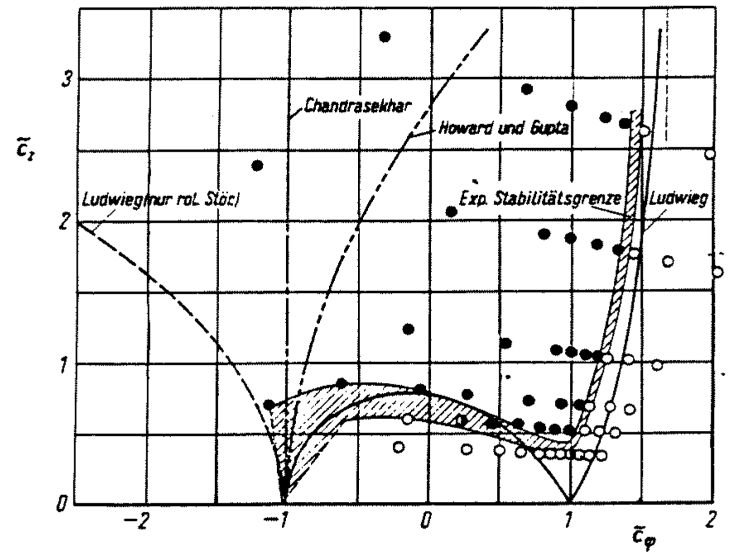

Figure 5.8: Original comparison between inviscid criterion of stability and experimental results, both obtained by Ludwieg in 1964.

This problem was first studied by Kiessling, 1963 and Ludwieg, 1964, who obtained inviscid stability criteria in the narrow gap case. The experiments of Ludwieg, 1964 are, as far as we know, the only experiments made in this problem to date. The results showed the correctedness of the inviscid Ludwieg, 1964 criterion (see figure 5.8), later improved by Wedemeyer, 1967. The general problem was studied by Mott & Joseph, 1968, Hung, Joseph & Munson, 1972 with special emphasis on energy methods; an excellent review can be found in the book of Joseph, 1976, chapter VI. Recently, Ali & Weidman, 1993 made a linear stability analysis of the Spiral Couette flow, in the stationary outer cylinder case, in the so called enclosed geometry, which includes end effects. The more general problem of oscillatory sliding has been recently considered by Hu & Kelly, 1995 and Marques & Lopez, 1997, whose numerical simulations are in good agreement with the experiments of Weisberg, 1996. The previous works dealt with the infinite cylinders case, assuming periodicity in the axial direction. As a result of the sliding, a non–zero mean flow in the axial direction appears, that can only be present in open ends configurations, like in the mentioned Ludwieg, 1964 experiments. The presence of lids enforces a zero axial mean flow; this constraint is enforced by adding a suitable axial pressure gradient, which mimics the lids effect, maintaining the periodicity of the velocity field; this is the usually termed *enclosed case.*

An understanding of the stability of these flows could have applications in some industrial processes like the purification of industrial waste water (Ollis *et al.* , 1991), the production of wire and cables (Tadmor & Bird, 1974) and the optical fiber fabrication techniques (Chida *et al.* , 1982). In all of them, axial sliding in a cylindrical annulus takes place, and the rotation of one or both cylinders change the stability and properties of the flow.

The following sections present an extensive exploration of the linear stability of the Spiral Couette flow mainly in the open ends case in order to compare with existing experimental data, although some computations are made in the enclosed case in order to test our numerical code and quantify the lids effect. The exploration covers a wide range of angular velocities of both cylinders, and two different radius ratio are examined: one corresponds to the Ludwieg (64) experiment, with a radius ratio $\eta = 0.8$, close to the narrow gap case ($\eta \rightarrow 1$). The other case (with a wide gap $\eta = 0.5$) has been considered because the instability appears at lower Reynolds numbers than in the narrow–gap case, and the change in the azimuthal wave numbers to be considered is also smaller, which permits a more detailed analysis.

The chapter is organized as follows. In section 5.3, a complete description of the physical system is given, and the analytical steady solutions are computed for the general case. In section 5.4 the linear differential equations which govern the stability of the first order perturbations are obtained, using a Petrov–Galerkin scheme. The symmetries of the problem are considered in order to reduce the parameter space region to be explored. The neutral stability curves in this problem may have multiple extrema and sharp geometrical forms, and also exhibit disconnected parts. Specific and robust methods for obtaining the neutral stability curves in spite of its geometric complexities are designed. The results of our numerical method are checked with former results obtained previously by Ali & Weidman, 1993. Section 5.5 is concerned with the wide gap case $\eta = 0.5$. For each pair of values Ro and Rz (outer rotation Reynolds number and axial Reynolds number respectively) the neutral stability surface is computed. Complex behaviour is found on the co-rotation zone, specially as the axial Reynolds number is increased. In fact, discontinuities in the critical inner rotation Reynolds surface have been observed. This phenomena is explained in detail as a competition between the centrifugal instability mechanism characteristic of the Taylor–Couette problem and the shear instability mechanism induced by the axial sliding. This interpretation in reinforced by examining the rigid rotation case with sliding. Section 5.6 deals with the narrow–gap case $\eta = 0.8$, where the same features are present. The results are compared with the experimental results of Ludwieg (64) and the linear stability computations of Hung *et al.* (73), reaching good agreement with both. A detailed analysis of the experimental data shows the presence of hysteresis regions associated to the mentioned discontinuities. Finally, section 5.7 offers some conclusions.

5.3 Physical Description; Steady Solutions

The dynamical features of the problem are essentially the same as those described in section 5.1.1. In addition, the inner cylinder is moving parallel to the common axis with a constant velocity U_c (see figure 5.9). The apparently more general flow with both cylinders moving axially is reduced to the present case by Galilean invariance, changing to a reference frame with constant axial speed. As a result, a new nondimensional parameter featuring the axial sliding must be considered. In this case, the Reynolds number $R_z = dU_c/\nu$ will measure the translational velocity of the inner cylinder. Henceforth, all variables will be rendered dimensionless in the same way as in section 5.1.1. As a result, the Navier–Stokes

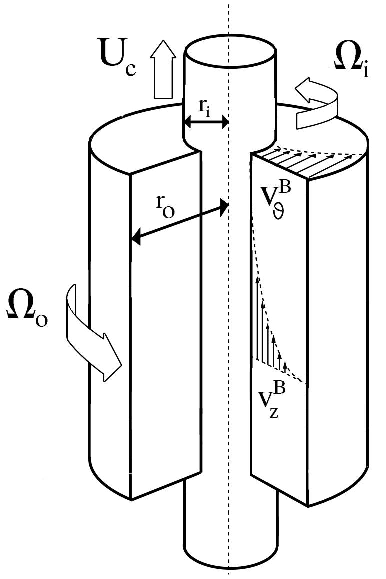

Figure 5.9: Geometric sketch and parameters of the Taylor-Couette problem with axial sliding. The basic flow r_θ^B, v_z^B, driven by the axial motion U_c and the angular rotations Ω_i, Ω_o, is also depicted.

equation and the incompressibility condition for this scaling are given by (5.1), and the boundary conditions are

$$u(r_i) = u(r_o) = 0, \tag{5.19}$$

$$v(r_i) = R_i, \quad v(r_o) = R_o, \tag{5.20}$$

$$w(r_i, t) = R_z, \quad w(r_o) = 0, \tag{5.21}$$

where $r_i = \eta/(1-\eta)$, $r_o = 1/(1-\eta)$.

In order to compare with experiments and with other previous work, two different situations are considered in the present research. In both, the basic flow velocity field is independent of the axial direction, but in one case the axial pressure gradient is zero (*open flow*) and nonzero in the other (*enclosed flow*). The nonzero axial pressure gradient in the enclosed flow case is physically represented by the presence of endwalls and allows us to enforce a net zero axial mass flux, not only for the base flow but also for the perturbed flow. The only experiments of the Taylor–Couette flow with axial sliding of the inner cylinder known to us are those of Ludwieg (64), which were carried out in an annulus with open endwalls. The use of an axial pressure gradient to include the large scale endwall effects has been implemented by Ali & Weidman, 1993, in the linear analysis of Taylor–Couette flow with axial sliding, in the enclosed case and with the outer cylinder at rest. This effect was also taken into account by other authors (Edwards *et al.* , 1991, Sanchez, Crespo & Marques, 1993) in the Couette flow without sliding, where the bifurcation to spirals in the counter–rotating case develop weak axial flows. The axial pressure gradient is fixed by the zero axial mass flow condition

$$\int_{z=0} w\, r\, dr\, d\theta = 0. \tag{5.22}$$

The steady velocity field $\mathbf{v}_B$ independent on the axial and azimuthal variables that verifies the previous condition is

$$u_B = 0,\ v_B = Ar + \frac{B}{r},\ w_B = C\ln(\frac{r}{r_o}) + \frac{P}{4}(r^2 - r_o^2), \tag{5.23}$$

as can be seen in (Joseph, 1976). The constants A, B, C are given by

$$A = \frac{Ro - \eta Ri}{1+\eta},\ B = \frac{\eta(Ri - \eta Ro)}{(1-\eta)(1-\eta^2)},\ C = \frac{1}{\ln\eta}\Big(Rz + \frac{P(1+\eta)}{4(1-\eta)}\Big) \tag{5.24}$$

and P is the non-dimensional Poiseuille number $P = (dp^*/dz^*)d^3/(\rho^*\nu^2)$ measuring the imposed axial pressure gradient. In the open flow case, $P = 0$; in the enclosed case, the mass conservation condition gives P as a function of Rz:

$$P = -4Rz\frac{(1-\eta)(2\eta^2\ln\eta + 1 - \eta^2)}{(1+\eta)[(1+\eta^2)\ln\eta + 1 - \eta^2]}. \tag{5.25}$$

5.4 Linear Stability of Spiral Couette Flow

In the preceding section the basic flow was obtained. Now a perturbation of this basic state by a small disturbance which is assumed to vary periodically in the azimuthal and axial directions is considered:

$$\mathbf{v}(r,\theta,z,t) = \mathbf{v}_B(r) + \mathrm{e}^{\mathrm{i}(n\theta+kz)+\lambda t}\mathbf{u}(r), \tag{5.26}$$

$$p(r,\theta,z,t) = p_B(r,z) + p'(r)\mathrm{e}^{\mathrm{i}(n\theta+kz)+\lambda t}, \tag{5.27}$$

where $\mathbf{v}_B = (0, v_B, w_B)$ is given by (5.23) and the boundary conditions for $\mathbf{u}$ are homogeneous, $\mathbf{u}(r_i) = \mathbf{u}(r_o) = \mathbf{0}$. Linearizing the Navier–Stokes equations near the basic solution, the following eigenvalue problem is obtained:

$$\lambda\mathbf{u} = -\nabla p' + \Delta\mathbf{u} - \mathbf{v}_B\cdot\nabla\mathbf{u} - \mathbf{u}\cdot\nabla\mathbf{v}_B. \tag{5.28}$$

In order to solve (5.28) numerically, a spatial discretization is accomplished by projecting (5.28) onto a suitable basis. The space of divergence-free vector fields satisfying the boundary conditions of the problem is

$$V = \{\mathbf{u}\in(\mathcal{L}_2(r_i,r_o))^3 \mid \nabla\cdot\mathbf{u} = 0,\ \mathbf{u}(r_i) = \mathbf{u}(r_o) = 0\}, \tag{5.29}$$

where $(\mathcal{L}_2(r_i,r_o))^3$ is the Hilbert space of square-integrable vectorial-functions defined in the interval (r_i, r_o), with the inner product,

$$<\mathbf{u},\mathbf{v}> = \int_{r_i}^{r_o} \mathbf{u}^*\cdot\mathbf{v}\ r dr, \tag{5.30}$$

where * denotes the complex conjugate. For any $\mathbf{u} \in V$ and any function p, we have $< \mathbf{u}, \nabla p >= 0$. Therefore expanding $\mathbf{u}$ in a suitable basis of V,

$$\mathbf{u} = \sum_{\alpha} a_\alpha \mathbf{u}_\alpha, \qquad \mathbf{u}_\alpha \in V, \tag{5.31}$$

and projecting the linearized equations (5.28) onto V the pressure term disappears, and a linear system for the coefficients a_α is obtained:

$$\lambda \sum_{\beta} < \tilde{\mathbf{u}}_\alpha, \mathbf{u}_\beta > a_\beta = \sum_{\beta} < \tilde{\mathbf{u}}_\alpha, \Delta \mathbf{u}_\beta - \mathbf{v}_B \cdot \nabla \mathbf{u}_\beta - \mathbf{u}_\beta \cdot \nabla \mathbf{v}_B > a_\beta. \tag{5.32}$$

A Petrov-Galerkin scheme is now implemented, where the basis used to expand the unknown velocity, $\{\mathbf{u}_\alpha\}$, differs from that used to project the equations, $\{\tilde{\mathbf{u}}_\alpha\}$. A comprehensive analysis of the method can be found in appendix D. The divergence-free condition for a velocity field of the form (D.20) is $D_+ u + \mathrm{i}nv/r + \mathrm{i}kw = 0$, and a basis for V is obtained by taking,

$$\mathbf{u}_j^1 = (0, -rkh_j(r), nh_j(r)), \tag{5.33}$$

$$\mathbf{u}_j^2 = (-\mathrm{i}kf_j(r), 0, D_+ f_j(r)), \tag{5.34}$$

where $D = \partial_r$, $D_+ = D + 1/r$. The functions f_j and h_j must satisfy the homogeneous boundary conditions $f_j = f_j' = h_j = 0$ on r_i and r_o.

Introducing the new radial coordinate $x = 2(r - r_i) - 1$, $x \in [-1, +1]$ and using Chebyshev polynomials T_j, a simple choice for f_j and h_j, which satisfy the homogeneous boundary conditions, is

$$f_j(r) = (1 - x^2)^2 T_{j-1}(x), \quad h_j(r) = (1 - x^2) T_{j-1}(x), \tag{5.35}$$

where j ranges from 1 to M, the number of Chebyshev polynomials used. In order to preserve the orthogonality relationships between the Chebyshev polynomials, and to avoid $1/r$ factors in the inner products in (5.32), a suitable choice for the projection basis $\tilde{\mathbf{u}}$ is

$$\tilde{f}_j(r) = r^2 (1 - x^2)^{3/2} T_{j-1}(x), \quad \tilde{h}_j(r) = r^2 (1 - x^2)^{\frac{1}{2}} T_{j-1}(x). \tag{5.36}$$

With this choice, all the inner products in (5.32) involve polynomials, except those containing the logarithmic term in w_B, and therefore they can be numerically computed exactly using Gauss–Chebyshev quadrature (Isaacson & Keller, 1966). Finally, a generalized eigenvalue system of the following form is obtained:

$$\lambda G \mathbf{x} = H \mathbf{x}, \tag{5.37}$$

where the vector $\mathbf{x}$ contains the real and imaginary parts of the coefficients a_α in (5.31), and G, H are constant matrices, with G positive definite. The explicit expressions of the matrix elements of G and H are given in the appendix D.

Let us consider the symmetries of our problem. The Navier–Stokes equations are invariant with respect to the specular reflections $\{z \to -z,\ w \to -w\}$ and $\{\theta \to -\theta,\ v \to -v\}$. They are also invariant with respect to rotations around the axis, axial translations

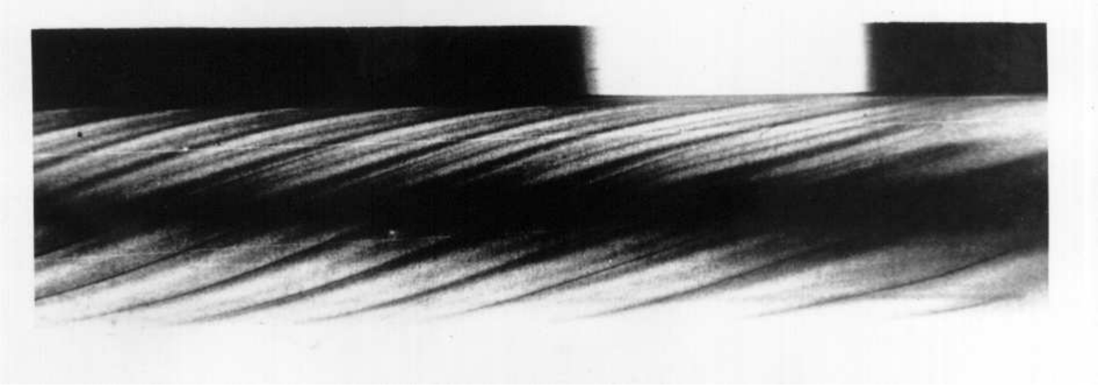

Figure 5.10: Experimental visualization of spiral secondary regime (from Wedemeyer, 1967).

and time translations. The boundary conditions break some of these symmetries. *Ri* or *Ro* different from zero breaks the specular reflection $\theta \to -\theta$, and $Rz \neq 0$ breaks the specular reflection $z \to -z$. In order to keep the invariance, the sign of these Reynolds numbers, as well as the corresponding wave numbers n and k in the solution of the linearized system (D.32), must be changed. Thus, the symmetries allow us to restrict the computations to the cases $Rz > 0$ and $Ri > 0$. Furthermore, since the Navier–Stokes equations are real, the complex conjugate of a perturbation (D.20, D.21) is also a solution, and the sign of n, k and the imaginary part of λ can be changed simultaneously. Therefore, the analysis can be restricted to the computations to the $k \geq 0$ case.

When n and k are both different from zero, the eigenvector of the linear problem has the form of a spiral pattern (see fig. 5.10, showing an experimentally observed spiral flow).

The wave numbers n and k, together with the imaginary part of the critical eigenvalue, $\omega = \mathrm{Im}\lambda$, fix the shape and speed of the spiral. The angle α of the spiral with a z–constant plane is given by $\tan\alpha = -n/(r_o k) = -(1-\eta)n/k$; the speed of the spiral in the axial direction (on a θ–constant line) is $c = -\omega/k$, and in the azimuthal direction (on a z–constant line) it is $\omega_{sp} = -\omega/n$. In the $n = 0$ case the pattern is axisymmetric and steady Taylor vortices appear for $\omega = 0$, being travelling ones if $\omega \neq 0$, with axial velocity c.

If $Rz = 0$, the symmetry $z \to -z$ is not broken, and at the bifurcation point, in the $n \neq 0$ case, two pairs of purely imaginary eigenvalues bifurcate simultaneously, representing spirals with opposite slope –or angle– (see Iooss & Adelmeyer, 1992). These spirals have opposite values of n. For $Rz \neq 0$, the corresponding eigenvalues split apart, and one of the two spirals $\pm n$ becomes dominant. Therefore, mode competition and switching between $+n$ and $-n$ for Rz close to zero is expected.

5.4.1 Computation of the Neutral Stability Curves

Let σ be the real part of the first eigenvalue of the linear system (D.32) which crosses the imaginary axis. The stability of the basic flow is conditioned by the sign of σ. For negative values of σ, the basic flow is stable under perturbations. When σ is zero or slightly positive, the steady flow becomes unstable and bifurcated secondary flows may appear. It should be noted that $\sigma(n, k, \eta, Ri, Ro, Rz)$ is a function of the physical parameters which play an essential role in the dynamics of the system. For fixed values of the parameters η, Ro and Rz, and n and k given, the inner Reynolds number $Ri_c(n,k)$ such that $\sigma = 0$ is computed. The critical inner Reynolds number is given by $Ri_{\text{crit}} = \min_{n,k} Ri_c(n,k)$, and the corresponding values of n, k are the critical azimuthal and axial wave numbers n_{crit}, k_{crit} which will fix the geometrical shape of the bifurcating solutions, which may be a spiral flow or travelling Taylor vortices. Moreover, the imaginary part of the critical eigenvalue, ω_{crit}, gives the angular frequency of the secondary pattern. Again, the critical values are functions of the parameters (η, Ro, Rz).

The curves in the (k, Ri) plane given by $\sigma(k, Ri) = 0$ are commonly termed Neutral Stability Curves (NSC). The main goal at this stage is to compute the absolute minimum of the NSC, which will give the critical parameters $(k_{\text{crit}}, Ri_{\text{crit}})$; in this way, the absolute minimum of the set of the NSC corresponding to integer values of n will be found. As will be seen below, the NSC curves for this problem may have multiple extrema (maximums and minimums), exhibit disconnected parts and sharp geometrical forms. In addition, these curves may exhibit multievaluation branches as functions of k. Moreover, these features may change abruptly in certain parameter ranges (see fig. 5.13). Standard methods applied to a regular grid in the plane (k, Ri) require extremely accurate computations. Consequently, an alternative method has been considered (for a comprehensive study, see appendix D).

A local extremum (k_c, Ri_c) must satisfy the following conditions:

$$\sigma(k_c, Ri_c) = 0, \quad \partial_k \sigma(k_c, Ri_c) = 0 \tag{5.38}$$

Using the Implicit Function Theorem, it can be seen that the local extremum is a minimum if, in addition, the inequality $\partial^2_{k,k}\sigma\partial_{Ri}\sigma < 0$ is satisfied. In order to solve equation (5.38), a two-dimensional Newton-Raphson method has been considered. The convergence of the method depends on the topological structure of the basin of attraction, and is strongly dependent on the initial point of iteration in the plane (k, Ri). In order to optimize the process, a predictor steepest-descent method has been used. This gradient method allows to be approached to the neighboring zones where the convergence is almost ensured. The predictor scheme is able to detect islands of instability, independently of their size and topological features.

5.4.2 Comparisons Open-Enclosed Flow ($Ro = 0$)

In order to check the numerical scheme, the linear stability of the open and enclosed flows have been studied for $\eta = 0.4$.

For the enclosed flow case, the present computations are in complete agreement with Ali & Weidman, 1993 results. The numerical results are displayed in figures 5.11 and 5.12. For high axial sliding Reynolds number, the azimuthal dominant mode is $n = 4$, as previously predicted by Ali & Weidman, 1993.

In order to study the effect of the zero mean flow, the same computations were carried out for the open-flow case. The qualitative behaviour of the system is similar to the previous case analyzed above, but some quantitative differences should be pointed out. First, the global end effects included in the enclosed case has a stabilizing effect on the basic flow,

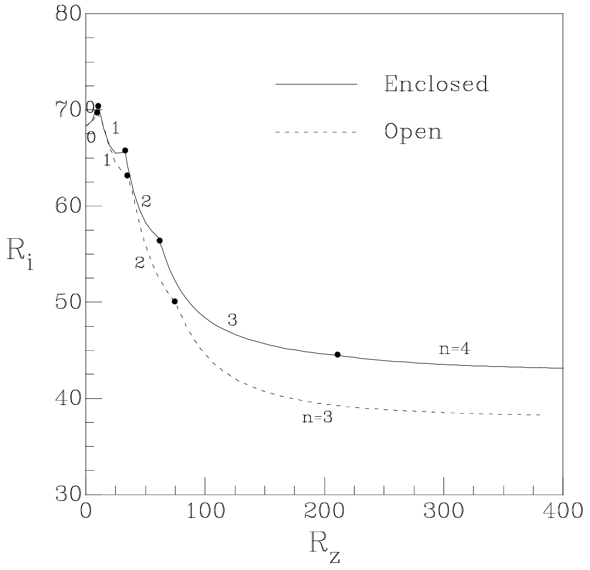

Figure 5.11: Comparison between the open and enclosed (Ali & Weidman, 1993) situations. Dominant azimuthal wave numbers have been sketched. The points reflect the change of mode.

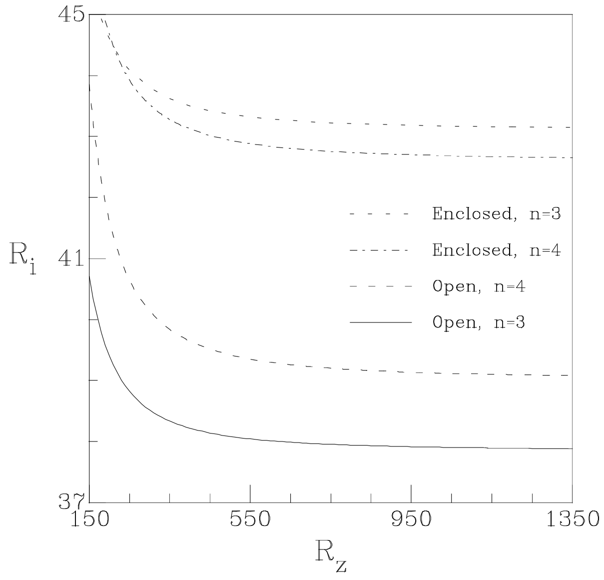

Figure 5.12: Comparison between the open and enclosed (Ali & Weidman, 1993) situations. Asymptotic states for high axial Reynolds number Rz.

effect that increases at high axial Reynolds number (see figure 5.11). This enhancement of stability in the enclosed case is similar to the one observed by Marques & Lopez, 1997 when the inner cylinder undergoes axial oscillations. Second, the asymptotic azimuthal wave number n is different, with the dominant azimuthal wave number $n = 3$ in the open case, and $n = 4$ in the enclosed one, in agreement with Ali & Weidman, 1993 (see figure 5.12). However, only the open flow case will be considered from now on. As a matter of fact, the previous experimental analysis were done under the open axial circulation configuration. The inner cylinder critical rotation Reynolds number Ri_{crit} was computed as a function of (Rz, Ro) for two different values of η, 0.5 and 0.8. This was carried out in the range $0 < Rz < 150$ and $-250 < Ro < 250$. Computations were restricted to the $Rz > 0$, $Ri > 0$ and $k > 0$ cases, on the basis of the symmetries of the physical problem.

5.5 Instability Results for $\eta = 0.5$

The computation of $Ri_c(Rz, Ro)$ as a function of Rz, Ro for the wide gap $\eta = 0.5$, gives as a first unexpected result the presence of a zero–order discontinuity in Ri_c, in the co–rotating case ($Ro > 0$). Although this behavior had been considered possible by some authors (Davis & Rosenblat, 1977), specific examples showing this kind of discontinuities are very unusual in Fluid Mechanics literature.

For $Ro = 200$ the discontinuity appears for $Rz = 82.63$. Fig. 5.13 shows the critical Ri as a function of k. For $Rz = 80$ the dominant mode is $n = -1$, giving $Ri_c = 373.43$ and $k_c = 1.68$; but for $Rz = 82.63$ the marginal stability curve of the $n = -4$ mode develops an island of instability for a much lower $Ri_c = 119.13$, introducing a discontinuity in Ri_c. It should also be noted that the change in n_{crit} is not ± 1 as usual, but changes in three units. The island of instability is very small (figure 5.13, $Rz = 84$), growing its size as long as Rz is further increased from the discontinuity point. All these features make the numerical computation of the critical parameters very difficult from the algorithmic point of view. For these reasons, specific numerical methods, outlined in section 5.4.1, were developed in order to detect the islands as soon as they appear.

Before crossing the Ri_c discontinuity, the marginal stability curve has a single extrema, a minimum (figure 5.13, $Rz = 80$), giving the critical parameter values (Ri_c, k_c). After crossing, and due to the appearance of the island, we have three extrema, two minima and a maximum, and the marginal stability curve has two disconnected branches. If we move to higher Rz values, the island grows until it merges with the other branch (figure 5.13, $Rz = 120$ and $Rz = 122$); the marginal curve then has now a single minimum. Plotting the position of all the extrema as a function of Rz, an S-shaped curve (see figure 5.25) is obtained, which shows that the critical surface is multievaluated and continuous but folded in such a way that a cusp develops. Figure 5.14 shows a perspective view of this critical surface.

The discontinuity of the critical parameter depends on the experimental way of approaching to this conflictive zone. For Ri remain fixed the computation of $Rz_c(Ri, Ro)$ results in a continuous surface, formed by all three sheets in the cusp region. In fact, this exactly is the followed procedure in order to obtain the critical surface in the cusp region, because the critical wave number n can also change. For dynamical systems that depend

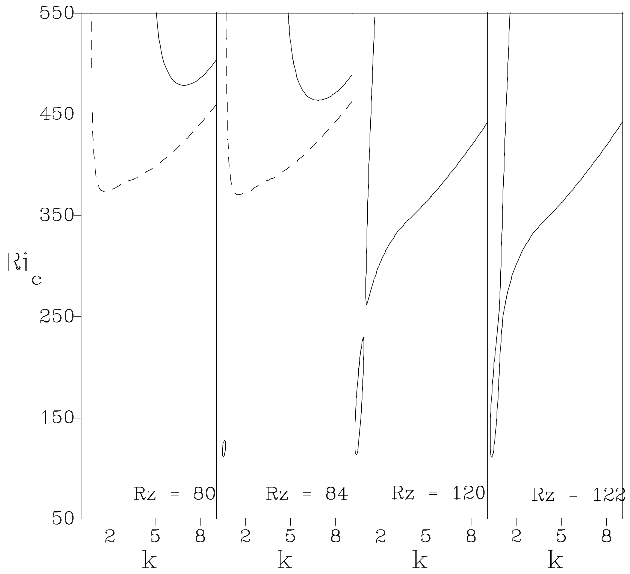

Figure 5.13: Formation and evolution of an island of instability for $\eta = 0.5$, $Ro = 200$. The solid line corresponds to the $n = -4$ mode, and the dashed one to $n = -1$.

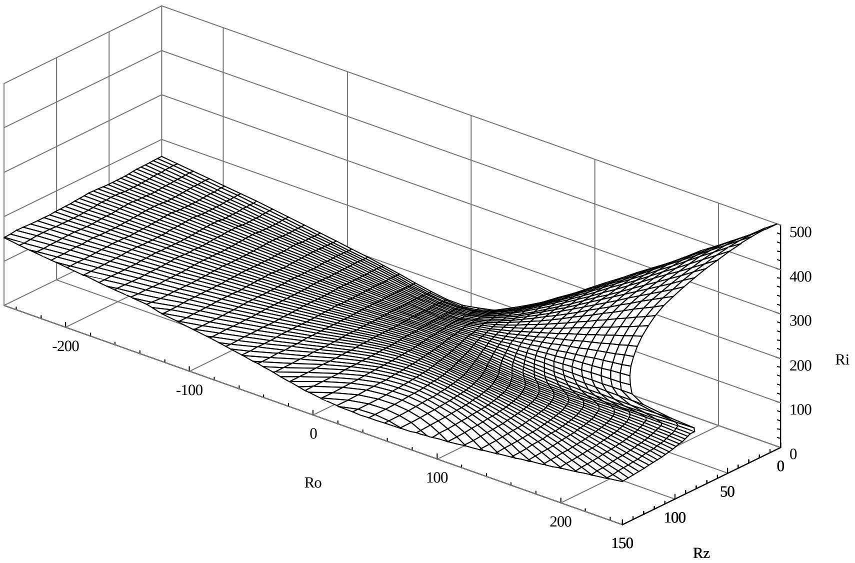

Figure 5.14: Perspective view of the critical surface $Ri_c(Ro, Rz)$ for $\eta = 0.5$.

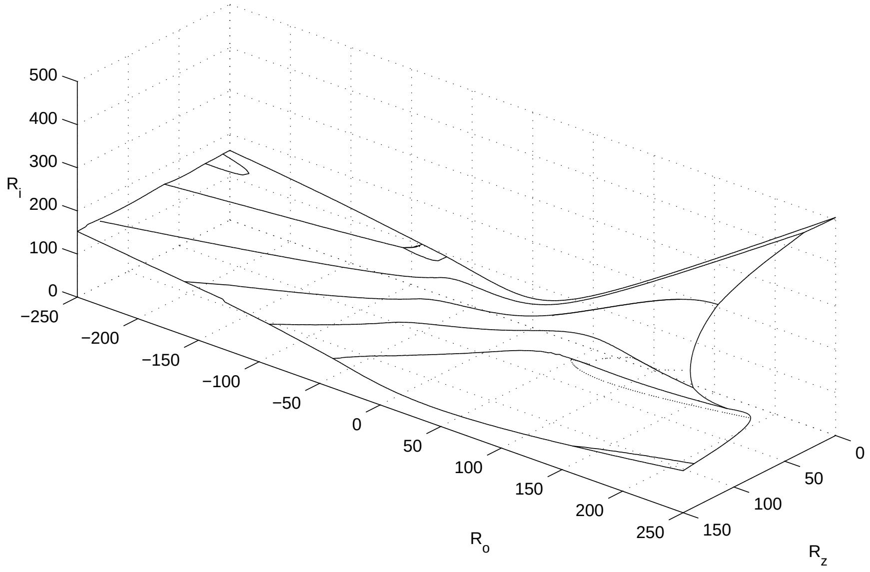

Figure 5.15: Perspective view of the critical surface $Ri_c(Rz, Ro)$, explicitly showing the changes in the dominant azimuthal mode n at criticality.

on a sufficient number of parameters, the critical surface (a manifold, in the general case) is likely to present discontinuities of the same or more complex kind. As we lack *a priori* knowledge of this possibility, the use of robust strategies to find the critical points, like those which have been implemented, becomes necessary.

Figure 5.15 shows the same critical surface with the curves corresponding to a change in the critical azimuthal wave number n. Along these curves, the change in n_{crit} is always ± 1, unless very close to the $Rz = 0$ axis, where the competition between modes $\pm n$ is strong. As already mentioned, the symmetries of the problem for $Rz = 0$ makes the eigenvalues corresponding to $\pm n$ bifurcate simultaneously. When the the symmetry breaking is small ($Rz \sim 0$), both eigenvalues are very close, and switching occurs between both critical surfaces close to the axis. In the region of the cusp, near the discontinuity in Ri_c, the increment in n_c may exceed the unity, because of the jump discontinuity between the different sheets of the critical surface; but as long as the displacement is done on the critical surface, the change in n_c is also ± 1.

The projection of the curves corresponding to a change in the azimuthal wave number n are plotted in fig. 5.16, along with the edges of the cusp region. The discontinuity in Ri_c corresponds to the upper edge of the fold region, and inside it the dominant azimuthal wave number is $n = -4$, except at the very end ($Ro \sim 250$) where the mode $n = -3$ becomes dominant.

The coordinates of the cusp point are $Ro = 93.22$, $Rz = 73.41$, $Ri_c = 107.63$, inside the region $n_c = -3$, but very close to the border with $n = -4$. Although this cusp point could be interpreted as being a bifurcation point of codimension higher than 1, it is *not*. The cusp point is characterized by having a tangent plane parallel to the Ri axis, with an inflexion point in the Ro-constant section. But if we look at the critical surface from

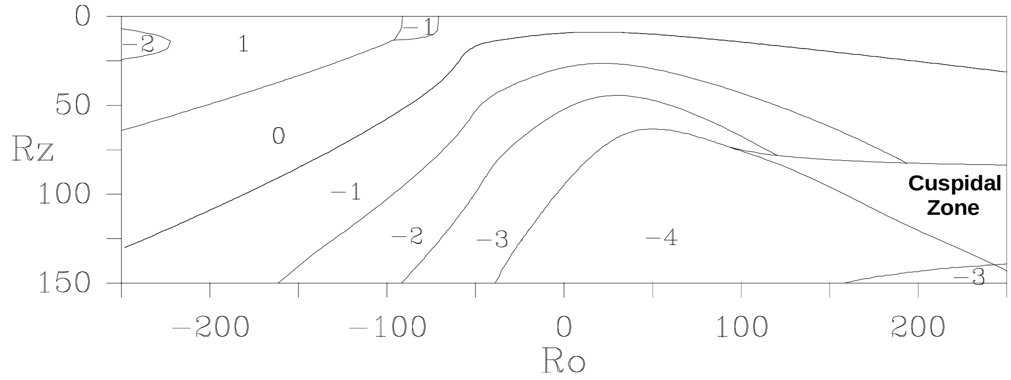

Figure 5.16: Dominant azimuthal mode n at criticality, as a function of Ro, Rz; $\eta = 0.5$

another point of view (for example changing Ri to a linear combination of the Reynolds numbers, as for experimental purposes), the cusp point changes its position on the surface. In fact, looking for the critical Rz number with Ri, Ro fixed, all the folding region is now univaluated and Rz is continuous. Discontinuities also exist in this case (in Rz), along with a multievaluated critical surface, but now in a different region of the critical surface. Figure 5.25 shows that in the upper right corner of fig. 5.15, Rz is multievaluated, and a discontinuity appears. These discontinuities or folded structures may have important consequences from the experimental point of view, like hysteresis phenomena, as well as the discontinuity in Ri_c.

The geometrical shape of the secondary patterns which appear in this case have been depicted in figures 5.17, 5.18, 5.19 and 5.20. First, figures 5.17, 5.18 feature the generally termed *travelling Taylor vortices*, corresponding to dominant cellular axisymmetric structures which propagate in the axial direction. Figures 5.19 and 5.20 feature the secondary spiral flow.

Figures 5.21, 5.22, 5.23 and 5.24 show Ri_c, ω_c, α and c as a function of Ro for different values of Rz, respectively. The critical Reynolds number Ri_c (fig. 5.21 is almost independent of Rz in the counter–rotating region $Ro < 0$. But in the co–rotating region, where the cusp develops, two well separated kinds of behavior are exhibited: for small axial sliding Rz, before the discontinuity, Ri_c is very close to the values without sliding (Taylor–Couette flow). For higher axial sliding, after the discontinuity, Ri_c falls to much lower values. The effect of the axial sliding is destabilizing, but the effect is important only in the co–rotating case, after the discontinuity. The centrifugal instability seems the dominant mechanism (as in Taylor–Couette, $Rz = 0$) except after the discontinuity, where a shear instability due to the axial sliding becomes dominant; the cuspidal zone can be interpreted as the transition region between both mechanisms. This qualitative change can also be noticed in the angle of the spiral pattern α (fig. 5.23, which shows a jump from values less than 10^o to values close to 70^o. This dramatic change in shape is also reflected in the axial speed of the spirals, in fig. 5.24. It is noted that the shear–instability dominated branch is very close to the solid body rotation line, where the centrifugal instability does not apply.

The imaginary part of the critical eigenvalue, ω_c, changes in a linear way with Ro

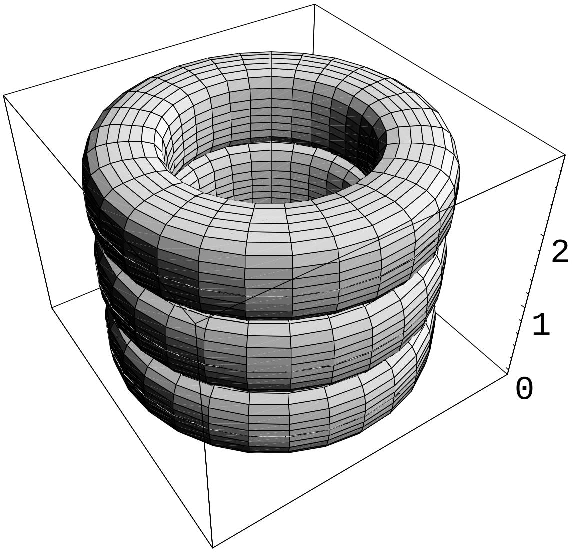

Figure 5.17: Geometrical sketch of *travelling Taylor vortices* for the value parameters $\eta = 0.5$, $R_i = 71.70$, $R_o = -30$, $R_z = 10.0$, $n = 0$ and $k_c = 3.26$.

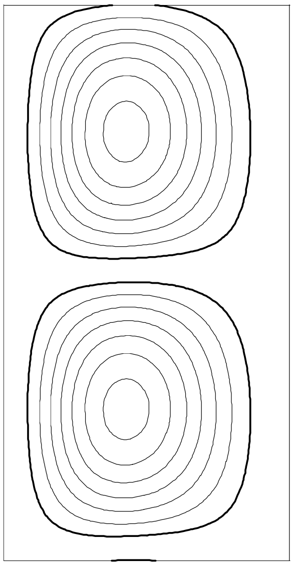

Figure 5.18: Geometrical sketch of *travelling Taylor vortices* for the value parameters $\eta = 0.5$, $R_i = 71.70$, $R_o = -30$, $R_z = 10.0$, $n = 0$ and $k_c = 3.26$. Different constant stream function values have been depicted. The thickest line represents a constant azimuthal cut of one pair of spiral structures represented in previous figure.

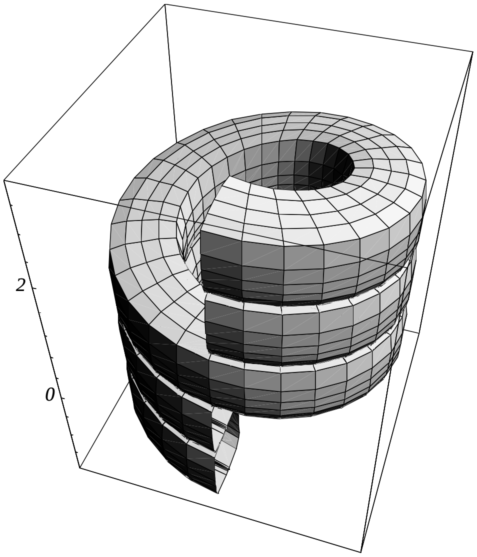

Figure 5.19: Geometrical sketch of *Spiral Flow* for the value parameters $\eta = 0.5$, $R_i = 95.93$, $R_o = 30$, $R_z = 10.0$, $n = -1$ and $k_c = 3.23$.

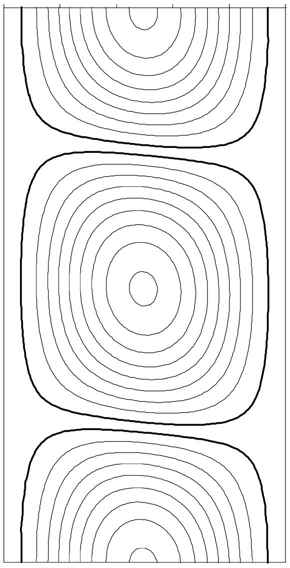

Figure 5.20: Geometrical sketch of *Spiral Flow* for the value parameters $\eta = 0.5$, $R_i = 95.93$, $R_o = 30$, $R_z = 10.0$, $n = -1$ and $k_c = 3.23$. Different constant stream function values have been depicted. The thickest line represents a constant azimuthal cut of one pair of spiral structures represented in the preceding figure.

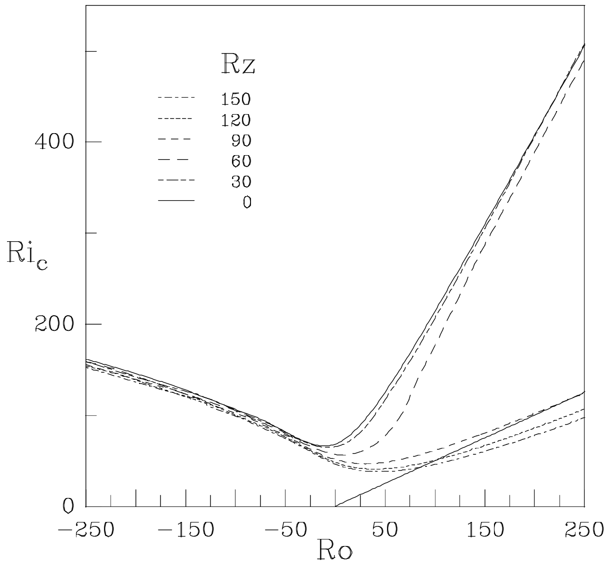

Figure 5.21: Critical parameters for $\eta = 0.5$, as functions of the outer Reynolds number Ro. Featuring, critical inner Reynolds number Ri_c; the solid straight line is the rigid rotation line $Ri = \eta Ro$.

(figure 5.22), except for jumps when the azimuthal mode n changes. Looking at fig. 5.16, a progressive decreasing of the wave number n, as Rz is increased, can be observed except in two regions: the first one, close to $Rz = 0$ in the counter–rotating area, displays competition between $\pm n$ modes, due to the breaking of the reflexional symmetry $z \to -z$, as described in 5.4. The second region, after the discontinuity, shows a kind of saturation; the azimuthal $n = -4$ mode is dominant in a very large area.

Figures 5.25, 5.26, 5.27 and 5.28 respectively show Ri_c, ω_c, α and c as a function of Rz for different values of Ro in the co–rotating case. In figure 5.25, sections of the cusp region are displayed; the critical Ri_c is, in fact, the minimum of the values in the multievaluated region, so a discontinuity takes place, growing its size as long as Ro is further increased. The discontinuity has been displayed in the remaining critical parameter plots, figures 5.26 5.27, 5.28. The bicritical points, where the azimuthal wave number n changes and two eigenvalues bifurcates simultaneously, are distinguished with a vertical bar. The dominant mode for small sliding (Rz close to zero) is axisymmetric ($n = 0$). Since the imaginary part of the critical eigenvalue is not zero (except for $Ro = 0$, see figure 5.26, Taylor vortices which travel axially with a speed c (showed in figure 5.28) appear. The effect of the sliding on these axisymmetric modes is slightly stabilizing, in contrast with their unstabilizing effect on the non-axisymmetric ones, mainly in the co–rotating region.

Figures 5.29, 5.30, 5.31 and 5.32 show Ri_c, ω_c, α and c as a function of Rz for different values of Ro in the counter–rotating case. Here all the critical parameters change smoothly, in an almost linear way. Figure 5.29 shows that the critical Reynolds number Ri_c is almost independent of the axial sliding Rz for $Ro < 0$, suggesting that the centrifugal instability is the dominant instability mechanism as noted before.

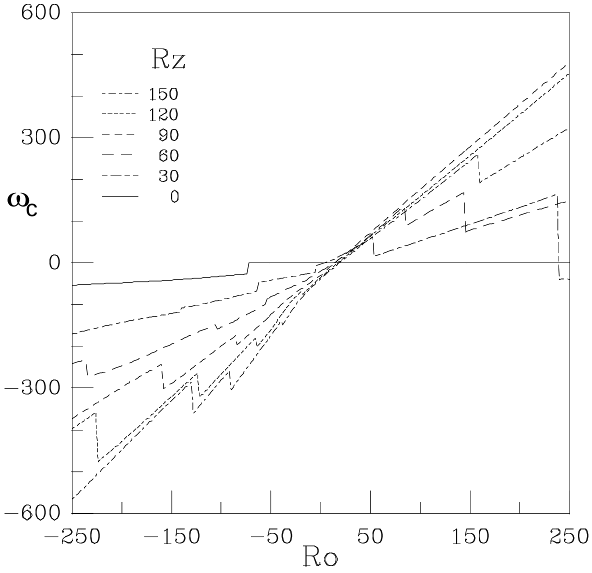

Figure 5.22: Critical parameters for $\eta = 0.5$, as functions of the outer Reynolds number *Ro*. Featuring the imaginary part of the critical eigenvalue ω_c.

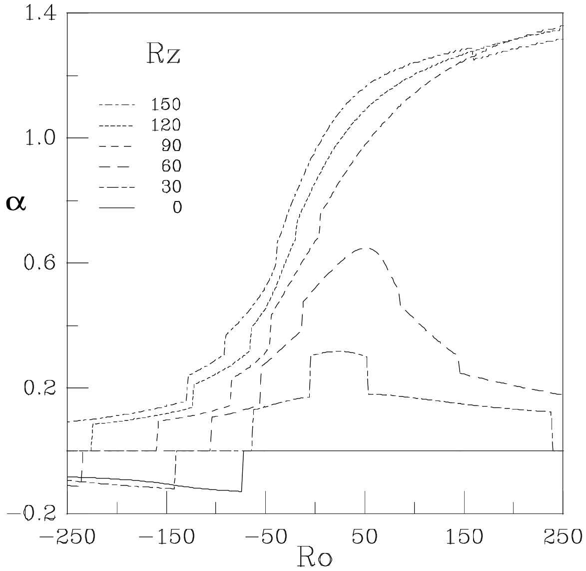

Figure 5.23: Critical parameters for $\eta = 0.5$, as functions of the outer Reynolds number *Ro*. Featuring the angle of the spiral pattern α.

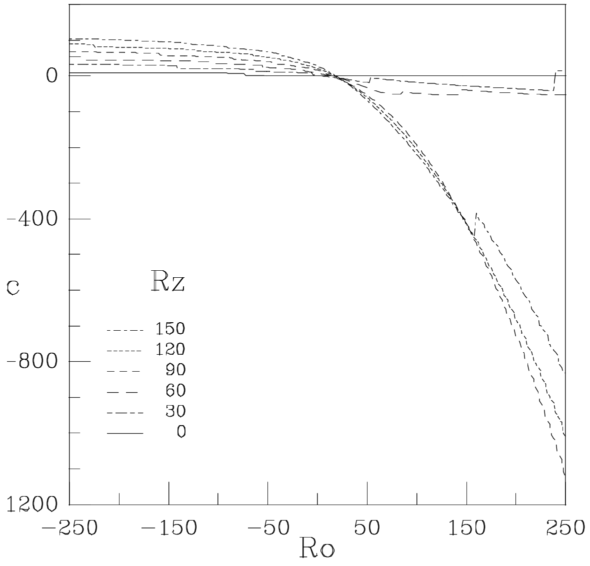

Figure 5.24: Critical parameters for $\eta = 0.5$, as functions of the outer Reynolds number *Ro*. Featuring axial pattern velocity *c*.

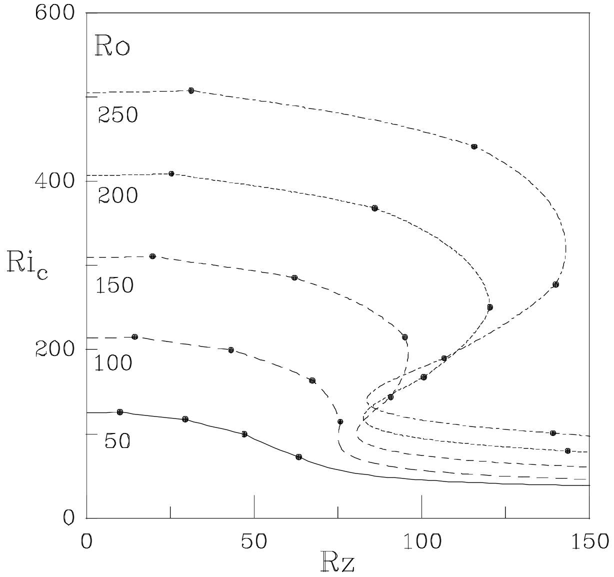

Figure 5.25: Critical parameters for $\eta = 0.5$, as functions of the axial Reynolds number *Rz* in the co–rotating case $Ro > 0$. Featuring critical inner Reynolds number Ri_c. The dots are exactly located at the azimuthal mode transition states.

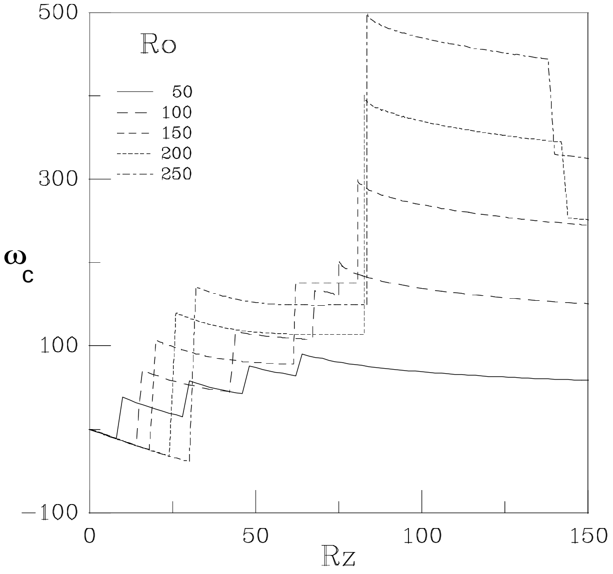

Figure 5.26: Critical parameters for $\eta = 0.5$, as functions of the axial Reynolds number Rz in the co–rotating case $Ro > 0$. Featured is imaginary part of the critical eigenvalue ω_c.

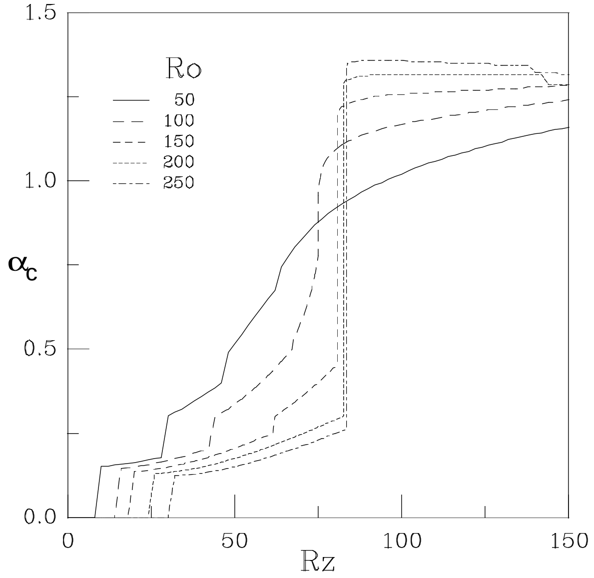

Figure 5.27: Critical parameters for $\eta = 0.5$, as functions of the axial Reynolds number Rz in the co–rotating case $Ro > 0$. Featured is the angle of the bifurcating spiral pattern α.

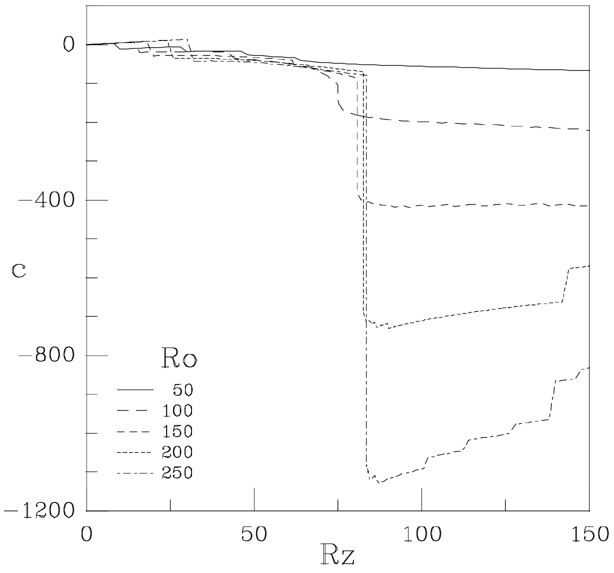

Figure 5.28: Critical parameters for $\eta = 0.5$, as functions of the axial Reynolds number Rz in the co–rotating case $Ro > 0$. Featured is the axial pattern velocity c.

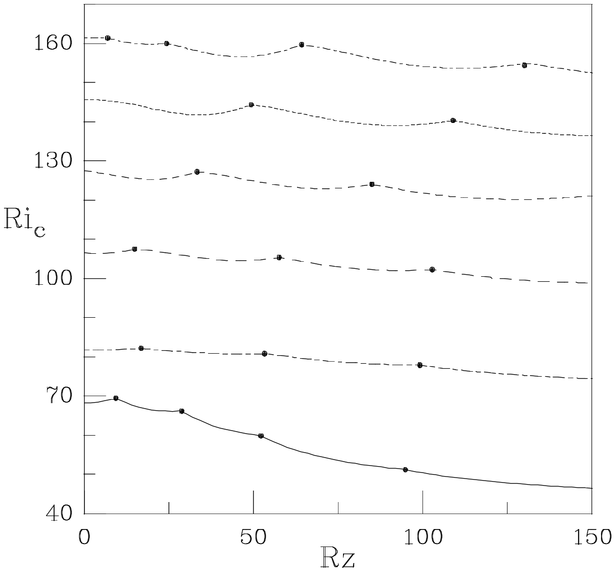

Figure 5.29: Critical parameters for $\eta = 0.5$, as functions of the axial Reynolds number Rz in the counter–rotating case $Ro < 0$. Featured is the critical inner Reynolds number Ri_c. The represented dots are exactly located at the dominance transition points between different azimuthal modes.

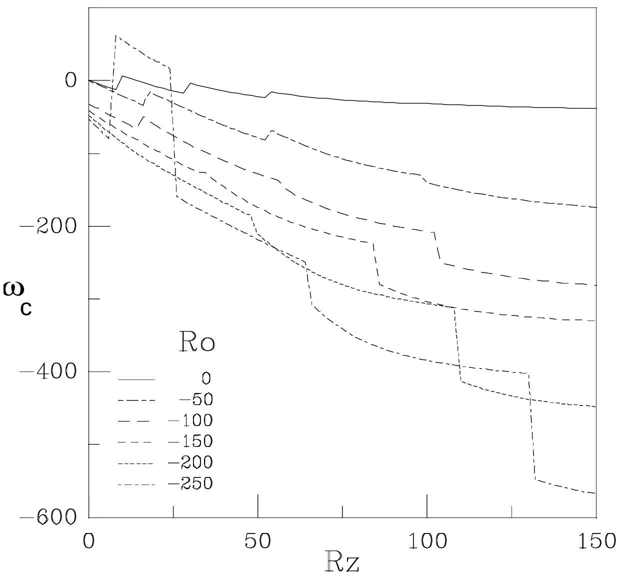

Figure 5.30: Critical parameters for $\eta = 0.5$, as functions of the axial Reynolds number Rz in the counter–rotating case $Ro < 0$. Featured is the imaginary part of the critical eigenvalue ω_c.

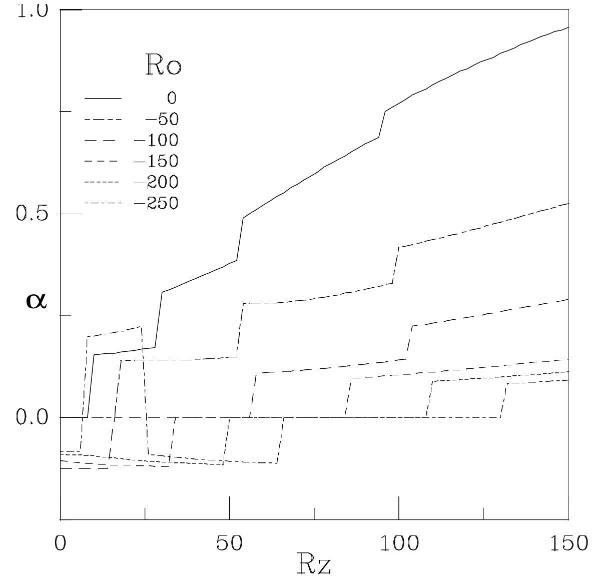

Figure 5.31: Critical parameters for $\eta = 0.5$, as functions of the axial Reynolds number Rz in the counter–rotating case $Ro < 0$. Featured is the angle of the spiral pattern α.

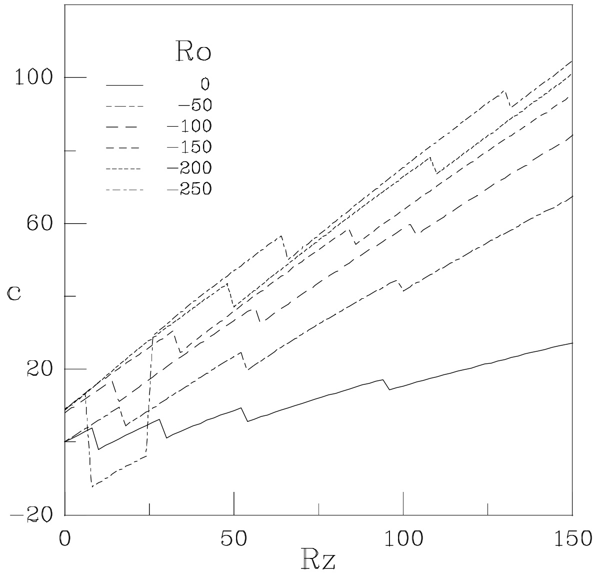

Figure 5.32: Critical parameters for $\eta = 0.5$, as functions of the axial Reynolds number Rz in the counter–rotating case $Ro < 0$. Featured is the axial pattern velocity c.

5.5.1 Sliding Rigid Rotation

In this section, the rigid rotation case $\Omega_i = \Omega_o$ (or, equivalently, $R = Ri = \eta Ro$) is going to be studied with the presence of sliding effects. Actually, it is essential to have a deeper understanding of the dominant instability mechanism in the cusp region. This situation is also important because of its global stability for both limiting cases $Rz = 0$, and $R = 0$. The situation is similar to (Mackrodt, 1976) where it is shown that although the Poiseuille flow in a circular pipe is linearly stable for any Reynolds number, adding a slow rotation of the pipe makes the flow unstable at some finite Reynolds number.

For this particular situation, the general Petrov-Galerkin scheme is used in order to compute the linear stability regimes. Figures 5.33 and 5.34 show the computed critical rotation number $R = Ri = \eta Ro$ and critical wave number k as a function of the axial speed Rz. The critical regime has an asymptotic value as Rz is increased, with the asymptotic rotation Reynolds number $R^{\infty} = 33.24$. In this limit, the critical azimuthal mode is $n = -4$. In addition, as the rotation Reynolds number is increased, the Rz Reynolds number approaches another asymptotic value, which is $Rz^{\infty} = 85.11$, with a critical azimuthal wave number $n = -5$. The dependence of the critical axial wave number k_c over the marginal curve is depicted in figure 5.34. We can observe the presence of a maximum for the values $Rz = 122.05$, $Ri = 50.25$, $k_{max} = 0.7638$. Moreover, the critical wave number k decreases to very low values (less than 0.1) as the axial Reynolds number Rz increases; as a result, the spiral's slope grows.

Therefore, in the co–rotation region, when the inner Reynolds number Ri is increased and before the onset of the centrifugal instability, the solid body rotation zone is experienced. And if the axial sliding Rz is greater than 85.11, shear instability comes into play: the lower part of the cusp appears, becoming the dominant instability mechanism, and

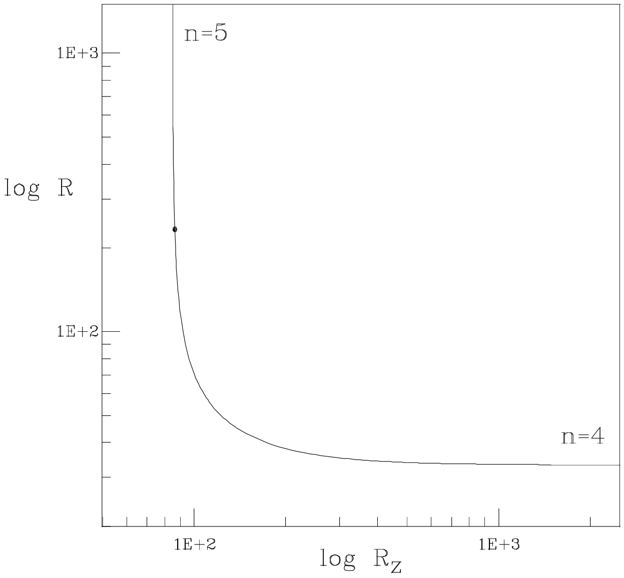

Figure 5.33: Sliding rigid rotation. Critical rotation number $R = Ri = \eta Ro$ as a function of the axial sliding effect. The dominant azimuthal modes are $n = 4$ and $n = 5$, where the dot has been just located at the change state.

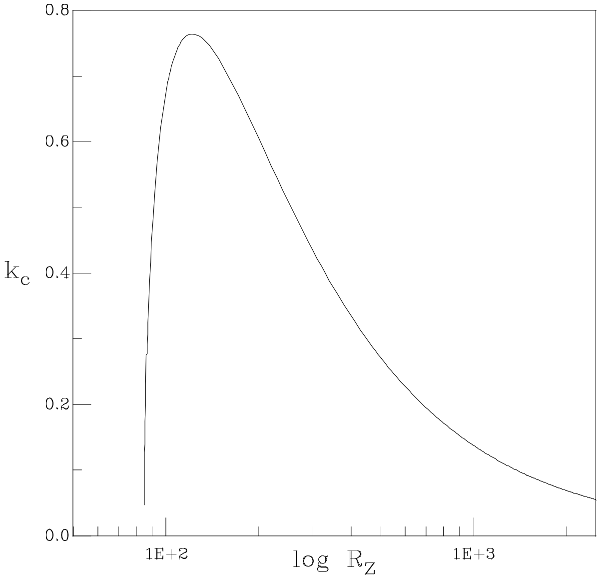

Figure 5.34: Sliding rigid rotation. Critical wave number k as a function of the axial speed Rz for $\eta = 0.5$.

giving a discontinuous critical Reynolds number. The corresponding eigenfunctions are clearly different from the centrifugally dominated ones. The axial wave number k is now very small, giving large spiral angles α, and an almost constant azimuthal wave number n (equal to -4). The cuspidal zone, where the critical surface is multievaluated, corresponds to the competition between the centrifugal instability mechanism (upper branch) and the shear instability mechanism (lower branch), constantly connected by the intermediate sheet. All three branches can be experimentally observed if we fix Ri and steadily increase the axial Reynolds number Rz.

5.6 Instability Results for $\eta = 0.8$

The qualitative features of the critical surface for $\eta = 0.8$ are the same as in the above analyzed $\eta = 0.5$ wide gap case, although quantitative differences do exist. On the one hand, high rhythm change of the n–critical azimuthal modes were observed, as featured in fig. 5.35. The number of azimuthal modes to be considered in the stability analysis increases substantially, and the computation is more expensive.

Figures from 5.36 to 5.47 show the critical parameters Ri_c, ω_c, α and c as functions of Rz and Ro as in the $\eta = 0.5$ case. The critical surface develops a cusp, but for higher positive values of Rz, outside the plotted range. The early stages of the cusp can be seen in figures 5.36, 5.37 and 5.39, where the curves display the same splitting in two different behaviors as in $\eta = 0.5$ case. In figure 5.40 is noted that the slope in the inflexion point tends to become vertical. The shear–instability dominated branch is also very close to the solid body rotation line. Additional numerical results in the region where the cusp is present are be given in section 5.6.1, where a comparison with experimental results is carried out.

The $n = 0$ axisymmetric mode is stabilized by the axial sliding, giving axially traveling Taylor vortices. But now the dominance of the axisymmetric mode is restricted to a very narrow range of Rz values as shown in figures 5.40 ... 5.43. From the numerical results, it can be asserted that the sliding has a global unstabilizing effect on the basic flow. Another curious feature is the presence of a small window of the $n = -3$ critical mode between the regions $n = 2$ and 1 (see figure 5.35). Since this takes place very close to the $Rz = 0$ axis, it is considered as a side effect of the mode competition and switching when the reflexional symmetry $z \to -z$ is broken.

5.6.1 Comparison with Previous Results

Previous experimental studies have been reported on the stability of the Spiral Couette flow. In an excellent work done by Ludwieg in 1964, both theoretical and experimental, a stability analysis was devoted to an specific zone on the parameter space, inside the cusp region. The experimental apparatus has a gap $\eta = 0.8$, with open ends, corresponding to the open flow case. The rotational speed of the external cylinder is held fixed at $Ro \approx 750$.In fact, Ludwieg's experimental device needed high external rotation speeds in order to avoid pre-turbulent stages induced by transients. In addition, the mechanism of increasing axial and azimuthal velocities enforced an implicit dependence between the two

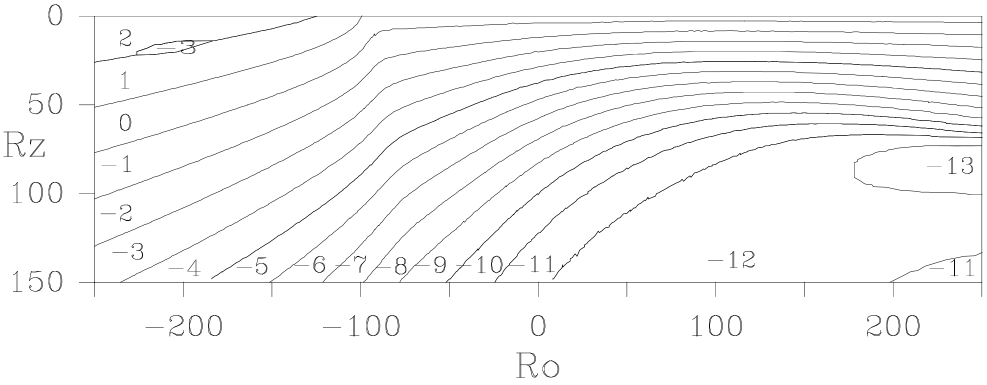

Figure 5.35: Dominant azimuthal mode n at criticality, as a function of Ro, Rz; $\eta = 0.8$.

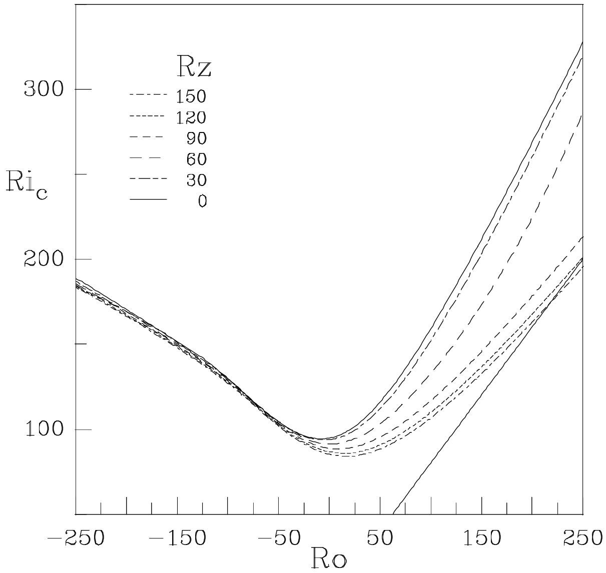

Figure 5.36: Critical parameters for $\eta = 0.8$, as functions of the outer Reynolds number Ro. Featuring critical inner Reynolds number Ri_c; the solid straight line is the rigid rotation line $Ri = \eta Ro$.

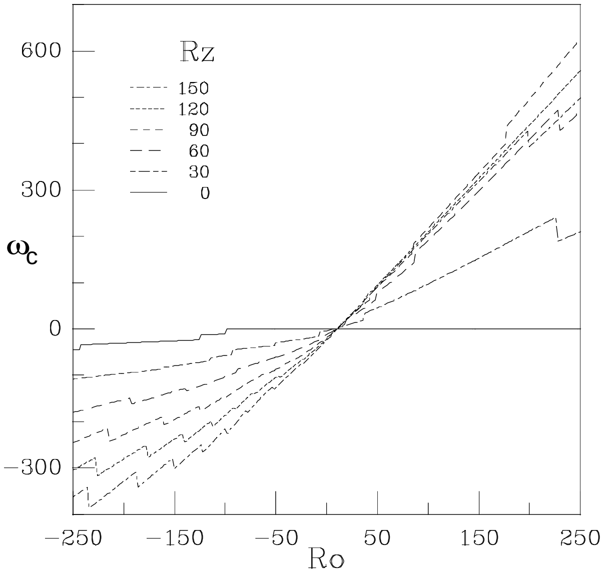

Figure 5.37: Critical parameters for $\eta = 0.8$, as functions of the outer Reynolds number *Ro*. Featuring imaginary part of the critical eigenvalue ω_c.

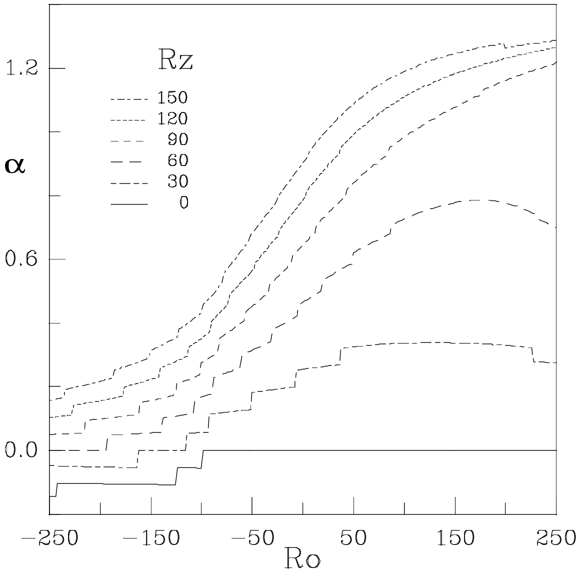

Figure 5.38: Critical parameters for $\eta = 0.8$, as functions of the outer Reynolds number *Ro*. Angle of the spiral pattern α.

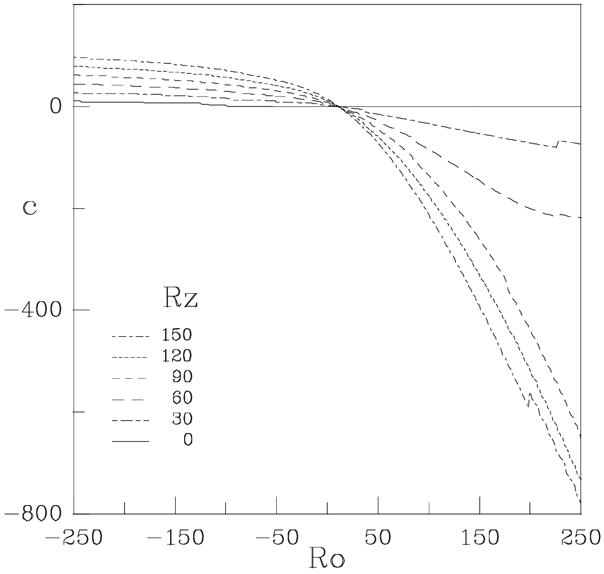

Figure 5.39: Critical parameters for $\eta = 0.8$, as functions of the outer Reynolds number Ro. Featuring axial pattern velocity c.

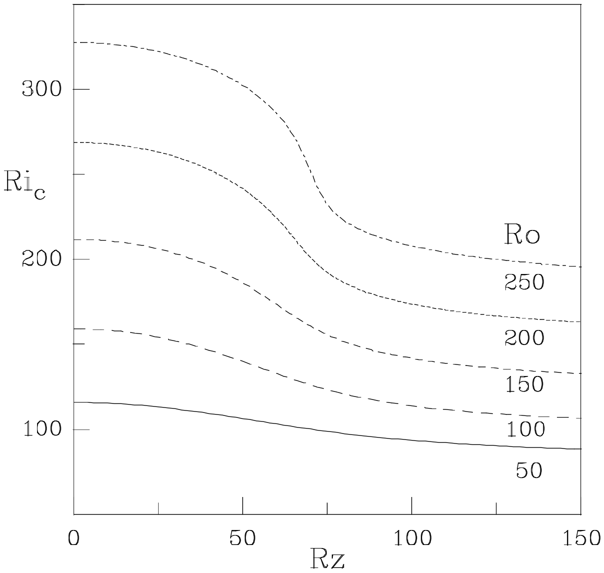

Figure 5.40: Critical parameters for $\eta = 0.8$, as functions of the axial Reynolds number Rz in the co–rotating case $Ro > 0$. Critical inner Reynolds number Ri_c.

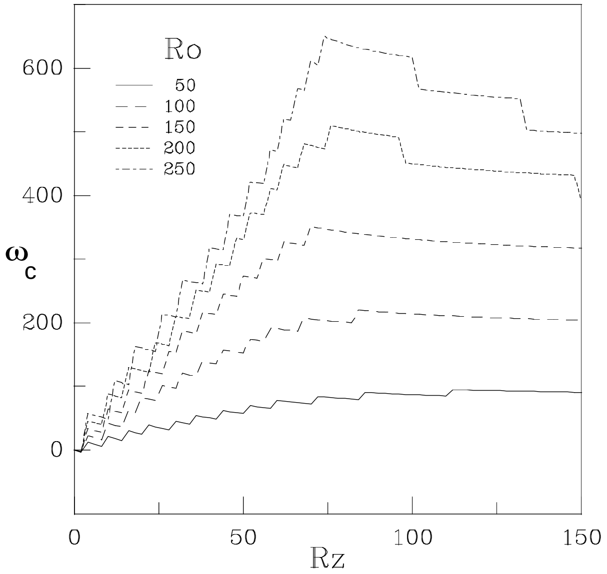

Figure 5.41: Critical parameters for $\eta = 0.8$, as functions of the axial Reynolds number Rz in the co–rotating case $Ro > 0$. Imaginary part of the critical eigenvalue ω_c.

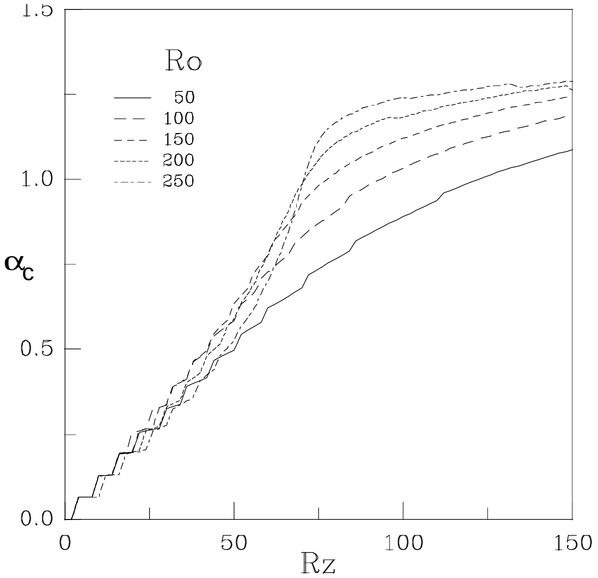

Figure 5.42: Critical parameters for $\eta = 0.8$, as functions of the axial Reynolds number Rz in the co–rotating case $Ro > 0$. Angle of the spiral pattern α.

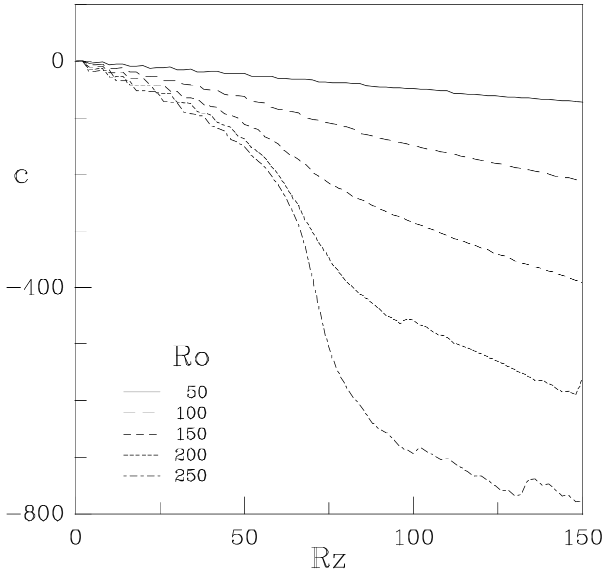

Figure 5.43: Critical parameters for $\eta = 0.8$, as functions of the axial Reynolds number Rz in the co–rotating case $Ro > 0$. Axial pattern velocity c.

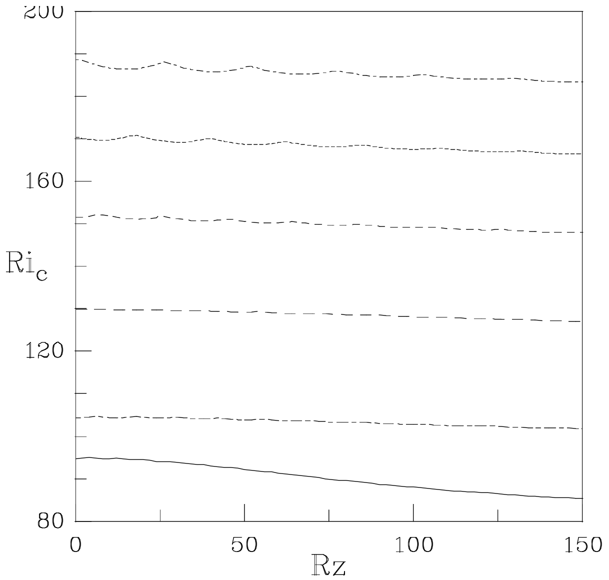

Figure 5.44: Critical parameters for $\eta = 0.8$, as functions of the axial Reynolds number Rz in the counter–rotating case $Ro > 0$. Critical inner Reynolds number Ri_c.

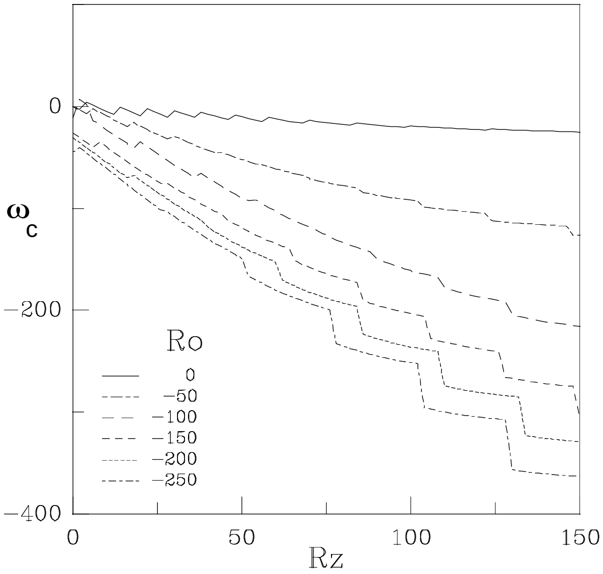

Figure 5.45: Critical parameters for $\eta = 0.8$, as functions of the axial Reynolds number Rz in the counter–rotating case $Ro > 0$. Imaginary part of the critical eigenvalue ω_c.

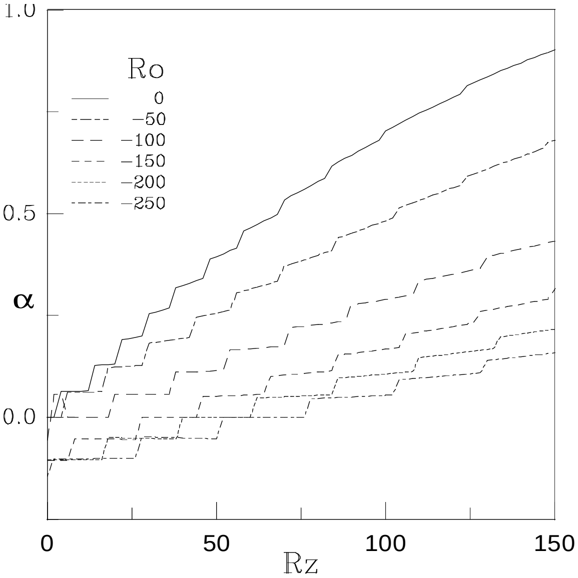

Figure 5.46: Critical parameters for $\eta = 0.8$, as functions of the axial Reynolds number Rz in the co–rotating case $Ro > 0$. Angle of the spiral pattern α.

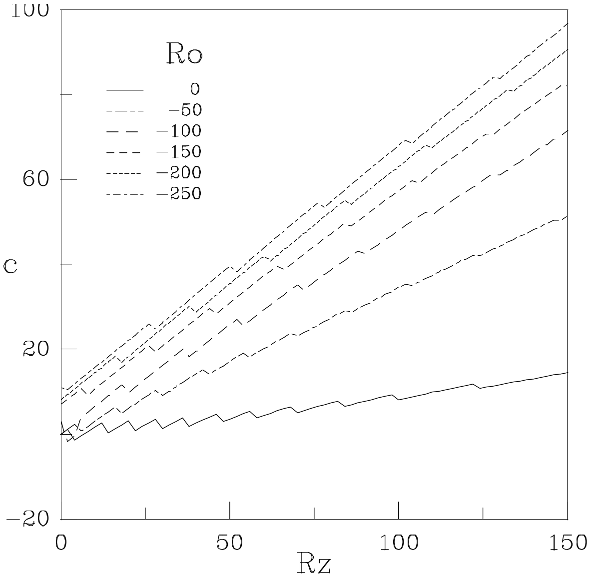

Figure 5.47: Critical parameters for $\eta = 0.8$, as functions of the axial Reynolds number *Rz* in the co–rotating case $Ro > 0$. Axial pattern velocity c.

magnitudes. As a result, the experimental paths in the parameter space (Ri, Rz) were straight lines.

Ludwieg's experimental results (figure 5.8) are given in terms of two nondimensional parameters c_ϕ and c_z, which describe the motion of the fluid. These parameters are functions of the radial variable r,

$$c_\phi(r) = \frac{r}{v_B}\frac{dv_B}{dr}, \quad c_z(r) = \frac{r}{v_B}\frac{dw_B}{dr}, \tag{5.39}$$

where $r_i \le r \le r_o$. In some specific situations, the previous functions suffer only tiny variations in the prescribed range of the values of r, mainly in the narrow gap case. As a consequence, Ludwieg, 1964, considered mean values $\tilde{c}_\phi$ and $\tilde{c}_z$ of these functions as the control parameters; he took $r = (r_i + r_o)/2$, the arithmetic mean radius, in the r factor in front of the definitions of c_z and c_ϕ, but he did not specify which values of the azimuthal and axial velocities and their derivatives were used. In Hung, Joseph & Munson, 1972, the values of $\tilde{c}_\phi$, $\tilde{c}_z$ were used at the geometric mean radius $\bar{r} = \sqrt{r_i r_o}$ to compare with Ludwieg results. As the difference between the arithmetic and geometric means is about 0.6% for the $\eta = 0.8$ case, and moreover, as the expressions of $\tilde{c}_\phi$ and $\tilde{c}_z$ are simpler, using the Hung *et al.* prescription, it is going to be used in the present context (a more detailed discussion of the parameters used by different authors is given in appendix D.5). Assuming the mentioned prescription, the dependence between $\tilde{c}_\phi$, $\tilde{c}_z$ and our variables *Ri*, *Ro*, *Rz* are given by the following equations (for $\eta = 0.8$):

$$\tilde{c}_\phi = \frac{1+\eta}{1-\eta}\frac{Ro - Ri}{Ro + Ri}, \quad \tilde{c}_z = \frac{1+\eta}{1-\eta}\frac{Rz}{Ro + Ri}. \tag{5.40}$$

For the $\eta = 0.8$ case the narrow gap approximation is not clearly justified. In figures 5.49 and 5.50 the variation of the functions $c_z(r)$ and $c_\phi(r)$ is seen to be about 10% with

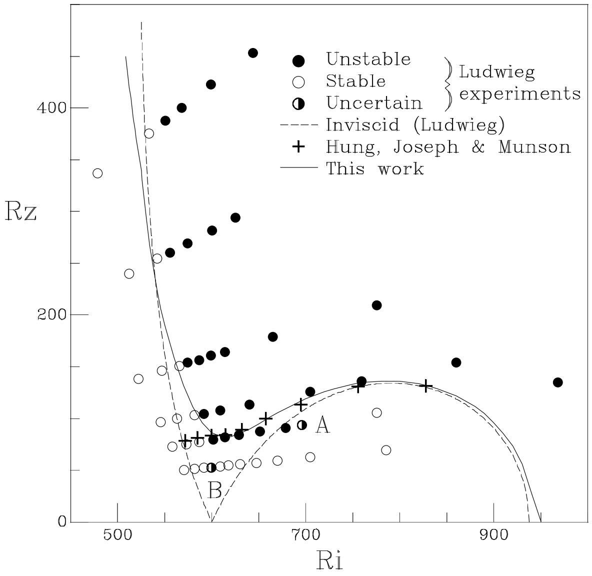

Figure 5.48: Experimental results, from (Ludwieg, 1964) for $\eta = 0.8$ and $Ro = 750$. The results are simultaneously compared with Hung, Joseph & Munson's 1972 former work.

respect to the mean values $\tilde{c}_z$, $\tilde{c}_\phi$. This could be a source of error in the experimental values given by Ludwieg, 1964. It would be necessary to know the original experimental results in terms of the Reynolds numbers in order to work with the *true* control parameters Rz and Ri.

A linear stability analysis of the Spiral Couette problem was reported by Hung, Joseph & Munson, 1972 (from now on cited as HJM), where only particular regions in parameter space where considered. Their results fairly agree with some of Ludwieg's results, although there were some unexplored zones that the present work treats in detail. As a particular case (but out of the range of the global analysis carried out in preceding section), the critical curve for $Ro = 750$ is computed. This curve is single–valued, considering Rz as a function of Ri, but it is well within the cusp region. The global results of the three analyses are sketched in figure 5.48.

Our results are fully coincide with the computations of HJM, except for two points on the left of the minimum of our critical curve in figure 5.48, where those results of HJM clearly diverges from these experimental results. It must be noted that the results of HJM are confined to the intermediate branch of the critical surface fold, where the changes in Rz_c are small. The other branches shows very high slopes of $Rz_c(Ri)$; furthermore, the change in the critical azimuthal wave number n is of more than 15 units in this range. This indicates the difficulties Hung *et al.* encountered out of the intermediate branch, which explains the mentioned discrepancy.

Ludwieg's experimental results exhibit good agreement with the numerical results of this research. The best experimentally defined bifurcation points correspond to the vertical branch (in this case, the shear is the dominant instability mechanism), and on this curve, his discrepancies are less than 4%; it should be mentioned that this is the first time the

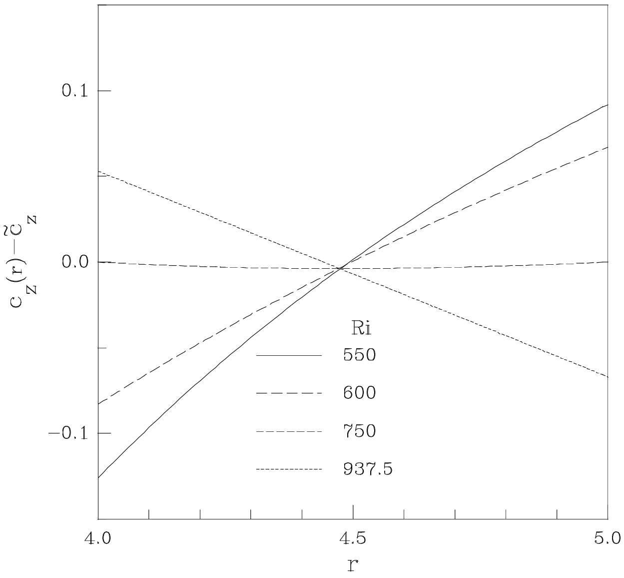

Figure 5.49: Variation of $c_z(r)$ for $\eta = 0.8$ in the gap, compared with the mean value $\tilde{c}_z$; as $c_z(r)$ is linear in Rz, we have plotted it only for the characteristic value $Rz = 100$.

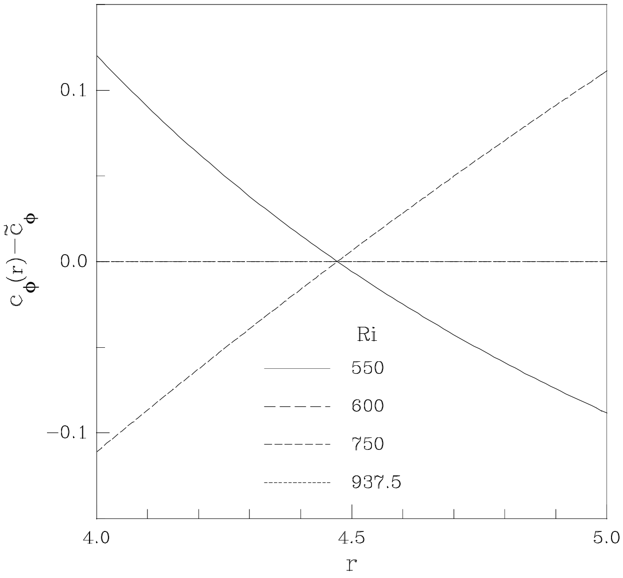

Figure 5.50: Variation of $c_\phi(r)$ for $\eta = 0.8$ in the gap, compared with the mean value $\tilde{c}_\phi$.

vertical branch has been computed numerically. The biggest discrepancy appears for high values of Rz, but for these parameter values, the splitting between the mean values $\tilde{c}_\phi$, $\tilde{c}_z$ and the functions $c_\phi(r)$, $c_z(r)$ has a maximum (see figures 5.49 and 5.50). In the region close to the minimum of the critical curve, the set in of the instability agrees with the experiments, but some points on the right side of the minimum clearly deviates from the numerical predictions. In order to understand why, the experimental setting must be examined closely. In Ludwieg's experiments, a long rod (the inner cylinder) goes through the outer cylinder, with axial movement and simultaneous rotation; the rod accelerates from the rest to the final desired inner rotation and axial velocity. The experiment lasts until the rod has run through the outer cylinder, a short time interval in all cases.

Coming back to figure 5.48, from the two experimental series for low Rz (the two lowest straight lines), it is apparent that to reach the point labeled A, the minimum of the stability curve is crossed when the axial velocity of the rod is increased, so a spiral flow appears before A is reached. Shortly after, when the velocity continues to increase, the basic flow again becomes stable, but the flow is now in the spiral regime, so different situations may arise. If the spiral flow is also stable, the flow will not return to the basic flow; if the bifurcation is subcritical, the spiral flow will persist within the region where the basic flow is stable (hysteresis effect). The spiral flow can also become unstable when the other side of the critical curve (supercritical bifurcation) is crossed, and, in this case, it will also take a finite time for the spiral flow to decay into the basic flow. If this occurs close to the bifurcation point (as it is the case), this asymptotic process can be longer than the the experiment lasts.

All these considerations explains why the experimental points close to A shows a discrepancy with the numerical computations. The experiment should be carried out again using a path in parameter space in such that the (multivalued) critical curve is not crossed, in order to be free of hysteresis and relaxation phenomena. Notice that the points marked with a black and white circle, where Ludwieg could not ascertain about their stability, are very close to the hysteresis region, strongly suggesting that the bifurcation could be subcritical in this parameters range. Ludwieg acknowledged the experimental uncertainties in this parameter region (see figure 5.8) and the estimated errors were shown as a dashed area.

Unfortunately, Ludwieg's experimental data do not include information on the azimuthal wavenumber n, or other critical parameters, as angular velocities, angle of the spiral pattern and axial velocities. Therefore, our comparison is reduced to the analysis of the critical Reynolds number.

Finally, the effectiveness of the inviscid criterion of Ludwieg should be noted, displayed as a dashed line in figure 5.48. The curve follows the behavior of the numerically computed viscous curve qualitatively, and predicts a multievaluated critical surface. The comparison between the inviscid criterion and our computations shows that viscosity stabilizes the flow, delaying the instability, except for high Rz, in the shear–dominated instability region, where the viscosity in fact destabilizes the basic solution, as has been observed in other shear flows.

5.7 Conclusions

In this work, a comprehensive analysis on the effect of axial sliding in the Taylor-Couette Problem has been carried out. Specific and robust numerical methods to deal with the geometrical complexities of the Neutral Stability Curves have been developed. The reliability of the numerical Petrov-Galerlin code has been checked by comparing with Ali and Weidman (93) results, in the enclosed flow case. Detailed computations of the critical surface have been made for two gap values. The wide gap $\eta = 0.5$ case has been considered because the instability appears at lower Reynolds numbers than in the narrow–gap case. The change in the azimuthal wave number is also smaller. The case $\eta = 0.8$ has been considered also, because, as far as could be ascertained, the only experimental data available on this problem correspond to this value. It was found that the sliding has a global unstabilizing effect over the non-axisymmetric modes. By contrast, the $n = 0$ mode keeps stabilized by the same effect, although the range of dominance of this behaviour is quite limited. The bifurcation is mainly to a spiral flow, but travelling Taylor vortices are also observed in small parameter ranges.

Notable differences can be pointed out between the co-rotation and counter-rotation zones. Counter-rotation configurations exhibit a regular behaviour in the critical regime. Nevertheless, the sudden dominance of non-consecutive azimuthal modes for low Rz values is to be noted. This phenomenon is due to the breaking of the reflexional symmetry $z \to -z$, which leads to mode competition and switching between $\pm n$ modes.

The critical behaviour is radically different in the co-rotation zone. The critical surface $Ri_c = f(Rz, Ro)$ exhibits zero-th order discontinuities, which can only be detected making use of the specific numerical scheme for the computation of the neutral stability curves. The discontinuity is due to the presence of a sudden dominant island corresponding to a different azimuthal mode. This unusual phenomena in hydrodynamical stability problems has been explained in terms of competition between two independent instability mechanisms: centrifugal instability, dominant in the counter–rotating regime and also for small axial sliding; and the shear instability due to the axial motion. This second mechanism becomes dominant near the solid body rotation line, substantially lowering the onset of the instability. The discontinuity of the critical surface is related to the competition between both modes; the critical surface is folded into a cusp, and hysteresis behavior becomes possible. The eigenfunctions corresponding to each mechanism are clearly different: spirals with large angles correspond to shear–type eigenfunctions and show little variation of the azimuthal wave number n, while those corresponding to the centrifugal instability exhibit small angles and large variations of n. The computations in this research compare very favorable with the previous computations of Hung, Joseph and Munson (72), who obtained one of the branches in the fold region. Agreement with the experimental results of Ludwieg (64) is also very good. In spite of the difficulties encountered with the parameters defined by Ludwieg, the agreement in the shear–dominated branch, computed for the first time, is better than 4%.

In order to accurately measure the bifurcation point in the region where hysteresis is present, new experiments would be necessary, trying to avoid the unwanted crossings of the critical surface, and designing a parameter path far from the tangencies exhibited by the lower experimental series of Ludwieg in figure 5.48. These experiments could also supply additional information on other computed critical parameters.

Chapter 6

Weak Nonlinear Analysis of the Taylor-Couette Problem: Petrov-Galerkin approach

6.1 Introduction

As was briefly commented in chapter one, ds theories have provided a wide assortment of methodologies for studying the nonlinear behaviour of a fluid system near critical stages. The formal approach to this problem lies on the mathematical hypotheses used to obtain the reduced or simplified model of amplitudes which leads the perturbations just after the bifurcation has taken place. At this stage, two main alternatives may be chosen. The first, under the hypothesis of continuous spectrum of eigenvalues (extended systems), space modulation of the perturbation amplitude may be assumed. This approach is usually termed Ginzburg-Landau method, and its effectiveness has been extensively checked in many continuous systems recently. Nevertheless, it should be pointed out that, so far, a formal conclusion has not been provided which could theoretically justify the time-space scale analysis used to obtain the Ginzburg-Landau amplitude equation. As a matter of fact, the method must be suitably modified in each particular case (Cross & Hohenberg, 1993). The second, under the hypothesis of discrete spectrum of eigenvalues, more formal methodologies are available.

Center manifold theory and normal forms provide a fair explanation of what is really happening after the system goes through a bifurcation. Of course, the reliability of the results is strongly conditioned whether the analysis is done near criticality or not. In either case, from a mathematical point of view, the amplitude equations obtained from this method are completely formal and general. The hypothesis of discrete spectrum of eigenvalues is now the main point to be discussed. Under some physical conditions, periodicity in the extended coordinates may be always assumed. This is, of course, an idealization of the original problem, because there are not infinite experimental systems. Nevertheless, it is a well known fact that extended systems exhibit pattern formation with a clear periodicity which is only modulated after a long transient period of time. Moreover, the information obtained from the center manifold models, condense the whole mechanism of instabilities along with their original nature.

The present chapter deals with the nonlinear stability analysis of the Taylor-Couette problem under some specific conditions. A methodology to apply Petrov-Galerkin schemes to obtain the first order coefficients of the amplitude equations will be developed. This part considers two particular situations. On the one hand, the steady bifurcation case without sliding effects will be studied. In this case, O(2) symmetry will be considered. On the other hand, the explicit symmetry breaking O(2)→SO(2) due to the presence of a the combination of relative sliding and imposed axial pressure gradient effects (*Couette-Poiseuille flow*). In fact, steady bifurcations are going to be sought in the last case. Our aim is to evidence numerically the predictions done by the normal form analysis of the bifurcation. In both situations, only the system of equations to be solved numerically will be obtained. The explicit numerical computation of the proposed systems is out of the scope of the present task.

6.2 Steady Bifurcations with O(2)–symmetry.

In this part, the classical Taylor-Couette problem will be considered. Consequently, no axial effects will take place in the dynamics of the system. Under this prescription, O(2)×SO(2) symmetries must be considered in order to simplify the analysis. First, consider the nonlinear partial differential equation corresponding to the perturbation field

$$\partial_t \mathbf{v} = \Delta \mathbf{v} - (\mathbf{v}^B \cdot \nabla)\mathbf{v} - (\mathbf{v} \cdot \nabla)\mathbf{v}^B - (\mathbf{v} \cdot \nabla)\mathbf{v} - \nabla p. \tag{6.1}$$

For the sake of simplicity, $\mathbf{v}^B$ will stand for the steady Couette flow with zero external rotation $R_o = 0$[1]

$$\mathbf{v}^B(r) = \begin{pmatrix} 0 \\ R_i \Theta(r) \\ 0 \end{pmatrix}, \tag{6.2}$$

where $\Theta(r)$ stands for the radial dependence of the laminar *Couette flow* under the prescribed boundary conditions

$$\Theta(r) \doteq \frac{\eta R_i}{1+\eta}\left[\frac{1}{r(1-\eta)^2} - r\right], \tag{6.3}$$

where $r \in [\frac{\eta}{1-\eta}, \frac{1}{1-\eta}]$. The critical stage is accomplished by increasing the rotation speed of the inner cylinder (i.e. the R_i control parameter) so that there are some eigenvalues of the linear analysis crossing the imaginary axis for some specific value $R_i = R_i^c$. In fact, due to axial symmetry, it can be proved that the crossing eigenvalue must be at least double (Chossat & Iooss, 1994). In the framework of center manifold theory, a slight increase of the R_i parameter is considered $R_i = R_i^c + \mu$, where $0 < \mu << 1$. For the axisymmetric case $n = 0$, the linear stability analysis provides the eigenfunctions associated with the critical eigenvalues which are crossing the imaginary axis:

$$\zeta_0(r,z) = \mathrm{e}^{\mathrm{i}k_c z} U_0(r) \quad \bar{\zeta}_0(r,z) = \mathrm{e}^{-\mathrm{i}k_c z} U_0(r) \tag{6.4}$$

---

[1] Nevertheless, the general case with rotation of the outer cylinder can be solved in the same way.

At the critical stage ($\mu = 0$), the asymptotic behavior of the perturbations remains led by the center variables x_c corresponding to the previous eigenfunctions

$$x_c(t) = A(t)\zeta_0(r,z) + \bar{A}(t)\bar{\zeta_0}(r,z). \tag{6.5}$$

In addition, the stable hyperbolic modes $x_h(t)$ will be slaved throughout the center manifold

$$x_h(t) = \sum_{p+q+r\geq 2} \phi_{pqr}(r,z)\mu^p A^p \bar{A}^q. \tag{6.6}$$

Consequently, the perturbation $\mathbf{v}(r,z,t)$ can be split up as follows

$$\mathbf{v}(r,z,t) = x_c(t) + x_h(t). \tag{6.7}$$

The same decoupling may be done for the pressure gradient field, where its hyperbolic part can be now expressed as a Taylor expansion of gradient fields

$$\nabla p = \sum_{p+q+r\geq 2} \nabla\tilde{\phi}_{pqr}(r,z)\mu^p A^p \bar{A}^q. \tag{6.8}$$

However, the previous terms will not be considered in the computational Petrov-Galerkin scheme as they vanish under the projection procedure.

The third order normal form corresponding to a steady bifurcation with O(2)-symmetry is (Iooss & Adelmeyer, 1992)

$$\frac{dA}{dt} = d\mu A + bA|A|^2, \tag{6.9}$$

where d and b are real coefficients which must be computed numerically. Formal substitution of the splitting (6.7) in the nonlinear perturbation equation (6.1)

$$\frac{d}{dt}(x_c + x_h) = [\Delta - \mathbf{v}^B \cdot \nabla](x_c + x_h) - [(x_c + x_h)\cdot\nabla](\mathbf{v}^B + x_c + x_h) - \nabla p, \tag{6.10}$$

where now the basic flow has been slightly perturbed above the critical stage

$$\mathbf{v}^B(r) = (R_i^c + \mu)\begin{pmatrix} 0 \\ \Theta(r) \\ 0 \end{pmatrix}. \tag{6.11}$$

Formal substitution of center manifold expansion $x_c(t)$ from (6.7) in (6.10) and neglecting terms with order higher than the third, a hierarchy of boundary eigenvalue problems is obtained by direct identification of power orders. This is accomplished by introducing normal form (6.9) in (6.10). Then, on identifying equally powered terms in Taylor's expansion of the form $\mu^p A^q |A|^r$, the following system of equation is obtained:

order μA:

$$\Delta\phi_{110} - [\begin{pmatrix} 0 \\ R_i \\ 0 \end{pmatrix}\cdot\nabla]\phi_{110} - R_i^c[\phi_{110}\cdot\nabla]\begin{pmatrix} 0 \\ \Theta \\ 0 \end{pmatrix} - \nabla\tilde{\phi}_{110} =$$

$$[\begin{pmatrix} 0 \\ \Theta \\ 0 \end{pmatrix}\cdot\nabla]\zeta_0 + [\zeta_0\cdot\nabla]\begin{pmatrix} 0 \\ \Theta \\ 0 \end{pmatrix} + d\zeta_0, \tag{6.12}$$

order $\mu\bar{A}$:

$$\Delta\phi_{101} - [\begin{pmatrix} 0 \\ R_i \\ 0 \end{pmatrix} \cdot \nabla]\phi_{101} - R_i^c[\phi_{101}\cdot\nabla]\begin{pmatrix} 0 \\ \Theta \\ 0 \end{pmatrix} - \nabla\tilde{\phi}_{101} = [\begin{pmatrix} 0 \\ \Theta \\ 0 \end{pmatrix}\cdot\nabla]\bar{\zeta}_0 + [\bar{\zeta}_0\cdot\nabla]\begin{pmatrix} 0 \\ \Theta \\ 0 \end{pmatrix} + d\bar{\zeta}_0, \tag{6.13}$$

order μA^2:

$$\Delta\phi_{020} - [\begin{pmatrix} 0 \\ R_i^c\Theta \\ 0 \end{pmatrix}\cdot\nabla]\phi_{020} - R_i^c[\phi_{020}\cdot\nabla]\begin{pmatrix} 0 \\ \Theta \\ 0 \end{pmatrix} - [\zeta_0\cdot\nabla]\zeta_0 - \nabla\tilde{\phi}_{020} = 0, \tag{6.14}$$

order $\mu\bar{A}^2$:

$$\Delta\phi_{002} - [\begin{pmatrix} 0 \\ R_i^c\Theta \\ 0 \end{pmatrix}\cdot\nabla]\phi_{002} - R_i^c[\phi_{002}\cdot\nabla]\begin{pmatrix} 0 \\ \Theta \\ 0 \end{pmatrix} - [\bar{\zeta}_0\cdot\nabla]\bar{\zeta}_0 - \nabla\tilde{\phi}_{002} = 0, \tag{6.15}$$

order $\mu A\bar{A}$:

$$\Delta\phi_{011} - [\begin{pmatrix} 0 \\ R_i^c\Theta \\ 0 \end{pmatrix}\cdot\nabla]\phi_{011} - R_i^c[\phi_{011}\cdot\nabla]\begin{pmatrix} 0 \\ \Theta \\ 0 \end{pmatrix} = [\zeta_0\cdot\nabla]\bar{\zeta}_0 + [\bar{\zeta}_0\cdot\nabla]\zeta_0 + \nabla\tilde{\phi}_{011}, \tag{6.16}$$

order $\mu A|A|^2$:

$$\Delta\phi_{021} - [\begin{pmatrix} 0 \\ R_i^c\Theta \\ 0 \end{pmatrix}\cdot\nabla]\phi_{021} - R_i^c[\phi_{021}\cdot\nabla]\begin{pmatrix} 0 \\ \Theta \\ 0 \end{pmatrix} - \nabla\tilde{\phi}_{021} = b\zeta_0 + [\zeta_0\cdot\nabla]\phi_{011} + [\bar{\zeta}_0\cdot\nabla]\phi_{020} + [\phi_{011}\cdot\nabla]\zeta_0 + [\phi_{020}\cdot\nabla]\bar{\zeta}_0, \tag{6.17}$$

order $\mu\bar{A}|A|^2$:

$$\Delta\phi_{012} - [\begin{pmatrix} 0 \\ R_i^c\Theta \\ 0 \end{pmatrix}\cdot\nabla]\phi_{012} - R_i^c[\phi_{012}\cdot\nabla]\begin{pmatrix} 0 \\ \Theta \\ 0 \end{pmatrix} - \nabla\tilde{\phi}_{012} = b\bar{\zeta}_0 + [\zeta_0\cdot\nabla]\phi_{002} + [\bar{\zeta}_0\cdot\nabla]\phi_{011} + [\phi_{002}\cdot\nabla]\zeta_0 + [\phi_{011}\cdot\nabla]\bar{\zeta}_0, \tag{6.18}$$

order μA^3:

$$\Delta\phi_{030} - [\begin{pmatrix} 0 \\ R_i^c\Theta \\ 0 \end{pmatrix}\cdot\nabla]\phi_{030} - R_i^c[\phi_{030}\cdot\nabla]\begin{pmatrix} 0 \\ \Theta \\ 0 \end{pmatrix} = [\zeta_0\cdot\nabla]\phi_{020} + [\phi_{020}\cdot\nabla]\zeta_0 + \nabla\tilde{\phi}_{030}, \tag{6.19}$$

order $\mu\bar{A}^3$:

$$\Delta\phi_{003}-[\begin{pmatrix}0\\ R_i^c\Theta\\ 0\end{pmatrix}\cdot\nabla]\phi_{003}-R_i^c[\phi_{003}\cdot\nabla]\begin{pmatrix}0\\ \Theta\\ 0\end{pmatrix}=$$
$$[\bar{\zeta}_0\cdot\nabla]\phi_{020}-[\phi_{020}\cdot\nabla]\bar{\zeta}_0-\nabla\tilde{\phi}_{030}. \qquad (6.20)$$

At the same time, it should be regarded that the sought functions ϕ_{pqr} must satisfy the free-divergence condition

$$\nabla\cdot\phi_{pqr}=0, \quad \forall p,q,r\in\mathbb{N} \qquad (6.21)$$

and

$$\phi_{pqr}(\frac{\eta}{1-\eta})=\phi_{pqr}(\frac{1}{1-\eta})=0, \quad \forall p,q,r\in\mathbb{N}\ , \qquad (6.22)$$

–that is, they vanish over the radial boundaries.

6.3 Computation of *d* and *b*. Fredholm Alternative

The present section deals with the mathematical problem of computation of coefficients d and b of the normal form equation (6.9). Only the Petrov-Galerkin methodology and final expressions will be provided here, the explicit computation being out of the scope of this work. This latter task would require, in some parts of the general procedure, the use of a algebraic manipulator (Rand & Armbruster, 1987).

First, consider the equation (6.12), which contains the sought coefficient d. From the linear stability analysis, an advantage can be drawn from the fact that ζ_0 is a 0−eigenfunction. In other words

$$\Delta\zeta_0-R_i^c[\begin{pmatrix}0\\ \Theta\\ 0\end{pmatrix}\cdot\nabla]\zeta_0-R_i^c[\zeta_0\cdot\nabla]\begin{pmatrix}0\\ \Theta\\ 0\end{pmatrix}=0\zeta_0 \qquad (6.23)$$

or, symbolically

$$M_{R_i^c}\zeta_0=0. \qquad (6.24)$$

As a result, the operator $M_{R_i^c}$ is not invertible. On note that now, the equation (6.12) for ϕ_{110} can be expressed as follows

$$M_{R_i^c}\phi_{110}=d\zeta_0+[\begin{pmatrix}0\\ \Theta\\ 0\end{pmatrix}\cdot\nabla]\zeta_0+[\zeta_0\cdot\nabla]\begin{pmatrix}0\\ \Theta\\ 0\end{pmatrix}+\nabla\tilde{\phi}_{110}. \qquad (6.25)$$

Regarding the no-invertibility of the operator acting over ϕ_{110}, a compatibility condition is needed to solve the boundary problem (6.25). For this purpose, the usually termed *Fredholm alternative* or *compatibility condition* is used. This is stated by the following theorem:

Theorem 6.3.1 (Fredholm alternative) *The boundary value problem (6.25) is compatible iff the right hand side term is orthogonal to* ζ_0*, which is the solution to the associated homogeneous boundary value problem (6.23).*

Consequently, the Fredholm alternative enforces the following condition to be satisfied

$$< \zeta_0, d\zeta_0 + [\begin{pmatrix} 0 \\ \Theta \\ 0 \end{pmatrix} \cdot \nabla]\zeta_0 + [\zeta_0 \cdot \nabla]\begin{pmatrix} 0 \\ \Theta \\ 0 \end{pmatrix} + \nabla\tilde{\phi}_{110} >= 0. \qquad (6.26)$$

In previous equation, the inner product $<,>$ must be understood in the sense of $\mathcal{L}^2[0, 2\pi/k_c] \times [0, 2\pi] \times [\eta/(1-\eta), 1/(1-\eta)]$-integrable vector fields. At this stage, Petrov-Galerkin schemes may play a useful role. First, the computed spectral eigenfunctions obtained from the linear analysis problem may be used. This greatly simplifies the computation of d because of the pressure gradient $\tilde{\phi}_{110}$ term cancellation in the projection. Denote by ζ_0^M, the $M^{th}-$order spectral eigenfuction corresponding to the discretization problem introduced in previous chapter

$$\zeta_0^M = \mathrm{e}^{\mathrm{i}k_0 z} U_0^M(r), \qquad (6.27)$$

where k_0 is the numerical approximation of k_c. Then, a fair approximation of the coefficient b is given by the following relation

$$d = -\frac{< U_0^M(r), [\begin{pmatrix} 0 \\ \Theta \\ 0 \end{pmatrix} \cdot \nabla]U_0^M(r) > + < U_0^M(r), [U_0^M(r) \cdot \nabla]\begin{pmatrix} 0 \\ \Theta \\ 0 \end{pmatrix} >}{< U_0^M(r), U_0^M(r) >} \qquad (6.28)$$

For the computation of the second coefficient b, the same procedure must be done. In this case, equation (6.17) may be written as follows

$$M_{R_i^c}\phi_{021} = b\zeta_0 + [\zeta_0 \cdot \nabla]\phi_{011} + [\bar{\zeta}_0 \cdot \nabla]\phi_{020} + [\phi_{011} \cdot \nabla]\zeta_0 + [\phi_{020} \cdot \nabla]\bar{\zeta}_0 + \tilde{\phi}_{021}, \qquad (6.29)$$

which, again, is not invertible. The compatibility condition is now

$$< \zeta_0, b\zeta_0 + [\zeta_0 \cdot \nabla]\phi_{011} + [\bar{\zeta}_0 \cdot \nabla]\phi_{020} + [\phi_{011} \cdot \nabla]\zeta_0 + [\phi_{020} \cdot \nabla]\bar{\zeta}_0 + \tilde{\phi}_{021} > . \qquad (6.30)$$

On note that now, the compatibility condition (6.30) includes the functions ϕ_{011} and ϕ_{020}, which must be computed numerically from equations (6.16) and (6.14), respectively. Altogether, the computation of the center manifold and the coefficients is a really *tour de force*. Equation (6.30) can be again suitably modified for the Petrov-Galerkin scheme. Thus, a fair approximation of b is given by the following equation

$$b = -\frac{< U_0^M(r), [\zeta_0 \cdot \nabla]\phi_{011}^M + [\bar{\zeta}_0 \cdot \nabla]\phi_{020}^M + [\phi_{011}^M \cdot \nabla]\zeta_0 + [\phi_{020}^M \cdot \nabla]\bar{\zeta}_0 >}{< U_0^M(r), U_0^M(r) >}, \qquad (6.31)$$

where ϕ_{011}^M and ϕ_{020}^M are the $M-$order spectral solutions corresponding to the homogeneous boundary problems (6.16) and (6.14), respectively.

6.4 O(2)→SO(2) Symmetry Breaking

This final section deals with of stationary bifurcations with an $\mathsf{O}(2)$ broken symmetry. At the present stage, it should be noted that the symmetry may be broken in two different ways. First, the bifurcation may break the symmetry by appearing structures which are not invariant under specular axial reflections or axial fixed-period translations. This is the case of spirals, for example, in Taylor-Couette problem, where a time-periodic pattern appears. Secondly, $\mathsf{O}(2)$ symmetry may be broken explicitly by introducing axial effects on the problem. The present section will only consider the combined axial sliding and imposed axial pressure gradient effects. Moreover, the analysis will be done under the hypothesis of stationary outer rotation.

The main goal is to find a generic bifurcation capable of providing stationary supercritical patterns. For this reason, the double-zero eigenvalue bifurcation eigenvalue will be considered. Consequently, two different alternatives are available for the Jordan form of the operator

$$L_1 = \begin{pmatrix} 0 & 0 \\ 1 & 0 \end{pmatrix}, \text{or} \quad L_2 = \begin{pmatrix} 0 & 0 \\ 0 & 0 \end{pmatrix}. \tag{6.32}$$

At this point, the non trivial $\mathsf{SO}(2)$ action group is considered over the two alternatives. This will be accomplished by introducing the exponential map

$$R_\phi = \begin{pmatrix} \mathrm{e}^{\mathrm{i}m\phi} & 0 \\ 0 & \mathrm{e}^{-\mathrm{i}m\phi} \end{pmatrix}, \quad m \neq 0, \tag{6.33}$$

which acts non-trivially over the two-dimensional zero-eigenspace. In order to identify which of them represent properly the bifurcation, the commutation relations $[R_\phi, L_1] = 0$ and $[R_\phi, L_2] = 0$ must be imposed. As a result, only the second alternative L_2 satisfies the equivariance property.

The computation of the normal form bifurcation equation is now accomplished by considering the complex representation

$$\begin{aligned} \dot{A} &= P(A, \bar{A}, \alpha) \\ \dot{\bar{A}} &= \overline{P(A, \bar{A}, \alpha)}, \end{aligned} \tag{6.34}$$

where P is a complex polynomial depending on second or higher order terms $A^p \bar{A}^q$ and on a set of parameters α featuring the $\mathsf{O}(2)$ symmetry breaking. The leading terms of P will be obtained by imposing the $\mathsf{SO}(2)$ symmetry condition

$$\mathrm{e}^{\mathrm{i}m\phi} P(A, \bar{A}, \alpha) = P(\mathrm{e}^{\mathrm{i}m\phi} A, \mathrm{e}^{-\mathrm{i}m\phi} \bar{A}, \alpha). \tag{6.35}$$

From last equation, the algebraic structure of P may be obtained

$$P(A, \bar{A}, \alpha) = A f(|A|^2, \alpha) \tag{6.36}$$

Equation (6.34) can be now expressed in its polar or Euler form by the identification $A = r\mathrm{e}^{\mathrm{i}\theta}$

$$\dot{r} = r(\mathrm{Re}[\alpha] + \mathrm{Re}[a] r^2 + \cdots) \tag{6.37}$$

$$\dot{\theta} = \mathrm{Im}[\alpha] + \mathrm{Im}[a] r^2 + \cdots . \tag{6.38}$$

Therefore, the third order polar normal form is

$$\dot{r} = r(\mu + cr^2) \tag{6.39}$$
$$\dot{\theta} = \nu + dr^2 \tag{6.40}$$

where μ and ν will now represent the unfolding parameters of the bifurcation. Therefore, the bifurcation is of codimension 2. The last equations can now be written in the classical complex form

$$\dot{A} = A(\mu + \mathrm{i}\nu + [c + \mathrm{i}d]|A|^2) \tag{6.41}$$

Stationary solutions of (6.40) and (6.40) are obtained from the conditions $\dot{r} = 0$ and $\dot{\theta} = 0$. As a result, two different kind of steady patterns may be appear. On the one hand, the trivial (unstable) *Couette-Poiseuille flow* corresponding to $r = 0$ is always a solution. On the other hand, provided that $c \neq 0$, two branches of stable solutions appear

$$\rho(\mu) = \pm\sqrt{-\frac{\mu}{c}}. \tag{6.42}$$

The phase $\theta-$dynamics is crucial at this point. The second condition $\dot{\theta} = 0$ establishes a linear dependence between the two parameters μ and ν over the bifurcation branches $\rho(\mu)$

$$\nu_\rho = \frac{d}{c}\mu \tag{6.43}$$

Consequently, the steady bifurcated solutions $(\sqrt{\mu/c}, \theta_0)$ would lie on a circle with a constant phase. This is a continuous family of Taylor vortices, distinguished by an axial phase shift. As was predicted by Armbruster and Mahalov, a suitable combination of imposed axial effects would lead to this kind of behaviour (Armbruster & Mahalov, 1992).

Finally, for the specific computation of the coefficients d and c, the center manifold formalism should be applied in the same way that it was carried out in the previous section. Nevertheless, the linear regime provides enough information about the qualitative character of the bifurcation. For the present, we will restrict our analysis to the search of numerical evidences capable of confirming the theoretical predictions obtained from the normal form analysis.

6.5 Numerical Evidences

In order to confirm the theoretical predictions obtained in the previous section, a Petrov-Galerkin scheme has been specially constructed for the simultaneous combination of the axial sliding and imposed axial pressure gradient case. Thus, the Taylor-Couette problem is here considered with the simultaneous effects of rotation of the inner cylinder R_i, inner axial sliding R_z and axial pressure gradient $\hat{\Pi}$ (*Couette-Poiseuille flow*, see Joseph, 1976). In this specific situation, the basic flow is given by the expression

$$\mathbf{v}^B(r) = \begin{pmatrix} 0 \\ R_i\Theta(r) \\ R_zZ_S(r) + \hat{\Pi}Z_P(r) \end{pmatrix}, \tag{6.44}$$

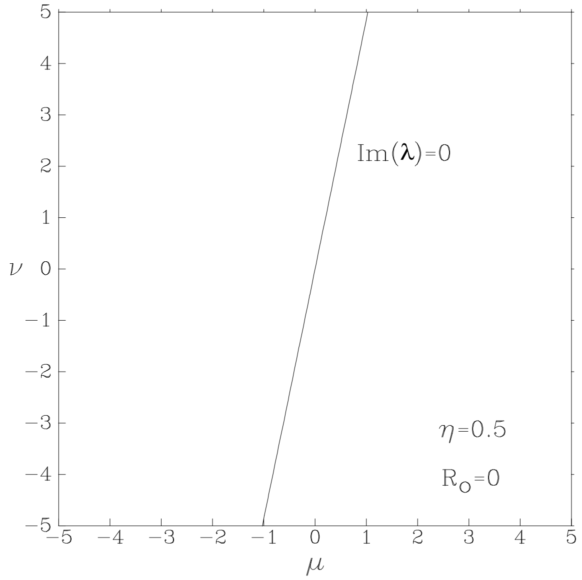

Figure 6.1: Featuring zero-level curve of the imaginary part ω corresponding to the critical eigenvalue as a function of the parameters $\mu = Rz$-sliding effect and $\nu = P$-axial pressure gradient. Petrov-Galerkin methods have been used in order to obtain the previous results. On note the linear dependence between the parameters of the codimension-2 bifurcation.

where Z_S and Z_P stand for the radial dependence of the axial basic flow corresponding to the sliding and imposed pressure effects respectively. They are explicitly given by the following expressions

$$Z_S(r) = \frac{\ln r(1-\eta)}{\ln \eta} \tag{6.45}$$

$$Z_P(r) = \frac{1}{4}[\frac{\delta}{\ln \eta} \ln r(1-\eta) - r^2 - \frac{1}{(1-\eta)^2}]. \tag{6.46}$$

Symmetry breaking will be accomplished by considering R_z and $\hat{\Pi}$ as the parameters μ and ν. Therefore, the analysis will be done for values near zero. A linear stability analysis, as in the previous chapter can be done. In this case, the main interest lies on the axisymmetric disturbances and their dominance for moderate values of $R_z = \mu$ and $\hat{\Pi} = \nu$. In addition, efforts must be focused on the search for steady secondary flows, that is, zero imaginary part of the bifurcating eigenvalues.

The main results are condensed in figure 6.1, where the curve of zero imaginary part of the bifurcating eigenvalue is represented as function of the symmetry breaking parameters μ and ν. As expected from the theoretical results obtained in the previous section, the dependence between the axial sliding and the imposed pressure gradient must be linear. The computations have been done for the $\eta = 0.5$ wide gap case.

Chapter 7

Conclusions

7.1 Main Results

In the present work, the reliability of the Petrov-Galerkin schemes applied to nonlinear fluid dynamical systems is confirmed extensively. Furthermore, their simplicity and easy implementation make the whole formalism a powerful tool in different kinds of problems. In chapter 3, focus was on the search for a link between dynamical systems theory and Navier-Stokes equations in order to provide essential information about the stability of two dimensional fluid flows. Although the computational cost of the numerical method may be greater than other standard method of integration (Shen, 1992), the final results are more reliable from the point of view of hydrodynamic stability. As a matter of fact, the instability results provided for the Regularized Driven Cavity Flow improve former ones obtained by Shen with a notable reduction of the relative error in the computation of the critical Reynolds number.

In chapter 4, the relevance of low-dimensional fluid models was pointed out as a fair explanation of turbulent phenomena. Furthermore, special numerical algorithms for the analysis of time multi-periodic dynamical systems was developed. Those methods can compute with high accuracy period-doubling points of bifurcations, detecting not only stable periodic orbits but also unstable ones, which are in fact the cause of the eventual transition to chaotic regimes. Beyond the multi-periodic stages, where Floquet analysis has been extensively applied, specific numerical algorithms for the long time evolution were constructed. This was done in order to compute Liapunov exponents, using the method of Shimada & Nagashima of basis renormalization. To sum up, the whole scenario completely agrees with Feigenbaum's theory of period-doubling subharmonic cascades, and it was also verified numerically by the explicit computation of δ_F, where only nine bifurcations were necessary to provide four significant figures of the universal constant. The essential features of the model and the numerical methods for its study were reported in (Meseguer, Marques & Sanchez, 1996).

Once Petrov-Galerkin schemes were checked numerically in chapters 3 and 4, the rest of the work dealt with the study of axial effects in the Taylor–Couette problem. The geometrical features of the problem and its particular boundary conditions required a special treatment of the Petrov-Galerkin formalism. In appendix D, a complete constructive analysis is proposed, applied extensively in chapters 5 and 6. Although some partial studies of the problem have been reported in the past (Hung, Joseph & Munson, 1972 or Ludwieg, 1964), they do not provide a comprehensive analysis of the competition between shear and centrifugal mechanisms of instability. The present task specially dealt with this analysis, focusing on new outstanding features appearing as an outcome of this competition. As a result, discontinuities and potential hysteresis mechanisms have been detected with the use of special numerical algorithms for the computation of neutral stability regimes. These new features (not commented or noticed in previous works) may have unwanted experimental consequences, making it necessary to repeat the experiments with more sophisticated devices. Despite the scattered experimental results provided by Ludwieg, our own computations are in good agreement with them. Moreover, a fair explanation of the cause of quantitative discrepances between Ludwieg's experiment and our results has been pointed out. A deeper analysis on the parameters used by different authors is provided in appendix D in order to clarify what was exactly measured in each work. For the present, the main results for wide and narrow gap cases $\eta = 0.5$ and $\eta = 0.8$ are reported in (Meseguer & Marqués, 1998).

Finally, chapter 6 is a formal approach to the weak nonlinear analysis of the Taylor-Couette problem. First, proposed was how the Petrov-Galerkin schemes can be used for the computation of the coefficients of the amplitude equations which lead the nonlinear behaviour of the flow just after the bifurcation has taken place. Secondly, the study of $\mathsf{O}(2)$ to $\mathsf{SO}(2)$ symmetry breaking under the presence of imposed axial effects was studied. The theoretical predictions from the normal form analysis have been confirmed numerically, agreeing with former predictions stated in (Armbruster & Mahalov, 1992) where stationary secondary patterns are expected under specific conditions (codimension-2 bifurcation).

7.2 Perspectives and Applications

Part of the development of the main ideas proposed in this work are within the frame of parallel studies related with axial effects in Taylor–Couette problem. In fact, Petrov-Galerkin methods can be used for more general purposes, as well as in the nonlinear regime. This is essentially the result of the work of Marques & Lopez, 1997, in which the stability of nonlinear periodic regimes of the Taylor–Couette problem submitted to axial oscillations was studied. At this time, the next step would be to consider nonlinear axial effects after criticality and to study the stability of some secondary flows predicted by the linear theory. On the one hand, the presence of dominant axisymmetric patterns (*Taylor vortex*) in the linear regime for high axial speeds must be checked nonlinearly. On the other hand it is necessary to make a nonlinear integration of the combined effects axial sliding and imposed axial pressure gradient in order to confirm the existence of steady axisymmetric cellular structures.

A better understanding of the competition of centrifugal and shear instability mechanisms is needed for the improvement of different industrial processes. One example is the purification of waste water, in which the fluid is rotated and driven axially simultaneously. Therefore, the exact control of inestabilization of the basic flow would avoid pre-turbulent stages, which could affect the effectiveness of the global purification procedure. Another direct application could related to the massive production on optical fibers. In this case, the fiber, in its fluid state, is injected under the effects of high pressure gradients. For such reasons, a comprehensive study of the stability of *Couette–Poiseuille* basic flow is essential.

Appendix A

Regularized Driven Cavity Flow: Explicit Computations

A.1 Computation of a Free-divergence Particular Solution

Our main goal is to obtain a solenoidal particular solution which satisfies the original boundary conditions. For this purpose, we consider a function $\psi(x,y)$ defined over the two-dimensional set $\Omega = [-1,1] \times [-1,1]$ such that the sought vector field can be derived from it

$$\mathbf{u}_p(x,y) = (v_p^x, v_p^y, 0) = \nabla \times (\psi \mathbf{k}), \quad v_p^x = \partial_y \psi, \quad v_p^y = -\partial_x \psi \tag{A.1}$$

It should be remarked here that ψ is not a stream function for the original problem. The consideration of this function is only a pure mathematical artifact in order to obtain a solenoidal field from it. For the sake of simplicity, the separation of variables hypothesis will be considered on the functional structure of ψ. We suppose that the sought function is The result of a product of two single variable functions

$$\psi(x,y) = F(x)G(y) \tag{A.2}$$

Now, imposing the boundary conditions (3.3) which must be satisfied by the field $\mathbf{u}_{\mathrm{p}}$, suitable functions F and G can be obtained. To sum up, the conditions are

$$v_p^y(x,\pm 1) = 0 \rightarrow \partial_x \psi(x,\pm 1) = 0 \rightarrow F'(x)G(\pm 1) = 0 \rightarrow G(\pm 1) = 0 \tag{A.3}$$

$$v_p^y(\pm 1,y) = 0 \rightarrow \partial_x \psi(\pm 1,y) = 0 \rightarrow F'(\pm 1)G(y) = 0 \rightarrow F'(\pm 1) = 0 \tag{A.4}$$

$$v_p^x(\pm 1,y) = 0 \rightarrow \partial_y \psi(\pm 1,y) = 0 \rightarrow F(\pm 1)G'(y) = 0 \rightarrow F(\pm 1) = 0 \tag{A.5}$$

$$v_p^x(x,-1) = 0 \rightarrow \partial_y \psi(x,-1) = 0 \rightarrow F(x)G'(-1) = 0 \rightarrow G'(-1) = 0 \tag{A.6}$$

$$v_p^x(x,1) = r(x) \rightarrow \partial_y \psi(x,1) = r(x) \rightarrow F(x)G'(1) = r(x) \rightarrow F(x) = \frac{r(x)}{G'(1)} \tag{A.7}$$

where $r(x)$ is the prescribed regularized profile over the top boundary ($r(x) = R(x^2-1)^2$ in the present case). Of course, the previous equations do not determine uniqueness of the functions F and G. On the contrary, many different options are available. In fact, the selection need to be done depending on the family of orthogonal functions which will be used later on the projection scheme. For this purpose, we have considered simple low order polynomials in the variables x and y. For example, from equations (A.4) and (A.5), the structure for $F(x)$ can be obtained. A simple option could be

$$F(x) = (x^2-1)^2 f(x) \tag{A.8}$$

where $f(x)$ is a continuous and differentiable function in $x = \pm 1$. For $G(x)$, the vanishing conditions are not so restrictive. From equation (A.3), the structure of $G(x)$ may be guessed

$$G(y) = (y^2-1)g(y) \tag{A.9}$$

with $g(y)$ a smooth function whose part of its structure is conditioned by the fourth boundary condition (A.6). A linear factor is only needed for this purpose such that

$$G(y) = (y^2-1)(y+1) \tag{A.10}$$

is a compatible solution. Finally, equation (A.7) will lead the regularity of the factor $f(x)$

$$f(x) = \frac{r(x)}{(x^2-1)^2 G'(1)} = \frac{r(x)}{4(x^2-1)^2} \tag{A.11}$$

where equations (A.10) and (A.8) have been used. The last equation reflects the regularity conditions which must be satisfied by the profile $r(x)$. To sum up, the regularity conditions over $r(x)$ can be synthesized in the following form

$$r(x) \sim \mathcal{O}[(x \pm 1)^2] \tag{A.12}$$

In our specific case the regularized profile is $r(x) = R(x^2-1)^2$, thus $f(x) = R/4$. Therefore, a simple option for ψ is

$$\psi(x,y) = \frac{R}{4}(x^2-1)^2(y^2-1)(y+1) \tag{A.13}$$

and the associated solenoidal field derived from it is

$$\mathbf{u}_\mathrm{p} = (\frac{R}{4}(3y-1)(y+1)(x^2-1)^2, -Rx(y+1)(y^2-1)(x^2-1)) \tag{A.14}$$

A.2 Coefficients for the Dynamical System of Amplitudes

The matrix elements which appear in chapter 3 are explicitly expressed as follows

$$A_{ijkl} = \int_\Omega \{\tilde{f}_i(x)\tilde{g}'_j(y) f_k(x) g'_l(y) + \tilde{f}'_i(x)\tilde{g}_j(y) f'_k(x) g_l(y)\} d\Omega \tag{A.15}$$

$$B_{ijkl} = \int_\Omega \{\tilde{f}_i(x)\tilde{g}'_j(y)\Delta[f_k(x)g'_l(y)] + \tilde{f}'_i(x)\Delta[\tilde{g}_j(y)f'_k(x)g_l(y)]\}d\Omega \tag{A.16}$$

$$\begin{aligned} C^R_{ijkl} = \int_\Omega \{ & \tilde{f}_i(x)\tilde{g}'_j(y)[v^x_p\partial_x + v^y_p\partial_y][f_k(x)g'_l(y)] + \\ & \tilde{f}'_i(x)\tilde{g}_j(y)[v^x_p\partial_x + v^y_p\partial_y][f'_k(x)g_l(y)] - \\ & \tilde{f}_i(x)\tilde{g}'_j(y)[-f_k(x)g'_l(x)\partial_x + f'_k(x)g_l(x)\partial_y]v^x_p + \\ & \tilde{f}'_i(x)\tilde{g}_j(y)[-f_k(x)g'_l(x)\partial_x + f'_k(x)g_l(x)\partial_y]v^y_p\}d\Omega \end{aligned} \tag{A.17}$$

$$\begin{aligned} N_{ijklmn} = \int_\Omega \{ & \tilde{f}_i(x)\tilde{g}'_j(y)[-f_k(x)g'_l(x)\partial_x + f'_k(x)g_l(x)\partial_y][f'_m(x)g'_n(y)] + \\ & \tilde{f}'_i(x)\tilde{g}_j(y)[-f_k(x)g'_l(x)\partial_x + f'_k(x)g_l(x)\partial_y][f'_m(x)g_n(y)]\}d\Omega \end{aligned} \tag{A.18}$$

$$\begin{aligned} b^R_{ij} = \int_\Omega \{ & -\tilde{f}_i(x)\tilde{g}'_j(y)\Delta v^x_p + \tilde{f}'_i(x)\tilde{g}_j(y)\Delta v^y_p + \\ & \tilde{f}_i(x)\tilde{g}'_j(y)[v^x_p\partial_x + v^y_p\partial_y]v^x_p - \tilde{f}'_i(x)\tilde{g}_j(y)[v^x_p\partial_x + v^y_p\partial_y]v^y_p\}d\Omega \end{aligned} \tag{A.19}$$

where $\Omega = [-1,1] \times [-1,1]$ and the functions $\tilde{f}_i$, $\tilde{g}_j$, f_k and g_l are defined as follows

$$\tilde{f}_i(x) = (1-x^2)^{3/2}T_i(x) \quad \tilde{g}_j(y) = (1-y^2)^{3/2}T_j(y) \tag{A.20}$$

$$f_k(x) = (1-x^2)^2 T_k(x) \quad g_l(y) = (1-y^2)^2 T_l(y) \tag{A.21}$$

being $T_m(x)$ the $i-$th order Tchebyshev polynomial

$$T_m(x) = \cos(m \arccos x), \quad x \in [-1,1] \tag{A.22}$$

The functions v^x_p and v^y_p are the cartesian components of the solenoidal field $\mathbf{u}_{\mathrm{p}}$ defined in equation (A.14) and Δ stands for the laplacian operator in two-dimensional cartesian coordinates

$$\Delta = \partial^2_x + \partial^2_y \tag{A.23}$$

The matrix elements can be computed numerically making use of Gauss-Tchebyshev quadrature schemes (Press *et al.* , 1986). In fact, the numerical integration is exact if the order of the quadrature greater or equal than the order of the polynomic factors which appear in the integrals.

Appendix B

Low-Dimensional Model: Explicit Computations

We consider the adimensionalized Navier-Stokes equations for incompressible fluids:

$$\partial_t \mathbf{v} + (\mathbf{v} \cdot \nabla)\mathbf{v} = -\nabla p + \Delta \mathbf{v} \quad , \quad \nabla \cdot \mathbf{v} = 0 \tag{B.1}$$

In order to build a weighted residual scheme, we will work with two different function spaces. Let $\mathcal{H}_d$ be the projection space of test functions:

$$\mathcal{H}_d = \{\tilde{\phi} \in L^2(\Omega),\ \nabla \cdot \tilde{\phi} = 0,\ \tilde{\phi} \cdot \hat{n} \mid_{\partial\Omega} = 0\} \tag{B.2}$$

where $\hat{n}$ is the unit normal to $\partial\Omega$, and let $\mathcal{H}_s$ be the space of divergence-free functions:

$$\mathcal{H}_s = \{\hat{\phi} \in L^2(\Omega),\ \vec{\nabla} \cdot \hat{\phi} = 0\} \tag{B.3}$$

Both spaces will be spanned by solenoidal functions $\mathcal{H}_d = \text{Span} < \tilde{\phi}_{pq} >$, $\mathcal{H}_s = \text{Span} < \phi_{mn} >$ of the form

$$\tilde{\phi}_{pq}(x,y) = \begin{pmatrix} -\tilde{f}_p(x)\tilde{g}'_q(y) \\ \tilde{f}'_p(x)\tilde{g}_q(y) \end{pmatrix} \quad , \quad \phi_{mn}(x,y) = \begin{pmatrix} -f_m(x)g'_n(y) \\ f'_m(x)g_n(y) \end{pmatrix} \tag{B.4}$$

where $'$ means derivative, and the normal component of $\tilde{\phi}_{pq}$ vanishes on the boundary $\partial\Omega$ of the domain: $\tilde{\phi} \cdot \hat{n} = 0$. These vectorial functions satisfy the divergence–free condition and are a base of the Hilbert spaces $\mathcal{H}_d$ and $\mathcal{H}_s$ respectively. Now the velocity field is of the form:

$$\mathbf{v}(x,y,t) = \sum_{m=0}^{M} \sum_{n=0}^{N} a_{mn}(t)\phi_{mn}(x,y) \tag{B.5}$$

The selection criteria of the set of functions $\tilde{\phi}_{pq}$ and ϕ_{mn} depend on the geometry of the problem and the boundary conditions. In fact, these functions will be built up using suitable orthogonal polynomials (see Canuto *et al.* , 1988 or Moser, Moin & Leonard, 1983 for a detailed discussion). We take the f and g functions as

$$\tilde{f}_p(x) = f_p(x) = (x^2 - 1)^2 P_p(x) \tag{B.6}$$

$$\tilde{g}_q(y) = g_q(y) = (y^2 - 1) P_q(y) \tag{B.7}$$

where P_p is the p^{th}-order Legendre polynomial. Thanks to the factors $(x^2-1)^2$ and y^2-1 the boundary conditions (4.1) are satisfied, except for the tangential component on $y=\pm 1$. This remaining boundary condition will be set by the tau method.

The weak form of problem (B.1) will be

$$< \tilde{\phi} \mid \partial_t \mathbf{v} + (\mathbf{v}\cdot\nabla)\mathbf{v} - \Delta\mathbf{v} >= 0 \quad , \quad \forall\tilde{\phi}\in\mathcal{H}_d,\ \mathbf{v}\in\mathcal{H}_s \tag{B.8}$$

where $<\cdot\mid\cdot>$ is the standard Hermitian product. The pressure term $<\tilde{\phi}\mid\nabla p>$ vanishes for all $\tilde{\phi}\in\mathcal{H}_d$ (Temam, 1988). When the remaining boundary conditions are set, the coefficients a_{mn} are no longer independent. In fact we can find $a_{m,N}$, $a_{m,N-1}$ in terms of the remaining $a_{m,n}$, for all m. From Eq. (4.1),

$$a_{m,n} = -\frac{R}{4}\delta_{m,0} - \sum_{k=1}^{[n/2]} a_{m,n-2k}\ ; \qquad n=N,\,N-1\ ; \quad m=0\div M \tag{B.9}$$

corresponding to the imposed velocity profile $v(x)=R(x^2-1)^2$ on $y=1$. The Eqs. (B.8) for the independent amplitudes in the case $N=3$, $M=1$ are Eqs. (4.2), where $u=a_{00}$, $v=a_{01}$, $w=a_{10}$ and $z=a_{11}$. The values of the numerical constants that appear in the Eqs. (4.2) are:

$$\begin{array}{llll}
\lambda_1 = 133/64 & \lambda_2 = 573/80 & \lambda_3 = 991/20592 & \lambda_4 = 73/5720 \\
\nu_1 = 23/2904 & \nu_2 = 1615/113256 & \nu_3 = 703/15730 & \nu_4 = 685/9438 \\
d_1 = 483/32 & d_2 = 267/8 & d_3 = 2003/80 & d_4 = 1521/40 \\
\delta_1 = 499/1716 & \delta_2 = 5/396 & \delta_3 = 801/1430 & \delta_4 = 17/26 \\
\rho_1 = 380/1573 & \rho_2 = 760/4719 & \rho_3 = 4776/7865 & \rho_4 = 280/1573 \\
\rho_5 = 12/143 & \rho_6 = 620/429 & \rho_7 = 504/715 & \rho_8 = 240/143 \\
\rho_9 = 1296/3575 & \rho_{10} = 72/1859 & &
\end{array} \tag{B.10}$$

Appendix C

Computation of Periodic Orbits

C.1 First Order Variational Equations

Consider a dynamical system

$$\dot{x} = f(x) \tag{C.1}$$

defined over an bounded open subset $\mathcal{U} \subset \mathbb{R}^n$. The uniparametric group of transformations , $\phi_t(x) = \phi(t,x)$ describes the flow of a particular initial point x after a time t, being the solution of the initial value problem

$$\dot{x} = f(x), \quad \phi_0(x) = x \tag{C.2}$$

If $f \in C^p$, the same order of smoothness for the flow ϕ may be assumed. For a fixed t value, the flow $\phi_t(x)$ may be interpreted as a continuous and differentiable map

$$\begin{array}{rccc} \phi_t(x): & \mathbb{R}^n & \longrightarrow & \mathbb{R}^n \\ & x & & \phi(t,x). \end{array} \tag{C.3}$$

In order to extract the qualitative information of the local geometric properties of the flow, the behaviour of ϕ must be studied in detail. From an analytical point of view, $\phi_t(x)$ is a diffeomorphism whose topological features may change as the paramater t evolves. Consequently, the local evolution of volume elements in phase space will be governed by the derivative of ϕ near the point x. For this purpose, the first order variations produced by a local increment Δx are considered

$$\phi_t(x+\Delta x) = \phi_t(x) + [D\phi_t(x)]\Delta x + \frac{1}{2}[D^2\phi_t(x)]\Delta^2 x + o(\Delta^2 x) \tag{C.4}$$

Now, regarding that $\phi_t(x)$ is the solution of the initial value problem (C.2)

$$\dot{\phi}_t(x) = f(\phi_t(x)). \tag{C.5}$$

The last equation will be very useful for the present purposes because it allows the change of order of derivation with respect x and t independently. For the sake of simplicity, only the first order variations are going to be considered for the study of the flow $\phi_t(x)$. In fact, the qualitative behaviour of volume elements in phase space is led by the first order terms. Therefore, the time-evolution of the linear map $D\phi_t(x)$ must be studied. This will be accomplished by taking the first order derivative with respect to t.

$$\frac{d}{dt}\frac{\partial}{\partial x}\phi_t(x) = \frac{\partial}{\partial x}\frac{d}{dt}\phi_t(x) = \frac{\partial}{\partial x}f(\phi_t(x)) = Df(\phi_t(x))\frac{\partial}{\partial x}\phi_t(x) \tag{C.6}$$

which leads to a dynamical system for the first order variations, whose explicit structure is

$$\frac{d}{dt}\begin{pmatrix} \partial_{x_1}\phi_t^1 & \cdots & \partial_{x_n}\phi_t^1 \\ \vdots & \ddots & \vdots \\ \partial_{x_1}\phi_t^n & \cdots & \partial_{x_n}\phi_t^n \end{pmatrix} = \begin{pmatrix} \partial_{x_1}f^1 & \cdots & \partial_{x_n}f^1 \\ \vdots & \ddots & \vdots \\ \partial_{x_1}f^n & \cdots & \partial_{x_n}f^n \end{pmatrix}\begin{pmatrix} \partial_{x_1}\phi_t^1 & \cdots & \partial_{x_n}\phi_t^1 \\ \vdots & \ddots & \vdots \\ \partial_{x_1}\phi_t^n & \cdots & \partial_{x_n}\phi_t^n \end{pmatrix} \tag{C.7}$$

with the initial condition

$$\begin{pmatrix} \partial_{x_1}\phi_t^1 & \cdots & \partial_{x_n}\phi_t^1 \\ \vdots & \ddots & \vdots \\ \partial_{x_1}\phi_t^n & \cdots & \partial_{x_n}\phi_t^n \end{pmatrix}_{t=0} = \begin{pmatrix} 1 & \cdots & 0 \\ \vdots & \ddots & \vdots \\ 0 & \cdots & 1 \end{pmatrix}. \tag{C.8}$$

The initial value problem formed by equations (C.7) and (C.8) is usually termed *First order variational equations* and it must be integrated simultaneously with system (C.2). The computational cost of the numerical integration will depend on the dimension of the global system. The stiffness of the equations requires powerful integrators capable of controlling the time increments near the initial conditions. For the present purposes, a Shampine & Gordon linear multi-step method provides enough accuracy, although more efficient schemes like Gear or implicit Runge-Kutta algorithms are highly recommended (Shampine & Gordon, 1975).

C.2 Numerical Computation of Poincaré Maps

For the study of stability of periodic or multi-periodic orbits of a dynamical system it is useful to consider the main features of their transversal sections instead of their global structure. This idea was originally proposed by Poincaré for the study of stability of planetary orbits in celestial mechanics. For this purpose, Poincaré considered surfaces immersed in the phase space which intersect tranversally to the periodic orbit under study. Poincaré realized that the information obtained from the intersection was enough in order to study the stability of the orbit. The geometrical mechanism is quite simple. First, consider a hypersurface Π_1 defined by equation $g_1(x) = 0$ crossing the flow $\phi_t(x_1)$ for $t = 0$ (this is, $x_1 = \phi(0,x)$) such that $\nabla g_1 \cdot f(\phi_t(x_1)) \neq 0$. Next, consider another hypersurface Π_2 given now by the relation $g_2(x) = 0$ intersecting transversally with the flow at the point x_2. In some sense, the flow $\phi_t(x)$ *mails* the point x_1 of Π_1 to the point x_2 of Π_2 for an specific value of t usually termed *flight-time*. Algebraically, this process can be interpreted as a map P defined between to manifolds as follows

$$\begin{array}{rccl} P: & \Pi_1 & \longrightarrow & \Pi_2 \\ & x_1 & & x_2 = \phi((t(x_1), x_1)) = P(x_1) \end{array}. \tag{C.9}$$

In fact, t is a function of x_1 (this is, different points of Π_1 need different *flight-times* to reach Π_2) and their dependence is is implicitly conditioned by the algebraic relation

$$g_2(\phi(t(x_1), x_1)) = 0. \tag{C.10}$$

Equation (C.10) is the cut condition for $t(x_1)$ and may be solved by a combined predictor algorithm of sign evaluation of g_2 over the flow followed by a corrector Newton's method:

$$t^{k+1} = t^k - \frac{g_2(x^k)}{\nabla g_2(x^k) \cdot f(x^k)}, \quad x^k = \phi(t^k, x_1) \tag{C.11}$$

The previous algorithm provides a numerical computation for the map defined previously in (C.9). For the present purposes, it will be only necessary to consider one transversal surface $\Pi_1 = \Pi_2 = \Pi_0$ defined by a linear equality $g(x) = 0$ (the Poincaré section) such that a point x_0 over Π_0 belongs to a periodic orbit if and only if

$$g(\phi(t(x_0), x_0)) = g(x_0) = 0 \tag{C.12}$$

for some value $t(x_0) = T$ which is just the period of the orbit. The previous argument is the classical setting of the usually termed *First return map* P. In fact, the main goal is to study the behaviour of closed trajectories interpreted as bijective maps over the Poincaré section. The essential information about the stability of trajectories is implicit in the map P. Therefore, the main point at this stage is the study of P and its effect on phase space dynamics. In order to simplify the analysis, the cut condition (C.10) will be given by setting one space coordinate (x_n, for example) to zero. This simplification can always be done assuming that $f(x_1)$ is not orthogonal to the canonical vector $e_n = (0, 0, \dots, 1)$. Therefore, the cut condition (C.10) is simplified to the expression

$$\phi^n(t(x), x) = 0. \tag{C.13}$$

The essential information about contraction or expansion effects in phase space is implicitly contained in the infinitesimal spatial variations of the map P

$$(DP)_{ij} = \partial_{x_j} P_i, \tag{C.14}$$

which can be obtained by explicit derivation of the definition of P given in (C.9)

$$\partial_{x_j} P_i = \partial_{x_j} \phi^i(t(x), x) = \partial_t \phi^i \partial_{x_j} t + \partial_{x_j} \phi^i = f^i(\phi(t(x), x) \partial_{x_j} t + \partial_{x_j} \phi^i. \tag{C.15}$$

In last equation, the factor $\partial_{x_j} \phi^i$ is given by the first variational equations (C.7) and (C.8). Besides, the unknown factor $\partial_{x_j} t(x)$ can be obtained by implicit derivation of (C.13) with respect to the spatial variables

$$\partial_{x_j} \phi^n(t(x), x) = \partial_t \phi^n \partial_{x_j} t(x) + \partial_{x_j} \phi^n = f^n(\phi(t(x), x)) \partial_{x_j} t(x) + \partial_{x_j} \phi^n(t(x), x) = 0, \tag{C.16}$$

therefore

$$\partial_{x_j} t(x) = -\frac{\partial_{x_j} \phi^n(t(x), x)}{f^n(\phi(t(x), x))}. \tag{C.17}$$

Finally, the differential of Poincaré map is given by the expression

$$\partial_{x_j} P = \partial_{x_j} \phi^i - \frac{f^i(\phi(x(t), x))}{f^n(\phi(x(t), x))} \partial_{x_j} \phi^i \tag{C.18}$$

which can be expressed in matrix form as follows

$$(DP)_{ij} = \sum_{k=1}^{n} (\delta_{ik} - \frac{f^i \delta_{kn}}{f^n})(\partial_{x_j} \phi^k), \quad (1 \le i, j \le n) \tag{C.19}$$

or

$$DP = (1_n - \frac{f \otimes e_n}{f_n}) J, \tag{C.20}$$

where 1_n is the $n-$dimensional identity matrix, $f \otimes e_n$ stands for the dyadic product $f^i \delta_{kn}$ and $J = \partial_x \phi$.

C.3 Period-doubling Mechanism: Floquet Analysis

For the stability analysis of the periodic orbits, only the restriction over the Poincaré section Π_0 is needed. The interest is mainly focused on the transversal expansion and contraction local properties of the periodic orbit. For this purpose, the projection of the first order differential of the Poincaré map is considered

$$(F)_{ij} = \sum_{k=1}^{n} (\delta_{ik} - \frac{f^i \delta_{kn}}{f^n})(\partial_{x_j} \phi^k), \quad (1 \le i, j \le n-1). \tag{C.21}$$

The previous matrix provides essential information concerning stability of periodic orbit under study. Let be P the Poincaré map restricted to the $n-1$ dimensional plane self-connected by a periodic orbit wich crosses the plane at the point x_0. From the point of view of maps, x_0 is, under the previous hypotheses, a fixed point of $P-$ that is, $P(x_0) = x_0$. Now, consider another point $x = x_0 + \delta$ in a neighborhood of x_0 ($\|\delta\| \to 0$). Lets study the behaviour of the perturbation δ under the action of P:

$$P(x_o + \delta) = P(x_o) + (DP_0)\delta + \mathcal{O}(\delta^2) = x_0 + F\delta + \mathcal{O}(\delta^2), \tag{C.22}$$

where (DP_0) stands for the first order differential of the Poincaré map evaluated at x_0, which is in fact the linear map F defined in equation (C.21). Thus, neglecting non-linear terms:

$$P(x_0 + \delta) = x_0 + F\delta. \tag{C.23}$$

Therefore, the initial perturbation δ is transformed linearly by the map F. The same process can be repeated twice in order to see the linear effects over δ

$$P^{(2)}(x_0 + \delta) = P[P(x_0 + \delta)] = P(x_0 + F\delta) = x_0 + F^2\delta, \tag{C.24}$$

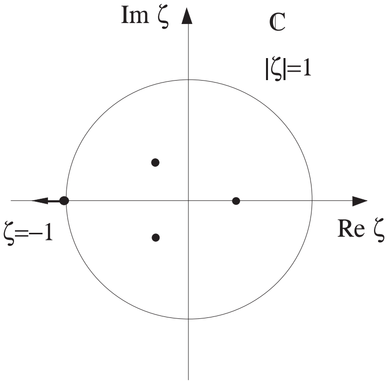

Figure C.1: Featuring period-doubling mechanism. One of the eigenvalues of the spectrum of the first order differential of Poincaré map crosses the unit circle in the complex plane passing throughout the point $\zeta = -1$, while the rest of eigenvalues remain inside the disc $\|\zeta\| = 1$.

where non-linear terms have been neglected again. Finally, after $m-$ complete periods, the initial perturbation δ is transformed by the following linear rule

$$\delta \longrightarrow F^m \delta \tag{C.25}$$

As a consequence, the geometrical evolution of the vector δ will be conditioned by the spectrum of eigenvalues of the matrix F. This matrix is usually termed *Floquet matrix* and its eigenvalues are known as characteristic exponents or more frequently *Floquet exponents.* Those eigenvalues will be in general complex and their modulus will conditionate the dilation or contraction of the vector δ. Floquet theory asserts stability of the periodic orbit if the spectrum of eigenvalues of F lies inside the unit circle over the complex plane. If the global system is perturbed (by increasing an external parameter, for example) the spectrum of eigenvalues may change. The inestabilization is achieved when, at least, one of the Floquet exponents crosses the unit disc. The mechanism under which this process is done may be very complicated and it is just what characterizes the bifurcation. A global analysis of the different kind of phenomena is out of the scope of the present appendix. For the present purposes, it is enough to consider a particular case.

The period-doubling bifurcation occurs when one of the Floquet exponents crosses the unit circle by the point $z = -1$ (see Fig. C.1). As a consequence, there appears a transversal one-dimensional subspace spanned by an eigenvector v_p such that

$$F v_p = -v_p \tag{C.26}$$

If now, the infinitesimal perturbation is taken in the direction of the eigenvector v_p- that is, $\delta = \epsilon v_p$ $(\epsilon \to 0)$, then

$$P(x_0 + \delta) = P(x_0 + \epsilon v_p) = x_0 + F(\epsilon v_p) = x_0 - \epsilon v_p = x_0 - \delta \tag{C.27}$$

and, similarly

$$P^{(2)}(x_0 + \delta) = P[P(x_0 + \epsilon v_p)] = P(x_0 - \delta) = x_0 + \delta \tag{C.28}$$

Therefore, the perturbed point turns to be a fixed point for the map $P^{(2)} = (P \circ P)$. In other words, a twice-periodic orbit appears (Bergé *et al.* , 1984). From that stage on, the stability analysis of the appearing orbit must be slightly modified because a new Poincaré map ($P^{(2)}$) for the new period must be defined. Moreover, the topological features of the orbits may change and the section surfaces may not be valid or not optimal for accurate computations. Altogether, the modifications on the numerical scheme must be done *ad hoc* depending on the particular behaviour of the system.

C.4 Asymptotic Behaviour: Computation of Lyapunov Exponents

The purpose of this section is to establish an algorithmic scheme capable of providing information about the long-time behaviour of periodic or multi-periodic orbits in phase space. As long as the periodic orbits exhibit period-doubling bifurcations, the dynamics of the system turns to be more and more complex. In fact, the period of the orbits increase as a power of 2. As a result, long-time numerical integrations are needed to make predictions about the stability of those orbits. Furthermore, subharmonic cascades produce typically chaotic behaviours beyond a limit accumulation value of the increasing control parameters. At the present stage, the term *chaotic* is introduced in the classical frame of sensibility with respect to initial conditions– that is, neighboring initial conditions exhibit uncorrelated evolutions for long time integrations. This feature should not be interpreted as instability or simple divergence of nearby initial trajectories. On the contrary, the dynamical evolution of volume elements in phase space is much more complicated. Simultaneous stretching and contracting phenomena can be frequently observed. From a geometrical point of view, the combination of both previous effects is just what characterizes chaotic regimes.

As in the previous section, consider the first order variations dynamical system

$$\left\{ \begin{array}{ll} \dot{x} = f(x) & \phi_0(x) = x_0 \\ \dot{J}(t) = (Df)J(t) & J(0) = 1_n \end{array} \right. , \tag{C.29}$$

where $J(t)$ stands for the first order variations map $D\phi_t(x)$ introduced in previous sections. If a slightly perturbed initial condition $x_0 + \delta_0$ is considered, the dynamical evolution of $\delta(t)$ will be led by the fundamental matrix $J(t)$ (Fig. C.2)

$$\delta(t) = J(t)\delta_0. \tag{C.30}$$

In fact, $J(t)$ can be interpreted as an exponential map in $\mathbb{R}^n$ as follows

$$J(t) = \begin{pmatrix} \mathrm{e}^{\lambda_1 t} & \cdots & 0 \\ \vdots & \ddots & \vdots \\ 0 & \cdots & \mathrm{e}^{\lambda_n t} \end{pmatrix} . \tag{C.31}$$

A measure of the asymptotic growth rate of the norm of δ along the trajectory $\phi_t(x)$ is given by the limit

$$\lambda(x_0, \delta_0) = \lim_{t \to \infty} \frac{1}{t} \ln \frac{\|J(t)\delta_0\|}{\|\delta_0\|} \tag{C.32}$$

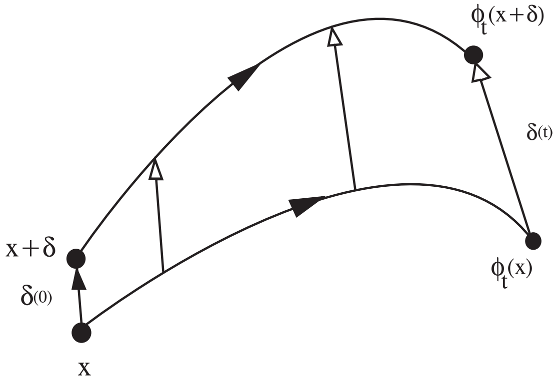

Figure C.2: Geometrical sketch of the evolution of the perturbed initial condition $x_0 + \delta_0$. At the first order, the evolution of $\delta(t)$ is led by the fundamental matrix $J(t)$ acting over δ_0.

The number $\lambda(x_0, \delta_0)$ is usually termed *Lyapunov exponent* and it measures the divergence rate of trajectories in the δ direction. If $\lambda(x_0, \delta_0) = \lambda_1 \neq 0$, then, for sufficiently high t:

$$\lim_{t \to \infty} \frac{1}{t} \ln \frac{\|J(t)\delta\|}{\|\delta\|} \sim \lambda_1 \tag{C.33}$$

therefore

$$\|J(t)\delta_0\| \sim \mathrm{e}^{\lambda_1 t} \|\delta_0\|, \tag{C.34}$$

i.e., the trajectories diverge or converge exponentially depending on the sign of λ_1. The Lyapunov exponent depends on the initial point of evolution x_0 and the direction defined by the initial perturbation δ_0. For fixed x, the Lyapunov exponent can acquire only a finite number of of mutually different values $\lambda_1, \lambda_2, \ldots, \lambda_k \quad (k \leq n)$ on the $n-$dimensional phase space. Thus, a basis $e_1, e_2, \ldots, e_n$ may be chosen to measure the behaviour of nearby flows in different directions.

At this stage, one of the essential features which needs to be captured from the global dynamics is the behaviour of $k-$dimensional volume elements in phase space. For this purpose, the $k - dimensional$ Lyapunov exponent is defined as follows

$$\lambda^{(k)}(x_0) \doteq \lim_{t \to \infty} \frac{1}{t} \ln \frac{\|J(t)e_1 \wedge J(t)e_2 \wedge \cdots \wedge J(t)e_k\|}{\|e_1 \wedge e_2 \wedge \cdots \wedge e_k\|} \tag{C.35}$$

Unfortunately, when Lyapunov exponents are evaluated directly by integrating variational equations, some numerical problems may arise. Depending on the complexity of the vector field, the dynamical system may exhibit chaotic behaviour. If it is the case, the variational equations have an exponentially divergent solution. Furthermore, there may be asymptotically stable manifolds throughout which, some components of the variational equations decay to zero. Altogether, it turns the fundamental matrix $J(t)$ to be ill-conditioned for computational purposes. In order to avoid this numerical problem, a renormalization method proposed by Shimada & Nagashima, 1979 is highly recommended.

The method considers a periodic renormalization of the basis $e_1, e_2, \ldots, e_k$ after a suitable transient time period τ. This renormalization is accomplished using the classical Gramm-Schmidt orthonormalization procedure

$$\begin{aligned}
e_1^{j+1} &= \frac{J(\tau)e_1^j}{\|J(\tau)e_1^j\|} \\
e_2^{j+1} &= \frac{J(\tau)e_2^j - (e_1^{j+1} \cdot J(\tau)e_2^j)e_1^{j+1}}{\|J(\tau)e_2^j - (e_1^{j+1} \cdot J(\tau)e_2^j)e_1^{j+1}\|} \\
e_3^{j+1} &= \frac{J(\tau)e_3^j - (e_1^{j+1} \cdot J(\tau)e_3^j)e_1^{j+1} - (e_2^{j+1} \cdot J(\tau)e_3^j)e_2^{j+1}}{\|J(\tau)e_3^j - (e_1^{j+1} \cdot J(\tau)e_3^j)e_1^{j+1} - (e_2^{j+1} \cdot J(\tau)e_3^j)e_2^{j+1}\|} \\
&\vdots \\
e_k^{j+1} &= \frac{J(\tau)e_k^j - \sum_{m=1}^{k-1}(e_m^{j+1} \cdot J(\tau)e_m^j)e_m^{j+1}}{\|J(\tau)e_k^j - \sum_{m=1}^{k-1}(e_m^{j+1} \cdot J(\tau)e_m^j)e_m^{j+1}\|} \qquad \text{(C.36)}
\end{aligned}$$

where the change of basis process is justified because of the invariance of subspaces generated under the exterior product. The exponents obtained under the computations of the previous algorithm provide information about the complexity of the time-dynamics. For instance, the existence positive values of Lyapunov exponents would evidence the presence of chaotic behaviour, while a zero maximum Lyapunov exponent would indicate the existence of periodic or multi-periodic regimes.

Appendix D

Spiral Taylor-Couette Problem: Petrov-Galerkin Formulation

D.1 Solenoidal Bases: Constructive Method

When considering axial-azimuthal periodicity of the physical system, the following functional structure on the perturbation fields can be assumed

$$\mathbf{v}(r,\theta,z) = \mathrm{e}^{\mathrm{i}(n\theta+kz)} \begin{pmatrix} v_r(r) \\ v_\theta(r) \\ v_z(r) \end{pmatrix}, \quad \forall n \in \mathrm{Z}, k \in \mathrm{I\!R} \tag{D.1}$$

where v_r, v_θ and v_z are the radial, azimuthal and axial components of the vector field, respectively. In order to built up a suitable complete set of solenoidal fields, the incompressibility condition must be considered. The condition $\nabla \cdot \mathbf{v} = 0$ leads to a functional dependence between the three components

$$D_+ v_r + \frac{in}{r} v_\theta + ikv_z = 0 \tag{D.2}$$

where the operators $D = \partial_r$ and $D_+ = D + 1/r$ have been used. In addition, the vector components must vanish over the radial boundaries $r_i = \frac{\eta}{1-\eta}$ and $r_o = \frac{1}{1-\eta}$ of the containing cylinders

$$v_r(r_i) = v_r(r_o) = v_\theta(r_i) = v_\theta(r_o) = v_z(r_i) = v_z(r_o) = 0 \tag{D.3}$$

For the sake of simplicity, three different situations will be considered. In each of them, independent radial, azimuthal and axial components are going to be studied in detail so that particular bases for those subspaces will be obtained. Finally, the linear dependence between them will be analysed.

- **Case I** ($v_\theta = 0$)

  In this case, axial and radial components are related as follows

$$D_+ v_r = -\mathrm{i}kv_z \tag{D.4}$$

To simplify the analysis, a particular functional structure for v_r and v_z is going to be imposed. They are explicitly defined as follows

$$v_r = -\mathrm{i}kf_j, \quad v_z = D_+ f_j \tag{D.5}$$

where f_j is a function depending on the radial variable whose structure will be particularly conditioned by the boundary conditions (D.3). At this stage, some freedom on the inner structure of f_j is present. In order to avoid $r^{-q}, (q > 0)$ factors in the hermitian products of the spectral projection, the structure of f_j has been selected as follows

$$f_j(x) = r^2(1-x^2)^2 T_j(x), \quad x = 2(r - r_i) - 1, \quad x \in [-1, 1], \tag{D.6}$$

where $T_j(x)$ is the $j-$th order Tchebyshev polynomial. The fourth order factor in f_j is needed for the homogeneous boundary condition on the axial component to be satisfied. On note that the selection (D.5) satisfies (D.2) identically. To sum up, the generic element of the basis of non-azimuthal solenoidal fields is

$$\mathbf{v}_j^1 = \begin{pmatrix} -\mathrm{i}kf_j \\ 0 \\ D_+ f_j \end{pmatrix}. \tag{D.7}$$

It should be remarked that this set of functions is a basis for $k \neq 0$ only. For the axial-independent case, a particular analysis must be done. For $k = 0$, (D.4) is reduced to the condition

$$D_+ v_r = 0 \to \frac{dv_r}{v_r} = -\frac{dr}{r} \to v_r(r) = \frac{C}{r}. \tag{D.8}$$

Now, imposing the boundary conditions (D.3) over v_r, the trivial solution $v_r = 0$ is obtained. Therefore, a suitable alternative is given by the generic element

$$\mathbf{v}_j^1 = \begin{pmatrix} 0 \\ 0 \\ h_j \end{pmatrix} \quad (k = 0), \tag{D.9}$$

where h_j has a laxer structure on its binomial factor

$$h_j(x) = r^2(1-x^2) T_j(x), \quad x = 2(r - r_i) - 1, \quad x \in [-1, 1], \tag{D.10}$$

- **Case II** ($v_z = 0$)

  In this second case, the solenoidal condition (D.2) is reduced to the equation

$$D_+ v_r = -\mathrm{i}\frac{n}{r} v_\theta \quad \text{or} \quad D(rv_r) = -\mathrm{i}nv_\theta \tag{D.11}$$

For the structure of f_j, the same process of selection explained in previous case is considered. Equation (D.11) is identically satisfied on choosing

$$v_r = -\mathrm{i}f_j, \quad v_\theta = D(rf_j) \tag{D.12}$$

Thus, a suitable generic element of the basis of non-axial solenoidal fields is

$$\mathbf{v}_j^2 = \begin{pmatrix} -\mathrm{i}nf_j \\ D(rf_j) \\ 0 \end{pmatrix}. \tag{D.13}$$

Again, the previous set of functions is complete for $n \neq 0$ only. For the axisymmetric case ($n = 0$), the trivial solution $v_r = 0$ is obtained again. As a consequence, the alternative generic basis element is

$$\mathbf{v}_j^2 = \begin{pmatrix} 0 \\ h_j \\ 0 \end{pmatrix} \quad (n = 0), \tag{D.14}$$

where h_j has the same structure than in case I.

- **Case III** ($v_r = 0$). In this case, the condition (D.2) is reduced to the simple equation

$$nv_\theta = -rkv_z \tag{D.15}$$

Consequently, the generic element of the basis of non-radial solenoidal fields is

$$\mathbf{v}_j^3 = \begin{pmatrix} 0 \\ -rkh_j \\ nh_j \end{pmatrix} \forall n, k. \tag{D.16}$$

Proposition D.1.1 (Linear dependence of $\mathbf{v}_j^2$.) *The set of functions $\mathbf{v}_j^2$ is linearly dependent of $\mathbf{v}_j^1$ and $\mathbf{v}_j^3$ for $k \neq 0$.*

Proof. Consider the following linear combination of $\mathbf{v}_j^1$ and $\mathbf{v}_j^3$

$$\frac{n}{k}\mathbf{v}_j^1 - \mathbf{v}_j^3. \tag{D.17}$$

Without loss of generality, if can be considered a particular structure for the function h_j

$$h_j = \frac{1}{k} D_+ f_j \tag{D.18}$$

Formal substitution of h_j in linear combination (D.17) gives to the generic vector field

$$\begin{pmatrix} -\mathrm{i}nf_j \\ D(rf_j) \\ 0 \end{pmatrix}, \tag{D.19}$$

which is an element of $\mathbf{v}^2$.

Although there is not a formal conclusion, it is a well known fact that confined axially extended flows are linearly stable to axial uniform perturbations. Experimental and numerical evidences suggest a preferred finite axial periodicity to inestabilize the flow. This property simplifies considerably the Petrov-Galerkin formulation because the ($k = 0$) elements in cases **I** or **III** may be neglected as a first glance. Therefore, the sets $\mathbf{v}^1$ and $\mathbf{v}^3$ are going to be chosen in order to span the spectral approximations.

At thi stage, a suitable set of test functions is needed to project the operator acting over the specr

D.2 Petrov-Galerkin Projection

As it was explained in previous section, the perturbed fields can be expressed as linear combinations of normal axial-azimuthal modes. Thus, perturbed velocity and pressure fields are written as follows

$$\mathbf{v}(r,\theta,z,t) = \mathbf{v}_B(r) + \mathrm{e}^{\mathrm{i}(n\theta+kz)+\lambda t}\mathbf{u}(r), \tag{D.20}$$

$$p(r,\theta,z,t) = p_B(r,z) + p'(r)\mathrm{e}^{\mathrm{i}(n\theta+kz)+\lambda t},. \tag{D.21}$$

Formal substitution of fields (D.20) and (D.21) in the linearized Navier-Stokes equation of the perturbation fields leads to a decoupled system of eigenvalues (5.28) whose explicit expression of is

$$\lambda \begin{pmatrix} v_r \\ v_\theta \\ v_z \end{pmatrix} = \begin{pmatrix} D_+ D v_r - (\frac{n^2+1}{r^2} + k^2) v_r - \frac{2}{r^2} i n v_\theta \\ D_+ D v_\theta - (\frac{n^2+1}{r^2} + k^2) v_\theta + \frac{2}{r^2} i n v_r \\ D_+ D v_z - (\frac{n^2+1}{r^2} + k^2) v_z \end{pmatrix} - \tag{D.22}$$
$$(in\frac{v_B}{r} + ikw_B) \begin{pmatrix} v_r \\ v_\theta \\ v_z \end{pmatrix} - \begin{pmatrix} -\frac{2}{r} v_\theta v_B \\ (\frac{v_B}{r} + D v_B) v_r \\ v_r D w_B \end{pmatrix} + \begin{pmatrix} D p' \\ \frac{in}{r} p' \\ ikp' \end{pmatrix}$$

where $\mathbf{v}_B = (0, v_B, w_B)$ is given by (5.23) and the perturbation velocity field $\mathbf{u} = (v_r, v_\theta, v_z)$ is enforced to vanish over the radial boundaries

$$\mathbf{u}(r_i) = \mathbf{u}(r_o) = \mathbf{0} \tag{D.23}$$

and to satisfy the solenoidal condition

$$D_+ v_r + \frac{in}{r} v_\theta + ikv_z = 0 \tag{D.24}$$

This is just the mathematical frame which has developed in the previous section. Consequently, the discretization of the eigenvalue problem is going to be accomplished with the spectral approximation

$$\mathbf{u} = \sum_{j=0}^{M} a_j \mathbf{u}_j^1 + b_j \mathbf{u}_j^2 \tag{D.25}$$

for the velocity field. Where $\mathbf{u}_j^1$ and $\mathbf{u}_j^2$ are elements of $\mathbf{v}^3$ and $\mathbf{v}^1$, respectively

$$\mathbf{u}_j^1 = (0, -rkh_j(r), nh_j(r)), \tag{D.26}$$

$$\mathbf{u}_j^2 = (-\mathrm{i}kf_j(r), 0, D_+ f_j(r)). \tag{D.27}$$

At this stage, a suitable set of test functions is needed to project the linear operator (D.23) acting over the spectral approximation (D.25). The projection is now defined as the standard hermitian product

$$< \mathbf{u}, \mathbf{v} >= \int_{r_i}^{r_o} \mathbf{u}^* \cdot \mathbf{v} r dr, \tag{D.28}$$

where $*$ denotes complex conjugation. Therefore, the main goal is to find again a set of solenoidal test functions compatible with the previous sets $\mathbf{v}^1$ and $\mathbf{v}^3$. For this purpose, this set is chosen as follows

$$\mathbf{u}_i^1 = (0, -rk\tilde{h}_i, n\tilde{h}_i) \quad \mathbf{u}_i^2 = (-\mathrm{i}k\tilde{f}_i, 0, D_+\tilde{f}_i), \tag{D.29}$$

where now, $\tilde{f}_i$ and $\tilde{h}_i$ are functions whose structure will depend not only on the boundary conditions but also on the orthogonal family of polynomials selected for f_j and h_j. For Tchebyshev polynomials, it is necessary to modify slightly the power factor in the binomial element $(1-x^2)$ of $\tilde{f}_j$ and $\tilde{h}_j$

$$f_j(r) = (1-x^2)^2 T_j(x), \quad h_j(r) = (1-x^2) T_j(x), \tag{D.30}$$

$$\tilde{f}_j(r) = r^2(1-x^2)^{3/2} T_j(x), \quad \tilde{h}_j(r) = r^2(1-x^2)^{1/2} T_j(x). \tag{D.31}$$

This change is needed in order some orthogonality properties between the polynomials to be satisfied and to avoid sparse matrices in the numerical scheme. Nevertheless, it should be remarked here that the matrix elements apparing eventually in the projection, can be exactly computed for the azimuthal components only. Unfortunately, the axial factors contain logarithmic terms which destroy the band structure. On note that test functions defined previously in (D.31) vanish over the boundary. In general, this condition is not necessary for the anihilation of the pressure term in the projection scheme. The necessary conditions are properly divergence-free and zero orthogonal component over the radial boundary. At this stage, the essential point is that the solenoidal condition in cylindrical geometry enforces not only the anhiliation of the radial (normal) component of the velocity field but also the azimuthal one (in elements $\tilde{\mathbf{u}}_j^2$, for example)

Finally, the susbstitution of spectral approximation (D.25) and projection over the test functions (D.31) leads to a complex generalized $2(M+1)$-dimensional eigenvalue problem which can be simbolically expressed as follows

$$\lambda G \mathbf{x} = H \mathbf{x}, \tag{D.32}$$

or, in matrix notation

$$\lambda \begin{pmatrix} G^{11} & G^{12} \\ G^{21} & G^{22} \end{pmatrix} \mathbf{x} = \begin{pmatrix} H^{11} & H^{12} \\ H^{21} & H^{22} \end{pmatrix} \mathbf{x}, \tag{D.33}$$

where first and second superindexes identify the projection and spectral elements with respect which the inner product has been done. The explicit structures of the hermitian products appearing in (D.33) are

$$G_{ij}^{11} = \int_{r_i}^{r_o} r\tilde{h}_i (r^2k^2 + n^2) h_j dr \tag{D.34}$$

$$G_{ij}^{12} = n \int_{r_i}^{r_o} r\tilde{h}_i D_+ f_j dr \tag{D.35}$$

$$G_{ij}^{21} = n \int_{r_i}^{r_o} r(D_+\tilde{f}_i)h_j dr \tag{D.36}$$

$$G_{ij}^{22} = \int_{r_i}^{r_o} r[k^2\tilde{f}_i + (D_+\tilde{f}_i)D_+]f_j dr \tag{D.37}$$

$$\begin{aligned} H_{ij}^{11} &= \int_{r_i}^{r_o} \tilde{h}_i[r^2k^2(D_+D - \frac{n^2+1}{r^2} - k^2)r + rn^2(D_+D - \frac{n^2}{r^2} - k^2)]h_j dr \\ &- \mathrm{i}\int_{r_i}^{r_o} \tilde{h}_i(r^2k^2 + n^2)(\frac{n}{r}v_B + kw_B)rh_j dr \end{aligned}$$

$$\begin{aligned} H_{ij}^{12} &= n\int_{r_i}^{r_o} \tilde{h}_i[2k^2 f_j + r(D_+D - \frac{n^2}{r^2} - k^2)D_+]f_j dr \\ &- \mathrm{i}\int_{r_i}^{r_o} \tilde{h}_i[k^2r^2(\frac{v_B}{r} + \partial_r v_B) + n(n\frac{v_B}{r} + kw_B)D_+ + kn(\partial_r w_B)]f_j dr \end{aligned}$$

$$\begin{aligned} H_{ij}^{21} &= n\int_{r_i}^{r_o} [2k^2\tilde{f}_i + r(D_+\tilde{f}_i)(D_+D - \frac{n^2}{r^2} - k^2)]h_j dr \\ &+ \mathrm{i}\int_{r_i}^{r_o} [2k^2rv_B\tilde{f}_i - r(D_+\tilde{f}_i)(n\frac{v_B}{r} + kw_B)]h_j dr \end{aligned} \tag{D.38}$$

$$\begin{aligned} H_{ij}^{22} &= \int_{r_i}^{r_o} [rk^2\tilde{f}_i(D_+D - \frac{n^2+1}{r^2} - k^2) + r(D_+\tilde{f}_i)(D_+D - \frac{n^2}{r^2} - k^2)D_+]f_j dr \\ &- \mathrm{i}\int_{r_i}^{r_o} [(n\frac{v_B}{r} + kw_B)(k^2\tilde{f}_i + (D_+\tilde{f}_i)D_+) + k(D_+\tilde{f}_i)(\partial_r w_B)]f_j dr \end{aligned} \tag{D.39}$$

D.3 Computation of the Critical Points in the NSC

Consider the equation which determines the marginal stability condition

$$\sigma(k, R) = 0 \tag{D.40}$$

where σ is the real part of the first eigenvalue belonging to the spectrum of the problem (D.32) which is near to cross the imaginary axis. The parameter R represents one of the Reynolds numbers (R_i, R_o or R_z) which control the dynamics of the physical problem with two of them held fixed. The variable k is the axial wave number of the perturbation.

From a geometrical point of view, the previous equation defines a curve in the (k, R) plane which separates the stable physical configurations from the unstable ones. This curves are so termed Neutral Stability Curves (NSC) and have the typical parabolic profile with an absolute minimum for some value of $k = k_c$ (see fig. 5.13). When studying physical perturbations, all the possible real $k-$values must be considered simultaneously. The critical value k_c will be conditioned by the minimum associated R_c value over the curve. The main goal is to compute numerically the value of k_c where the NSC reaches its minimum R_c. As a matter of fact, the dependence $R = g(k)$ is not explicitly present in the analysis. As a consequence, change of sign detection algorithms of the σ function over a grid in the (k, R) plane are applied in order to compute the critical values. Change sign algorithms are useful in Taylor-Couette problem or in Benard convection due to the simple geometrical structure of the NSC. Unfortunately, when an axial symmetry breaking effect $\mathsf{O(2)}$ to $\mathsf{SO(2)}$ is imposed in the problem, the topological features of the NSC are strongly perturbed. As a consequence, some technical problems may arise. On the one hand, the NSC appear to be multievaluated and with sharpened profiles so that changes of sign require high resolution in the (k, R) evaluation grid. On the other hand, there may appear disconnected zones of instability (also termed islands of instability) far from the expected critical values. Altogether, the computational cost may be prohibitive in order to take advantage from change sign algorithms. Consequently, an alternative methodology is needed.

From an analytical point of view, Implicit Function Theorem ensures the existence of a local branch $R = g(k)$ near the (k_c, R_c) point under some specific conditions. In other words, equation (D.40) defines locally over an open set A a unique function $R = g(k) \in C^p(A)$ with $R_c = g(k_c)$ provided that:

$$\textbf{(i)} \qquad \sigma(k, R) \in C^p(A), \quad p \in \mathbb{N}^*, (k_c, R_c) \in A \tag{D.41}$$

$$\textbf{(ii)} \qquad \sigma(k_c, R_c) = 0 \tag{D.42}$$

$$\textbf{(iii)} \qquad \partial_R \sigma(k_c, R_c) \neq 0 \tag{D.43}$$

Under the previous hypotheses, the necessary condition for k_c to be an extreme point is

$$\left(\frac{dg}{dk}\right)_{k=k_c} = 0 \tag{D.44}$$

Making use of the implicit function theorem, the last equation can be expressed as a combination of partial derivatives of σ with respect the variables k and R. Applying the chain rule in equation (D.44)

$$\frac{d}{dk}\sigma(k, R) = \frac{d}{dk}\sigma(k, g(k)) = \partial_k \sigma + \partial_R \sigma \frac{dg}{dk} = 0 \tag{D.45}$$

so that a very useful relation is obtained

$$\frac{dg}{dk} = -\frac{\partial_k \sigma}{\partial_R \sigma} \tag{D.46}$$

which allows to express the extreme condition in the following form

$$\partial_k \sigma(k_c, R_c) = 0 \tag{D.47}$$

provided that $\partial_R \sigma(k_c, R_c) \neq 0$. Simultaneously, the condition of minimum is given by the following relation

$$\left(\frac{d^2 g}{dk^2}\right)_{k=k_c} > 0 \tag{D.48}$$

Deriving (D.45) implicitly with respect the variable k

$$\frac{d}{dk}[\partial_k \sigma + \partial_R \sigma \frac{dg}{dk}] = \partial^2_{k,k}\sigma + \left(\frac{dg}{dk}\right)[2\partial^2_{k,R}\sigma + \left(\frac{dg}{dk}\right)\partial^2_{R,R}\sigma] + \left(\frac{d^2 g}{dk^2}\right)\partial_R \sigma = 0 \tag{D.49}$$

evaluating the previous expression in (k_c, R_c), another important relation is obtained

$$\left(\frac{d^2 g}{dk^2}\right)_{k=k_c} = -\left(\frac{\partial^2_{k,k}}{\partial_R \sigma}\right)_{(k_c,R_c)} \tag{D.50}$$

where equation (D.44) has been used. Therefore, the condition of minimum will be given now by

$$\left(\frac{\partial^2_{k,k}}{\partial_R \sigma}\right)_{(k_c,R_c)} < 0 \tag{D.51}$$

D.4 Newton-Raphson Method for the Computation of (k_c, R_c)

The set of equations (D.42), (D.47) and (D.51) form a system of non-linear equations in $\mathbb{R}^2$ which must be solved numerically. To formalize the problem, we consider a function $\mathbf{F} : \mathbb{R}^2 \to \mathbb{R}^2$ defined as follows

$$\mathbf{F}(k, R) = \begin{pmatrix} \sigma(k, R) \\ \partial_R \sigma(k, R) \end{pmatrix} \tag{D.52}$$

Therefore, the problem can be expressed as follows

$$\mathbf{F}(k, R) = \mathbf{0}, \quad \frac{\partial^2_{k,k}}{\partial_R \sigma} < 0 \tag{D.53}$$

At this point, it should be regarded here that there is not a closed expression for $\sigma(k, R)$. In fact, the evaluation of this function requires the selection of the maximum real part eigenvalue. Assuming regular behaviour of the spectrum of the operator (**??**, the system (D.53) can be solved numerically making use of a Newton-Raphson algorithm which is described by the following iteration expression

$$(D\mathbf{F})(k^{(n)}, R^{(n)})[\begin{pmatrix} k^{(n+1)} \\ R^{(n+1)} \end{pmatrix} - \begin{pmatrix} k^{(n)} \\ R^{(n)} \end{pmatrix}] + \mathbf{F}(k^{(n)}, R^{(n)}) = \mathbf{0} \tag{D.54}$$

The method considers a initial iteration point $(k^{(0)}, R^{(0)})$ near the sought solution. This initial point will be obtained by a prediction of the local behaviour of the function σ near the critical point. $D\mathbf{F}(k^{(n)}, R^{(n)})$ stands for the jacobian matrix of F evaluated at the $n-$iteration point. Explicitly, the previous system can be expressed in the following form

$$\begin{pmatrix} \partial_k\sigma & \partial_R\sigma \\ \partial^2_{k,k}\sigma & \partial_{R,k}\sigma \end{pmatrix}_{(k^{(n)},R^{(n)})} \left[\begin{pmatrix} k^{(n+1)} \\ R^{(n+1)} \end{pmatrix} - \begin{pmatrix} k^{(n)} \\ R^{(n)} \end{pmatrix}\right] + \begin{pmatrix} \sigma \\ \partial_k\sigma \end{pmatrix}_{(k^{(n)},R^{(n)})} = \begin{pmatrix} 0 \\ 0 \end{pmatrix} \tag{D.55}$$

The partial derivatives which appear in the scheme can not be evaluated analitically. The numerical alternative is to evaluate those derivatives with a finite-differences method over a discrete grid in the (k, R) plane. For this purpose, a centered nine-point reticular configuration has been used. Figure (D.1) represents the lattice

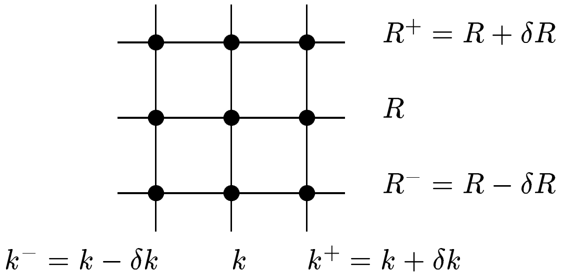

Figure D.1: Nine-point finite-difference lattice used for the evaluation of derivatives in the Newton-Raphson scheme.

The partial derivatives have been computed numerically making use of a nine-point relations (see, for example Abramowitz & Stegun, 1972). In the centered prescription they are

$$\partial_k\sigma = \frac{1}{2\delta k}[\sigma(k^+, R) - \sigma(k^-, R)] \tag{D.56}$$

$$\partial_k\sigma = \frac{1}{2\delta R}[\sigma(k, R^+) - \sigma(k, R^-)] \tag{D.57}$$

$$\partial^2_{k,k}\sigma = \frac{1}{2(\delta k)^2}[\sigma(k^-, R) - 2\sigma(k, R) + \sigma(k^+, R)] \tag{D.58}$$

$$\partial^2_{k,R}\sigma = \frac{1}{4\delta k\delta R}[\sigma(k^+, R^+) + \sigma(k^-, R^-) - \sigma(k^+, R^-) - \sigma(k^-, R^+)] \tag{D.59}$$

Newton-Raphson's method is cuadratically convergent whether the initial point of iteration (k^0, R^0) is near the sought solution (k_c, R_c) or not. Unfortunately, the topological structure of the basin of attraction may be very complicated. As a consequence, a predictor-steepest-descent method is required to optimize the scheme. The algorithm computes the gradient vector field of σ in each point of the (k, R)-plane and the predictor point is guided by the steepest path throughout which σ exhibits maximum local variations. This process is done departuring from different points of the plane until σ is positive. Although there is not a formal conclusion, it can be conjectured (from numerical evidences) that the corrector NR method converges more rapidly if $(k^{(0)}, R^{(0)})$ is in the positive σ zone. Nevertheless, it has been necessary to consider orientative values extracted from geometrical analyses to initialize the global search process. Although it was considered to modify the predictor method with a conjugate gradient scheme, the speed of the original one was enough for the present purposes.

D.5 Parameters from Different Authors

The functions $c_\phi(r)$, $c_z(r)$ (5.39) introduced by Ludwieg, 1964 are easily computed from the expressions (5.23):

$$c_\phi(r) = \frac{Ar^2 - B}{Ar^2 + B}, \quad c_z(r) = \frac{Cr}{Ar^2 + B}, \tag{D.60}$$

where the constants A, B, C are given by (5.24). Evaluating these expressions at the geometric mean radius $\bar{r} = \sqrt{r_i r_o}$, we get

$$\tilde{c}_\phi = \frac{1+\eta}{1-\eta}\frac{Ro - Ri}{Ro + Ri}, \quad \tilde{c}_z = -\frac{1+\eta}{\sqrt{\eta}\ln(1/\eta)}\frac{Rz}{Ro + Ri}. \tag{D.61}$$

By Taylor expanding near $\eta = 1$ we obtain

$$\frac{\sqrt{\eta}\ln(1/\eta)}{1-\eta} = 1 - \frac{(1-\eta)^2}{24} + \dots , \tag{D.62}$$

therefore (5.40) are the narrow gap approximations of the expressions (D.61). In fact the expression for $\tilde{c}_\phi$ is exact, and the difference in $\tilde{c}_z$ is only 0.2% for $\eta = 0.8$, so we will use the expressions (5.40) from now on. The difference in sign has been introduced for better comparison with the experiments, because if we simultneously change the signs of Rz, n and ω_c the marginal stability curve does not change (see §5.4 for a detailed account of the system symmetries).

The variables used by HJM, χ, $\tilde{\Omega}_2$ and R are related with the present parameters as

$$Ri = R\{\frac{\eta}{1-\eta}\tilde{\Omega}_2 + \sin\chi\}, \quad Ro = \frac{R\tilde{\Omega}_2}{1-\eta}, \quad Rz = R\cos\chi. \tag{D.63}$$

Their dependence with the Ludwieg parameters $\tilde{c}_\phi$ and $\tilde{c}_z$ is

$$\tilde{\Omega}_2 = \frac{1 + a\tilde{c}_\phi}{\sqrt{(a+1)^2\tilde{c}_z^2 + (1-\tilde{c}_\phi)^2}} \quad ; \quad \sin\chi = \frac{1 - \tilde{c}_\phi}{\sqrt{(a+1)^2\tilde{c}_z^2 + (1-\tilde{c}_\phi)^2}} \tag{D.64}$$

where $a = (1-\eta)/(1+\eta)$ and $Ro = 750$ is held fixed. From (D.63), (D.64) we can easily arrive at the same formulas (5.40), showing that HJM used the narrow–gap limiting values of $\tilde{c}_\phi$, $\tilde{c}_z$, or equivalently their values at the geometric mean radius $\bar{r} = \sqrt{r_i r_o}$.

Bibliography

M. Abramowitz & I. Stegun (*eds.*). *Handbook of Mathematical Functions.* Dover Publications, Inc., New York (1972).

M E. Ali, P.D. Weidman. *On the linear stability of cellular spiral Couette flow.* Phys. Fluids A. **5**, 1188-1200 (1993)

C. D. Andereck, S. S. Liu, and H. L. Swinney, *Flow regimes in a circular Couette system with independently rotating cylinders.* J. Fluid Mech. **164**, 155-83 (1986).

D. Armbruster, A. Mahalov *On the explicit symmetry breaking in the Taylor–Couette problem.* Phys. Lett. A 167 (1992) 251-254.

P. Bergé, Y. Pomeau, Ch. Vidal. *Lórder dans le Chaos.* Hermann (1984).

C. Boldrighini, V. Franceschini. Commun. Math. Phys. **64**, 159-170 (1979).

R. Cafarelli, R. Kohn, L. Niremberg. Comm. Pure. Appl. Math., **35**, 771 (1982).

C. Canuto, M.Y. Hussaini, A. Quarteroni, T.A. Zang. *Spectral Methods in Fluid Dynamics.* Springer-Verlag (Springer Series in Computational Physics) (1988).

S. Chandrasekhar. *Hydrodynamic and Hydromagnetic Stability.* Oxford Univ.Press (1961).

K. Chida, S. Sakaguchi, M. Wagatsuma, T. Kimura. *High-speed coating of optical fibres with thermally curable silicone resin using a pressurized die.* Electronic Letters, *18*, 713–715 (1982).

P. Chossat, G. Iooss, *The Couette-Taylor problem.* Springer-Verlag (Applied Mathematical Sciences, Vol. 102), 1994.

K. A. Cliffe, J.J. Kobine, T. Mullin, *The role of anomalous modes in Taylor-Couette flow.* Proc. R. Soc. London **439** (1992).

M. M. Couette. *Sour un nouvel apareil pour l'étude du frotement des fluids.* Comptes Rendus **107**, 388-90 (1888).

P. Coullet, E. A. Spiegel *Amplitude equations for systems with competing instabilities.* SIAM J. Appl. Math. **43**: 776-821 (1983).

M. C. Cross, P. C. Hohenberg,. *Pattern formation outside of equilibrium.* Rev. Mod. Phy. Vol. 65, N. 3, Part II (1993). J. T. Stuart. *On the nonlinear mechanics of wave disturbances in stable and unstable parallel flows. Part 1. The basic behaviour in plane Poiseuille flow.* Journal of Fluid Mechanics. **9**, 353-70 (1960).

Y. Demay, G. Iooss. *Calcul des solutions bifurquées pour le problème de Couette-Taylor avec les deux cylindres en rotation.* Journal de Mècanique théorique et apliquée (n.e.) 193-216 (1984).

P. G. Drazin, W. Reid *Hydrodynamic Stability.* Cambridge University Press (1981).

W. Eckhaus *The Ginzburg-Landau Manifold is an Attractor.* Journal of Nonlinear Science Vol. 3 pp. 329-348 (1993).

W.S. Edwards, R.P. Tagg, B.C. Dornblaser, H.L. Swinney. *Periodic traveling waves with nonperiodic pressure.* Eur. J. Mech. B Fluids, **10**, 205–210 (1991).

D. Farmer, J.P. Crutchfield, H. Froehling, N.H. Packard, R. Shaw. Ann. N.Y. Acad. Sci. **357** (1980), 453. Part I (1981).

P. Grassberger, I. Procaccia. *Characterization of Strange Attractors.* Phys. Rev. Lett. 50,346 (1983).

J. Guckenheimer, P. Holmes, *Nonlinear Oscillations, Dynamical Systems, and Bifurcations of Vector Fields.* Springer-Verlag (Applied Mathematical Sciences, vol.42), (1986).

M. M. Gupta, R. P. Manohar. J. Comput. Phys. **31**, 265-288 (1979).

H.C. Hu, R.E. Kelly. Effect of a time-periodic axial shear flow upon the onset of Taylor vortices. Physical Review E, **51**, 3242–3251 (1995)

W.L. Hung, D.D. Joseph, B.R. Munson. *Global stability of spiral flow. Part 2.* Journal of Fluid Mechanics, **51**, 593–612 (1972)

G. Iooss, M. Adelmeyer, *Topics in Bifurcation theory and applications.* Advanced series in Nonlinear dynamics, Vol. 3. World Scientific (1992).

E. Isaacson and H.B. Keller. *Analysis of Numerical Methods.* John Wiley & Sons, (1966).

D. D. Joseph. *Stability of Fluid Motions* vol. I and II. Springer Tracts in Natural Philosophy, 27-28. Springer-Verlag, Berlin (1976)

H.B.Keller. *Numerical Solution of bifurcation and nonlinear eigenvalue problems* in Applications of Bifurcation Theory, edited by P.H. Rabinowitz. Academic, New York, (1977).

I. Kiessling. *Uber das Taylorsche Stabilitatsproblem bei zusatzlicher axialer Durchstromung der Zylinder.* Duetsche Versuchsanstalt fur Luft-Unraumfahrt—Bericht 290 (1963).

K. Z. Korczak, A. T. Patera. *Isoparametric spectral element method for solution of the Navier-Stokes equations in complex geometry.* J. Comput. Phys. **62**, 361-382 (1986).

M. Kubicek, M. Marek. *Computational Methods in Bifurcation 3Theory and Dissipative Structures.* Springer-Verlag (Springer Series in Computational Physics) (1983).

L. D. Landau. C.R. Acad. Sci. U.R.S.S.M. **44**, 311.

L. D. Landau, E. M. Lifshitz, *Fluid Mechanics (2nd ed.).* Pergamon Press, Oxford (1987).

W. F. Langford *The Taylor-Couette System* in *Singularities and Groups in Bifurcation Theory.* M. Golubitsky, I. Stewart, D. G. Schaeffer. Springer-Verlag (Applied Mathematical Sciences, Vol. 69) (1988).

C. C. Lin, *The theory of hydrodynamic stability.* Cambridge Univ. Press (1955).

E.N. Lorenz. *Deterministic Non-Periodic Flow*, J. Atm. Sci. **20** (1963), 130-141.

H. Ludwieg. *Experimentelle Nachprufung des stabilitatstheorien fur reibungsfreie Stromungen mit schraubenlinienformigen stromlinien.* Z. Flugwiss, 12, 304–309 (1964)

P.A. Mackrodt. *Stability of Hagen-Poiseuille flow with superimposed rigid rotation.* Journal of Fluid Mechanics, **73**, 153-164 (1976)

A. Mallock. *Determination of the viscosity of water.*, Proc. R. Soc. London, Ser. A **45**, 126-32 (1888).

F. Marqués, Phys. Fluids A 2 (5) (1990), 729–737.

F. Marques and J.M. Lopez. *Taylor–Couette flow with axial oscillations of the inner cylinder: Floquet analysis of the basic flow* Journal of Fluid Mechanics, to appear in September (1997)

I. Mercader, M. Net, A. Falqués, *Spectral Methods for high order equations.* Computer Methods in Applied Mechanics 91 (1991).

A. Meseguer, F. Marqués, *Centrifugal versus Shear Instability in the Spiral Couette Flow.* (under revision in Journal of Fluid Mechanics).

A. Meseguer, F. Marques, J. Sanchez. *Feigenbaum's Universality in a Four-Dimensional Fluid Model.* Int. J. of Bifurcation and Chaos, **6**, 1587-1594 (1996)

R.D. Moser, P. Moin, A. Leonard. *A spectral numerical method for the Navier-Stokes equations with applications to Taylor-Couette Flow.* J. Comput. Phys. **52**, 524-544 (1983).

J.E. Mott, D.D. Joseph. *Stability of Parallel Flow between Concentric Cylinders.* Phys. Fluids **11**, 2065-2073 (1968).

A.C. Newell, J. A. Whitehead. *Finite Amplitude, Finite Bandwidth Convection.* Journal of Fluid Mechanics **38** pp. 279-303 (1969)

D.F. Ollis, E. Pelizzetti, N. Serpone. *Photocatalyzed destruction of water contaminants.* Environ.

Sci. Technol., **25**, 1523–1529 (1991)

R. Peyret, T.D. Taylor. *Computational Methods for Fluid Flow.* Springer-Verlag. (Springer Series in Computational Physics) (1983).

W. H. Press, B. P. Flannery, S. A. Teukolsky, W. T. Vetterling. *Numerical Recipes (the art of scientific computing).* Cambridge Univ. Press, (1986)

R. H. Rand, D. Armbruster. *Perturbation Methods, Bifurcation Theory and Computer Algebra.* Springer-Verlag (Applied Mathematical Sciences, Vol. 65), (1987).

D. Ruelle. *Chaotic Evolution and Strange Attractors.* Cambridge Univ. Press. (1989).

V.M. Sadeghi, B.G. Higgins. *Stability of sliding Couette-Poiseuille flow in an annulus subject to axisymmetric and asymmetric disturbances.* Phys. Fluids A **3**(9) (1991).

J. Sanchez, D. Crespo, F. Marques. *Spiral Vortices Between Concentric Cylinders.* Applied Scientif Research, **51**, 55–59 (1993).

L. F. Shampine, M. K. Gordon. *Computer Solution of Ordinary Differential Equations. The initial value problem.* W. H. Freeman and Company, San Francisco, (1975).

J. Shen. *Hopf Bifurcation of the Unsteady Regularized Driven Cavity Flow.* J. Comput. Phys. **95**, 228-245 (1991).

J. Shen. Comput. Methods Appl. Mech. Eng. **80**, 273 (1990).

I. Shimada, T. Nagashima. Prog. Theor. Phys. **61** (1979), 1605-1615.

J. T. Stuart. *On the nonlinear mechanics of wave disturbances in stable and unstable parallel flows. Part 1. The basic behaviour in plane Poiseuille flow.* Journal of Fluid Mechanics. **9**, 353-70 (1960).

G. I. Taylor. *Stability of a viscous liquid contained between two rotating cylinders.* Phil. Trans. Roy. Soc. London, Ser. A**223**, 289-343 (1923).

Z. Tadmor, R.B. Bird. *Rheological Analysis of stabilizing forces in wire-coating dies.* Polymer Engineering and Science, **14**, 124–136 (1974)

J. Phys. Soc. Japan **46**, 1935.

R. Temam. *Infinite Dimensional Dynamical Systems in Mechanics and Physics.* Springer-Verlag. New York (1988).

J. Watson. *On the nonlinear mechanics of wave disturbances in stable and unstable parallel flows. Part 2. The development of a solution for plane Poiseuille flow and for plane Couette flow.* Journal of Fluid Mechanics. **9**, 371-89 (1960).

E. Wedemeyer. *Einfluss der Zahigkeit auf die Stabilitat der Stromung in einem schmalen Ringraum* *mit zusatzlichem, axialem Durchfluss.* AVA–Bericht 67, A34 (1967).

A.Y. Weisberg. *Control of transition in Taylor-Couette flow with axial motion of the inner cylinder.* Ph.D. thesis, Princeton, Dep. of Mechanical and aerospace engineering. (1996)

R. F. Wittenberg, P. Holmes. *The limited efectiveness of normal forms: a critical review and extension of local bifurcation studies of the Brusselator PDE.* Physica D **100** 1-40.